Drops on hydrophobic surfaces & vibrated fluid surfaces

Wind-Willassen, Øistein

Publication date:
2014

Document Version
Publisher's PDF, also known as Version of record

Drops on hydrophobic surfaces & vibrated fluid surfaces

Øistein Wind-Willassen

Kongens Lyngby 2014
PhD-2014-323

Technical University of Denmark
Department of Applied Mathematics and Computer Science
Matematiktorvet, building 303B,
2800 Kongens Lyngby, Denmark
Phone +45 4525 3351
compute@compute.dtu.dk
www.compute.dtu.dk ISSN: 0909-3192

Summary (English)

The first part of this thesis deals with a droplet on a hydrophobic surface. We first present a basic introduction to fluid dynamics, including a description of relevant dimensionless numbers and a derivation of the Young-Laplace equation. An analytic approach to describing the oscillations of a droplet is then given, after which we set up a 2D computational Finite-Element Method (FEM) model for a neutrally buoyant drop immersed in another liquid. The model is validated by considering the volume loss over time.

Subsequent to an introduction to the physics of wetting, the developed FEM model is then extended to include drop-surface interactions, and we describe a) the initial descent of a droplet down an inclined hydrophobic substrate, and b) the motion of the droplet in a potential well created through spatial contact angle variations. We solve the full Navier-Stokes equations inside the drop domain, and use the Arbitrary Lagrangian-Eulerian method to keep track of the droplet surface; the contact angle is included by using the Frennet-Serret equations.

In situation a), we investigate the behavior of the drop velocity as a function of the slip length and compare with experimental results found in the literature. Furthermore, we quantify the energy associated with center of mass translation and internal fluid motion. The model predicts trajectories for tracer particles deposited inside the drop, and satisfactorily describes the sliding motion of steadily accelerating droplets. The model can be used for determining a characteristic slip parameter, associated with slip lengths and drag reduction for hydrophobic surfaces.

In situation b), we observe that the droplet oscillations (frequency, amplitude and decay time) in the potential is not linear with respect to the forcing, i.e. the strength of the potential, and contribute this to preferred eigenmodes of the droplet oscillation.

The second part of this thesis deals with a droplet bouncing on a vertically vibrated fluid bath of the same liquid, a system which is the first known macroscopic example of pilot-wave dynamics. An introduction to the experimental set-up is given, followed by a description of the mathematical models governing the vertical and horizontal motion of the drop. Two in-depth studies are then presented.

In the first, the results of a comprehensive series of experiments are presented. The most detailed characterisation to date of the system's dependence on fluid properties, droplet size, and vibrational forcing is provided. A number of new bouncing and walking states are reported, including complex periodic and aperiodic motions. Specific attention is given to the first characterisation of the different gaits arising within the walking regime. In addition to complex periodic walkers and limping droplets, we highlight a previously unreported mixed state, in which the droplet switches periodically between two distinct walking modes. The experimental results are compared to previously developed theoretical predictions.

In the second study, wo consider the case where the fluid bath is also rotated around its center-line. The drop then experiences an effective Coriolis force, and previous studies have made a comparison between emerging unstable radii in this system and Landau levels for a charged particle in a magnetic field. The system is treated numerically, and the results are compared to experiments. We provide, again, the most detailed regime diagram of the possible orbits depending on the forcing and the rotation rate of the fluid bath. We highlight each class of orbit, and analyze in depth the wobbling state, precessing orbits, wobble-leap dynamics, exotic trajectories and the emergence of statistical behavior when the forcing is near the Faraday threshold.

Summary (Danish)

Den første del af denne afhandling beskæftiger sig med en dråbes interaktion med en hydropfob overflade. Vi præsentererd først en introduktion til fluiddynamik, indeholdende en beskrivelse af relevante dimensionsløse størrelser samt en udledning af Young-Laplace ligningen. Derefter gives en analytisk tilgang til beskrivelsen af en dråbes oscillationer, efterfulgt af udviklingen af en to-dimensionel numerisk Finite-Element Metode (FEM) model for en frit svævende dråbe omgivet af en anden fluid. Modellen valideres ved at betragte volumentabet over tid. Efter en introduktion til fysikken for overfladers fugtningsegenskaber udvider vi modellen til at inkludere interaktioner mellem dråbe og overflade. Vi beskriver a) dråbens begyndende bevægelse på en skrå hydrofob overflade, samt b) dråbens bevægelse i en potential-brønd, hvor brønden er skabt ud fra rumlige gradienter i kontaktvinklen.

Vi løser den fulde Navier-Stokes ligning i dråbens domæne, og benytter metoden Arbitrary Lagrangian-Eulerian til at følge dråbens overflade. Kontaktvinklen er inkluderet ved at anvende Frennet-Serret ligningerne.

I situation a) undersøger vi dråbens hastighed som funktion af sliplængden på randen og sammenligner med eksperimentelle resultater. Desuden giver vi et bud på energien, der er associeret med den translatoriske bevægelse af dråbens massemidtpunkt samt med den interne fluids bevægelse. Modellen giver et bud på bevægelsen af enkelte partikler placeret i dråben og giver et tilfredsstillende bud på konstant accelererende dråbers bevægelse. En anvendelse af modellen er at finde en karakteristisk slipparameter, der er associeret med slip længden og reduktion i drag for en given hydrofob overflader.

I situation b) observerer vi en ikke-lineær sammenhæng mellem dråbens oscillation (frekvens, amplitude og henfaldstid) og styrken af potentialet, og vi tilskriver dette foretrukne egentilstande i dråbens interne oscillation.

Den anden del af afhandlingen handler om en dråbe, der hopper på en vertikalt vibrerende overflade af samme væske. Dette system er det første kendte eksempel på et system med makroskopisk pilot-bølge dynamik. Vi giver en introduktion til den eksperimentelle opstilling, og derefter beskriver vi den matematiske model der anvendes til at beregne dråbens vertikale og horisontale bevægelse.

Vi præsenterer resultatet af en omfattende række af eksperimenter der giver den til dato mest fuldstændige karakterisering af systemets opførsel som funktion af fluidens egenskabder, dråbens størrelse og den vibrationelle kraft. Et antal nye vertikale hoppe tilstande samt horisontale bevægelser dokumenteres, inklusiv komplekse periodiske og aperiodiske bevægelser. Speciel opmærksomhed gives til de vertikale hoppetilstande i regionen, hvori dråberne bevæger sig horisontalt over overfladen. I tillæg til de komplekse periodiske walkere og haltende dråber, fremhæver vi en hidtil urapporteret "mixed"tilstand, hvori dråben skifter periodisk mellem to specifikke tilstande. De eksperimentelle resultater sammenlignes med tidligere udviklede teoretiske forudsigelser.

Når det vibrerede væskebad udsættes for en rotation omkring den vertikale centerlinje, oplever dråben en effektic corioliskraft. Tidligere studier har sammenlignet de ustabile radier, der opstår i det fluiddynamiske system med Landau niveauerne for en ladet partikel i et magnetfelt. Vi betragter systemet numerisk og sammenligner enkelte resultater med eksperimentelle observationer. Igen præsenteres det til dato mest komplette regime diagram for de fundne tilstande som funktion af den vibrationelle kraft og rotationsraten af badet. Vi fremhæver hver enkelt klasse af de observerede tilstande og analyserer dem i dybden. Det drejer sig om oscillerende tilstande, baner der precesserer, tilstande der oscillerer og derefter springer til et nyt punkt i rummet, eksotiske baner, samt opståelsen af statistisk opførsel når den vibrationelle kraftpåvirkning er tæt på Faraday grænsen.

Preface

This thesis is based on the scientific studies performed in the period from January 2011 to January 2014. It has been prepared at the Technical University of Denmark - Institute for Mathematics (which is now the Department of Applied Mathematics and Computer Science) in partial fulfillment of the requirements for acquiring the PhD degree. The project, funded by the Nanoplast project and DTU, has mainly been supervised by Professor Mads Peter Sørensen (DTU Compute) and co-supervised by Rafael Jozef Taboryski and Alicia Charlotte Johansson (both DTU Nanotech).

The thesis is divided into two parts, covering the major areas of study I have been involved in. The first part deals with droplets on hydrophobic surfaces, specifically the influence of hydrophobicity on the fluid flow inside a droplet as it moves across the surface. The second part is concerned with a system where a drop bounces on a vertically vibrated fluid bath, which gives rise to interesting dynamical phenomena. The unifying theme is droplets at the millimeter scale, but since the two topics represent disconnected studies, the overlap is small. It is my hope, however, that some sections from Part 1 will be useful to the reader in Part 2.

The work presented herein has been, and will be, communicated in the following journal articles:

- Øistein Wind-Willassen, Jan Molacek, Daniel M. Harris and John W. M. Bush., Exotic states of bouncing and walking droplets, *Physics of Fluids* **25** 082002 (2013). Included in Appendix A.1.
- Øistein Wind-Willassen and Mads Peter Sørensen, A Finite-Element Method

Model for Droplets on Hydrophobic Surfaces, under consideration for publication in *European Journal of Physics E* (2013). Included in Appendix A.2.

- Anand U. Oza, Øistein Wind-Willassen, Daniel M. Harris, Rodolfo R. Rosales and John W. M. Bush, Exotic trajectories in the rotating frame, under preparation (2013).

Additionally, the following article was published during my period at DTU:

- Williams, N., Wind-Willassen, Ø., Program, REU, Olufsen, M., Mehlsen, J., Ottesen, J., Patient Specific Modeling of Head-Up Tilt, in press *Mathematical Medicine and Biology*, 2013.

I have given the following presentations:

- Modelling sessile droplets on structured surfaces, oral presentation at *DANSIS research seminar*, May 2012.
- Modelling sessile droplets on structured surfaces with spatially varying contact angle, oral presentation at *American Physical Society 65th annual Divison of Fluid Dynamics meeting*, November 20 2012.
- Bouncing drops on a vibrating fluid bath, oral presentation at *DCAMM Symposium*, March 13, 2013.
- Bouncing droplets on a vibrating fluid bath, oral presentation at *DTU Mathematical Colloquium*, May 8, 2013
- Droplets on hydrophobic surfaces: two approaches, poster presented at *Fluid-DTU summerschool: Complex motion in fluids*, August 2011.
- Modelling sessile droplets on structured surfaces with spatially varying contact angle, poster presented at *European Post Graduate Fluid Dynamics Conference*, July 10-12 2012.

I spent six months with Professor John Bush's group at Massachusetts Institute of Technology from September 2012 to March 2013. This stay has been very rewarding, both on the academic and personal level, and I would like to thank John for his kind hospitality, his high spirit, and for being a great motivator. Also, many thanks to Anand, Dan, and Jan for the collaborations, and for taking their time to discuss, explain and socialize during, and also after, my stay at MIT.

Also, a lot of thanks to my girlfriend Lea, family, friends, and colleagues at DTU. I give special thanks to Michael and Lars for helping out in the last stage of the writing process.

I am grateful to my supervisor Mads Peter Sørensen. You have allowed me to pursue the ideas and scientific areas I found interesting, even though they did not necessarily coincide with the project we started with. Your door has always been open, and I would like to thank you for an always encouraging perspective on things.

Lyngby, 06-January-2014

Øistein Wind-Willassen

Contents

List of symbols

Notation in general	
Variable	Definition
ρ	fluid density
$\mathbf{u}$	velocity field
$\mathbf{S}$	stress tensor
$\mathbf{f}$	external forces
η	dynamic viscosity
ν	kinematic viscosity
$\sigma = \sigma_{LG}$	surface tension (liquid-gas interfacial tension)
a, R_0, $D/2$	drop radius
$l_c = \sqrt{\frac{\sigma}{g\delta\rho}}$	capillary length
$Re = \frac{UL}{\nu}$	Reynolds number
$Bo = \frac{g\delta\rho L^2}{\sigma}$	Bond number
$Ca = \frac{\eta U}{\sigma}$	capillary number
$We = \frac{\rho U^2 L}{\sigma}$	Weber number
$Oh = \frac{\eta}{\sqrt{\rho\sigma L}}$	Ohnesorge number
$Fr = \frac{U^2}{gL}$	Froude number

Specific notation in Part I	
Variable	Definition
L, U	characteristic length and velocity
ψ	velocity potential
σ_{LS}, σ_{LG}, σ_{SG}	liquid-solid, liquid-gas, solid-gas interfacial tensions
β	slip length
Ψ	velocity potential
θ, θ_A, θ_R	contact angle, receding (R) and advancing (A)
θ_e	Youngs contact angle
$\Delta\theta = \theta_A - \theta_R$	contact angle hysteresis
$S = \sigma_{SG} - (\sigma_{SL} - \sigma_{LG})$	spreading parameter
r	surface roughness
f_1, f_2	fractional surface areas
α_R	roll-off angle
R_1, R_2	principal radiis of curvature
$\mathbf{n}$, $\mathbf{t}$, $\mathbf{e}$	normal vector, tangent vector, vector along gravity
κ	mean interface curvature
$\nabla_s = \nabla - \mathbf{n}\frac{\partial}{\partial n}$	surface gradient operator
Ω, Γ	computational domain and boundaries

Specific notation in Part II	
Variable	Definition
$f = \frac{\omega}{2\pi}$	vertical oscillation frequency of bath
$\gamma = A\omega^2$	forcing acceleration
$\Gamma = \gamma/g$	dimensionless forcing
$g^*(t)$	gravitational acceleration in bath frame of reference
k_F, λ_F	Faraday wave number and wavelength
γ_B, γ_w, γ_F	bouncing, walking, and Faraday threshold
$\Omega = 2\pi f\sqrt{\frac{r_0^3\rho}{\sigma}}$	vibration number
R_0	drop radius
T_d	viscous decay time of surface waves
$T_F = 2/f$	Faraday period
$M_e(\gamma) = \frac{T_d}{T_F(1-\gamma/\gamma_F)}$	memory parameter
c_1, c_2, c_3	coefficients in the model for the vertical dynamics
z	drop center of mass position
$F_N(t) = m\ddot{z} + mg^*(t)$	normal component of reaction force
$h_n(\mathbf{x}, t)$	surface wave created from single drop impact
$h(\mathbf{x}, t)$	total fluid surface height
μ_{eff}	phenomenological (effective) viscosity
D	drag coefficient
$(m, n)^i$	vertical drop bouncing mode
Ω_R	vertical rotation rate of fluid bath
$\kappa = \frac{m}{DT_F M_e}$	nondimensional mass
$\beta = \frac{Fk_F T_F M_e^2}{D}$	nondimensional wave force coefficient
r_0	orbital radius
ω	orbital frequency
$\overline{r}(t)$	instantaneous orbital radius
(x_c, y_c)	coordinates of orbital center

Part I

Droplets on structured surfaces

Chapter 1

Fluid dynamics fundamentals

The goal of the following part is two-fold. First, an introduction to the physics of fluids is given, consisting of the governing equations for the fluid and its interface along with relevant characteristic dimensionless numbers. Second, a numerical method is developed. This method serves as a basis for the treatment of drops residing on a hydrophobic surface, the topic of chapter 5.

After the fluid dynamical introduction, which is based on standard textbooks on the subject [1, 2, 3], special analytic and numerical attention is thus given to the case where a liquid droplet is suspended in another fluid of lighter density. A reason for the somewhat detailed exploration of an oscillating drop is found in Part II, where a drop bouncing on a vibrated liquid surface is considered. Here, the internal drop frequencies are of importance to the observed behavior, and an understanding of this phenomenon is necessary.

1.1 Fluid properties

A fluid consists of a number of molecules interacting through Newton's laws, giving rise to the physical properties of the fluid. When describing the fluid

it is useful to consider the continuum hypothesis in which the fluid is thought of as perfectly continuous in structure. Properties of the fluid is taken per volume, e.g. mass density, momentum density, force density etc. The usual goal in fluid dynamics is to obtain the velocity field as a function of position and time, $\mathbf{u}(\mathbf{x}, t)$, which is described by a set of nonlinear partial differential equations, and they originate from Newton's second law of motion. A fluid deforms continuously when stresses are applied, and it can be a gas as well as a liquid, plasma or plastic solid.

Assuming that the fluid is incompressible, i.e. the density is assumed constant, we obtain

$$\rho\left(\frac{\partial \mathbf{u}}{\partial t} + \mathbf{u}\cdot\nabla\mathbf{u}\right) = \nabla\cdot\mathbf{S} + \mathbf{f}, \tag{1.1}$$

$$\nabla\cdot\mathbf{u} = 0. \tag{1.2}$$

Here Eq. (1.1) are the Navier-Stokes equations and Eq. (1.2) is the incompressibility condition. The mass density is ρ, p is the pressure, $\mathbf{S}$ is the stress tensor, and $\mathbf{f}$ is some body force acting on the fluid, e.g. gravitational forces, electrical forces etc. The stress tensor is a function of the velocity $\mathbf{u} = \mathbf{u}(\mathbf{x}, t)$ and the pressure. For a Newtonian fluid (where the viscous shear stress inside the liquid is proportional to the local strain rate),

$$S(\mathbf{u}, p)_{i,j} = 2\eta D(\mathbf{u})_{i,j} - p\delta_{i,j}, \qquad i, j = 1, 2, 3,$$

where

$$D(\mathbf{u})_{i,j} = \frac{1}{2}\left(\frac{\partial u_i}{\partial x_j} + \frac{\partial u_j}{\partial x_i}\right), \qquad i, j = 1, 2, 3.$$

Here $\eta = \rho\nu$ is the dynamic viscosity (ν is the kinematic viscosity), Together with suitable boundary conditions, these equations describe the state of an incompressible fluid in terms of the velocity $\mathbf{u}$ and pressure p. Several techniques exists for solving the equations analytically, but they all rely of some form of simplifying assumptions. In Chapter 2, the viscosity is neglected, and the velocity is assumed to be the gradient of some scalar field, $\mathbf{u} = \nabla\psi$. These assumptions result in what is called a potential flow. One can also look for steady state solutions, i.e. when $\partial_t\mathbf{u} = 0$, or consider pressure driven flows where the entire left hand side of Eq. (1.1) has been neglected.

In numerical implementations of Eqs. (1.1)-(1.2), a nondimensionalized version is typically used to avoid issues where quantities are of significantly different orders of magnitude. We make a change in coordinates,

$$\mathbf{x} = \hat{\mathbf{x}}L, \quad \mathbf{u} = \hat{\mathbf{u}}U, \quad p = \frac{\eta U}{L}\hat{p}, \quad t = \hat{t}\frac{L}{U}, \tag{1.3}$$

where L and U is a characteristic length and velocity, respectively. The nondimensionalized equations are

$$\partial_{\hat{t}}\hat{\mathbf{u}} + \left(\hat{\mathbf{u}} \cdot \hat{\nabla}\right)\hat{\mathbf{u}} = \hat{\nabla} \cdot \hat{\mathbf{S}} + \frac{L}{U^2}\mathbf{f}, \tag{1.4}$$

$$\hat{\nabla} \cdot \hat{\mathbf{u}} = 0. \tag{1.5}$$

Here, quantities with hats denote a dimensionless quantity. If gravity is the only external body force on the fluid, $\mathbf{f} = g\mathbf{e}$, where $\mathbf{e}$ is the normal vector in the direction of gravitation, and g is the gravitational constant. Then the last term can be written $\mathbf{e}/Fr$, where $Fr = U^2/(gL)$ is the Froude number.

The Navier-Stokes equation governs the bulk of the fluid, but the interface shape between two fluids is a function of the pressure difference and the surface tension.

1.2 Interfaces between liquids

Surface tension, σ, is important for many everyday phenomena, e.g. the size of raindrops and the attraction of cheerios in your morning cereal. To understand its origin, assume that a liquid has an interface with another fluid, and consider two situations at the molecular level as depicted in Figure 1.1. Every molecule in the liquid experiences a cohesive force from the surrounding molecules. In panel (a), the molecule in the bulk has a bond with all neighbors while, in panel (b), the molecule at the interface experiences a bond with fever molecules in the liquid. This results in an energetically unfavorable state for molecules at the interface. A given amount of liquid will organize into the state with the lowest energy cost or minimal surface area per volume, and for small amounts of liquid this is a sphere. Surface tension is measured as $\frac{\text{Energy}}{\text{Area}}$ or $\frac{\text{Force}}{\text{Length}}$, and has as a unit $\frac{\text{N}}{\text{m}}$. For water at 25° C, $\sigma \approx 70$ mN/m, and at 100° C, $\sigma \approx 60$ mN/m.

The surface tension at the interface between two immiscible (non mixing) liquids and the pressure difference across the same interface is connected through the geometry of the interface. Consider the situation in Figure 1.2, where two liquids with pressures p_1 and p_2, respectively, are separated by an interface with given surface tension σ.

There is a small surface element, $df = ds_1 ds_2$, which has, at the point P, principal radii of curvature R_1 and R_2 and normal vector $\boldsymbol{n}$. We can at each point of the entire displaced surface draw the normal to the surface. The length of the normal lying between the original surface and the displaced, is denoted by $\delta\xi$.

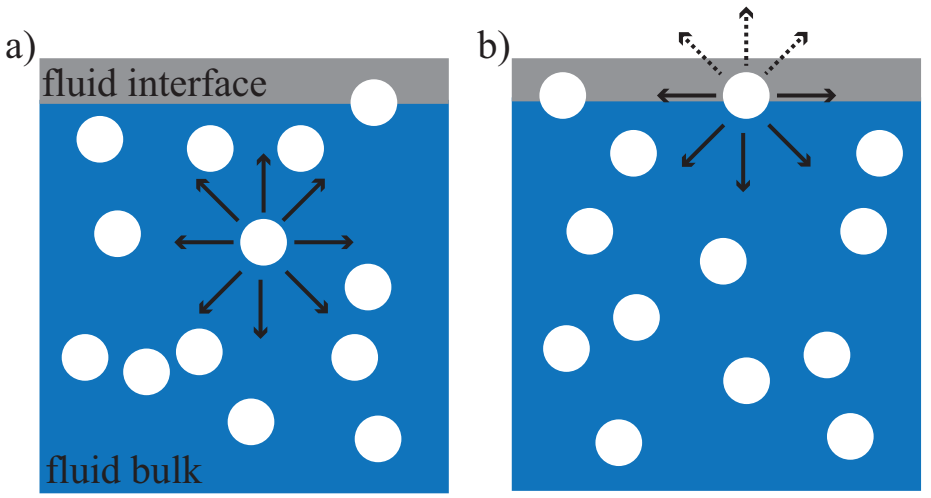

Figure 1.1: Sketch of the molecular level of a liquid. (a) A molecule in the fluid bulk has bonds with all neighboors. (b) A molecule at the interface of liquid has fewer connections, resulting in a higher energy configuration.

The displaced volume of this small surface element is

$$dV = df\delta\xi,$$

and the work needed to obtain the displacement for the entire surface is

$$\delta W_{displacement} = \int (-p_1 + p_2)\delta\xi df.$$

The work associated with changing the entire surface area with the amount δf is

$$\delta W_{surface} = \sigma\delta f,$$

Thus, the total work required for the displacement of the entire surface is

$$\delta W = \delta W_{surface} + \delta W_{displacement} = \sigma\delta f - \int (p_1 - p_2)\delta\xi df. \qquad (1.6)$$

In Figure 1.2, the lengths ds_1 and ds_2 are drawn on the surface in its principal curvature sections. Since we are considering infinitesimal displacements, we assume that these arcs are straight lines. The triangles between R_1, ds_1 and $\boldsymbol{n}$, and also R_2, ds_2 and $\boldsymbol{n}$, gives us the lengths of the displaced ds_1 and ds_2:

$$ds_1^{'} = \frac{ds_1}{R_1}(R_1 + \delta\xi),$$

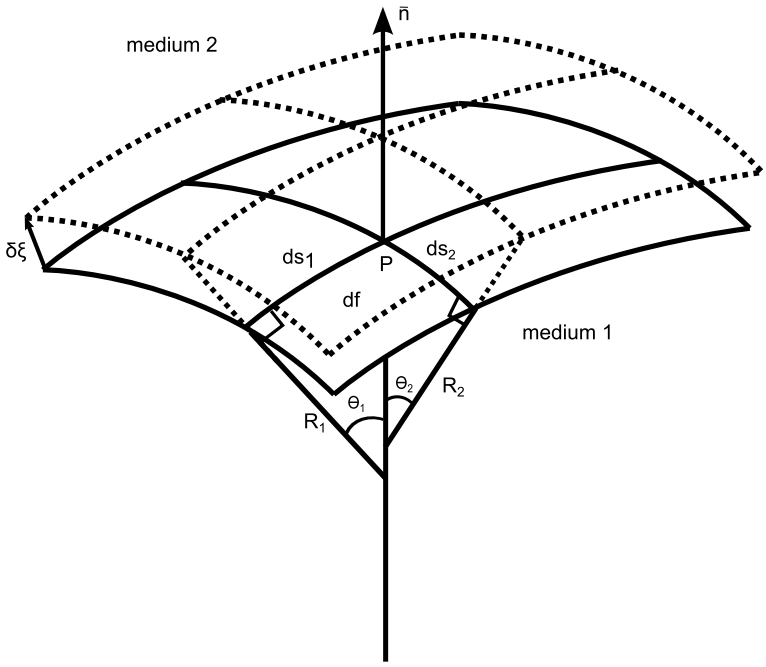

Figure 1.2: The displacement of a surface df by the normal vector $d\xi$.

and

$$ds_2^{'} = \frac{ds_2}{R_2}(R_2 + \delta\xi).$$

The displaced surface element $df^{'}$ is then

$$df^{'} = ds_1^{'} ds_2^{'} = ds_1 \frac{R_1 + \delta\xi}{R_1} ds_2 \frac{R_2 + \delta\xi}{R_2} = df\left[1 + \frac{\delta\xi}{R_1} + \frac{\delta\xi}{R_2}\right],$$

where we have assumed that $\delta\xi^2 = 0$. The small surface element df changes by $\delta\xi(\frac{1}{R_1} + \frac{1}{R_2})df$, and to obtain an expression for the entire surface, we integrate with respect to df,

$$\delta f = \int \delta\xi \left(\frac{1}{R_1} + \frac{1}{R_2}\right) df. \tag{1.7}$$

When this is inserted in Equation (1.6), and the thermodynamic equilibrium condition

$$\delta W = 0,$$

is employed, we get that

$$\int \delta\xi \left[\sigma\left(\frac{1}{R_1} + \frac{1}{R_2}\right) - (p_1 - p_2)\right] df = 0. \tag{1.8}$$

Since this has to hold for all small displacements, i.e. for all values of $\delta\xi$, we get the Young-Laplace equation

$$(p_1 - p_2) = \sigma\left(\frac{1}{R_1} + \frac{1}{R_2}\right). \tag{1.9}$$

The term $\kappa = (1/R_1 + 1/R_2)$ is recognized as the mean curvature of the surface which can be computed for general surfaces. Suppose the interface can be covered by a patch $\boldsymbol{s}\,(u, v)$ with first and second fundamental forms

$$\mathrm{I} = Edu^2 + 2Fdudv + Gdv^2$$

$$\mathrm{II} = Ldu^2 + 2Mdudv + Ndv^2,$$

where

$$E = \left|\left|\frac{\partial \boldsymbol{s}}{\partial u}\right|\right|^2,\ F = \frac{\partial \boldsymbol{s}}{\partial u} \cdot \frac{\partial \boldsymbol{s}}{\partial v},\ G = \left|\left|\frac{\partial \boldsymbol{s}}{\partial v}\right|\right|^2,$$

and

$$L = \frac{\partial^2 \boldsymbol{s}}{\partial u^2} \cdot \boldsymbol{N},\ M = \frac{\partial^2 \boldsymbol{s}}{\partial u \partial v},\ N = \frac{\partial^2 \boldsymbol{s}}{\partial v^2} \cdot \boldsymbol{N}.$$

where $\boldsymbol{N}$ is the unit normal to the surface [4]. The mean curvature, κ, is then given as

$$\kappa = \frac{LG - 2MF + NE}{2\,(EG - F^2)},$$

and the Young-Laplace equation becomes a partial differential equation (in the following, $\partial_u s = \partial s/\partial u$)

$$(p_1 - p_2) = \sigma \frac{\left(1 + (\partial_v s)^2\right) \partial_u^2 s - 2\partial_u s \partial_v s \partial_{uv} s + \left(1 + (\partial_u s)^2\right) \partial_v^2 s}{\left(1 + (\partial_u s)^2 + (\partial_v s)^2\right)^{3/2}}. \tag{1.10}$$

This equation determines the shape of the interface between fluids. Notice that, for a given pressure difference ΔP, the centre of curvature lies in the phase with the higher pressure. Also, if the pressure difference is constant, an increase in surface tension results in a decrease in curvature, i.e. a more flat interface. The pressure inside a small bubble is also higher than inside a bubble of larger radius (with same surface tension), which makes it louder when bursting.

The Young-Laplace equation can be stated in a slightly more general way when spatial gradients in σ are included,

$$\mathbf{n} \cdot \mathbf{S}^2 - \mathbf{n} \cdot \mathbf{S}^1 = \kappa\sigma\mathbf{n} - \nabla_s \sigma, \tag{1.11}$$

where $\mathbf{S}^i$ is the stress tensor in liquid 1 and 2, $\mathbf{n}$ is the outward unit normal to the interface, and ∇_s is the surface gradient operator, which is the gradient operator restricted to the surface. This operator is written as [5]

$$\nabla_s = (\mathbf{I} - \mathbf{nn})\nabla = \nabla - \mathbf{n}\partial_n. \tag{1.12}$$

Intuitively this means that ∇_s has no component in the normal direction. Flows induced by spatial variations in the surface tension are called Marangoni flows. These gradients arise for different reasons, but some of the main sources are temperature variations, uneven positioning of detergents residing on the surface (soap), or a changing concentration of some chemical in the fluid.

We know from everyday experience that larger puddles of water does not appear spherical everywhere, so when does gravity begin to impact the geometry and behavior of liquids? In the next section, relevant dimensionless numbers are introduced.

1.3 Dimensionless numbers and scaling

Several forces act on a liquid, but depending on the characteristic length scale and other physical properties of the system, they might not all be equally important. An attempt to asses the relative importance of forces and timescales is done by considering a number of dimensionless quantities. The probably most

well-known quantity is Reynolds number, the ratio of inertial forces to viscous forces,

$$Re = \frac{UL}{\nu}, \tag{1.13}$$

where U and L are the characteristic velocity and length of the system, respectively. High Reynolds numbers are characteristic of inertial flows, with possible turbulence, and low Reynolds numbers usually indicate a laminar flow. This dimensionless number naturally arises when re-scaling Navier-Stokes' equations (Eq. (1.1)) using a characteristic length, velocity, time and pressure.

For liquid drops with characteristic length L (typically the radius of the drop), there is a natural limit for when gravity forces surpasses those of the surface tension. The Bond number is the ratio of gravitational effects to surface tension effects,

$$Bo = \frac{g\Delta\rho L^2}{\sigma}, \tag{1.14}$$

where g is the gravitational acceleration, and $\Delta\rho = \rho_2 - \rho_1$ is the density difference between the two fluids. Small values (< 1) of Bo indicate the dominance of surface tension, resulting in spherical shapes of interfaces. This can be achieved through large values of σ, or by reducing the characteristic length of the system. If we assume $Bo = 1$, and solve for the associated length scale, l_c, we obtain the capillary length,

$$l_c = \sqrt{\frac{\sigma}{g\Delta\rho}}. \tag{1.15}$$

This quantity essentially describes the size below which things are dominated by surface tension. For water surrounded by air at room temperature and 1 atm pressure, this length is $l_c \approx 2$ mm. Everyday observations of this length is possible, e.g. drops hanging from the ceiling after a hot shower is of this size.

Continuing in the capillary region, another ratio of interest is the Capillary number,

$$Ca = \frac{\eta U}{\sigma}, \tag{1.16}$$

where $\eta = \rho\nu$ is the dynamic viscosity. Here Ca describe the ratio of viscous forces to surface tension forces. A drop moving down an inclined plane will deform (in part) due to viscous forces as Ca increases, whereas the shape will be near spherical for low values (assuming other relevant quantities are accordingly small).

In Part II, drops impacting a fluid surface will be considered. The impact dynamics can be simplified in some parameter region, and to characterize this, the Weber number is used. It is the ratio between a fluids inertia and its surface

tension,

$$We = \frac{\rho U^2 L}{\sigma}. \tag{1.17}$$

For $We \ll 1$ the dynamics are governed by the surface tension. This means, for example, that we expect drop shapes to quickly reach equilibrium. Another quantity related to droplet impact is the Ohnesorge number,

$$Oh = \frac{\sqrt{We}}{Re} = \frac{\eta}{\sqrt{\rho\sigma L}}. \tag{1.18}$$

This number was first considered when Ohnesorge studied the breakup of a liquid jet, and it arises when describing the ratio of two timescales. The first being the characteristic time for the breakup of an inviscid fluid jet (as considered by Lord Rayleigh [6]). The other scale is the visco-capillary characteristic time. Small values of Oh indicates a lesser degree of dependence on the viscosity, compared to inertial and surface tension effects.

We now turn the attention towards an analytic description of the oscillations of a suspended liquid drop. Through perturbation methods, the influence of having a temperature dependent surface tension is investigated for an inviscid, incompressible fluid. Droplet oscillations will also be an important phenomenon to consider in Part II, so it is justified to consider some of the details here.

Chapter 2

An oscillating drop: analytical approach

The description of an inviscid, incompressible, oscillating drop was first considered by Rayleigh in 1879 [6]. Others have later treated the subject with slightly different approaches, but they all confirm the final expression for the most important oscillatory mode [2, 1]. Miller and Scriven [7] examined extensively the oscillatory modes for several conditions, e.g. a drop of high viscosity immersed in a low viscosity fluid, or a cavity in an inviscid fluid.

In the following chapter, the result of Rayleigh is confirmed (although it is obtained in a slightly different way); a geometric perturbation is imposed in order to determine the most dominant oscillatory mode. Then follows a thermal perturbation to determine the effect of having a temperature dependent surface tension. In both cases we consider an inviscid drop of density ρ, pressure p and velocity potential ψ. The drop is immersed in another fluid with corresponding properties, $\tilde{\rho}$, $\tilde{p}$ and $\tilde{\psi}$. Figure 2.1 shows a schematic of the situation. In the following three cases we find the perturbed versions of the velocity potential,

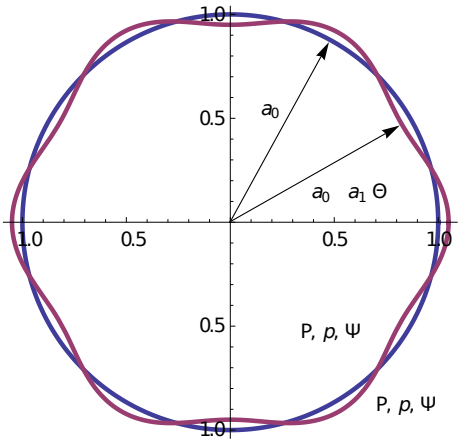

Figure 2.1: Schematic of the setup with azimuthal symmetry. a_0 is the initial radius, $a_0+a_1(\theta)$ is the perturbed radius of the drop. The physical properties of the drop are ρ, p and ψ, and for the fluid outside $\tilde{\rho}$, $\tilde{p}$ and $\tilde{\psi}$. The drawn oscillating function is $0.95 + 0.1\cos(3\theta)^2$

pressure, curvature and surface tension. The expansions to first order are

$$p = p_0 + p_1, \tag{2.1a}$$
$$\psi = \psi_0 + \psi_1, \tag{2.1b}$$
$$\tilde{p} = \tilde{p_0} + \tilde{p_1}, \tag{2.1c}$$
$$\tilde{\psi} = \tilde{\psi_0} + \tilde{\psi_1}, \tag{2.1d}$$
$$\kappa = \kappa_0 + \kappa_1, \tag{2.1e}$$
$$\sigma = \sigma_0 + \sigma_1. \tag{2.1f}$$

Here κ is the mean curvature of interface. The above quantities are related through a kinematic boundary condition and the linearized Young-Laplace equation, Eq. (1.9), which describes the pressure jump across the interface

$$p(a) - \tilde{p}(a) = \sigma\kappa. \tag{2.2}$$

2.1 Geometric perturbation

The objective is to determine the most dominant oscillatory mode of the geometrically perturbed interface, Fig. (2.1) shows the schematic of the set-up along with a specific perturbation of the interface. We assume that the surface

tension is constant in the following, i.e. $\sigma_1 = 0$. When the expanded fields are inserted in Eq. (2.2) we get

$$p_0 - \tilde{p}_0 = \sigma\kappa_0 \tag{2.3a}$$

$$p_1 - \tilde{p}_1 = \sigma\kappa_1. \tag{2.3b}$$

In the following, a spherical coordinate system is chosen, and no angular symmetry is assumed, hence Fig. (2.1) is drawn in polar coordinates for increased visual clarity.

For the zero order problem the velocity inside and outside the drop is zero, leading to p and $\tilde{p}$ being constant. Eq. (2.3a) then determines the pressure inside the drop,

$$p_0 = \tilde{p_0} + \frac{2\sigma}{a_0}. \tag{2.4}$$

The interface between the inner and outer fluid is described by the function $r = a_0 + a_1 = a_0 + \zeta(\theta, \phi, t)$, and we will now assume that ζ is some non-zero small disturbance and consider the consequenses. Through continuity we have that the velocity potentials must satisfy the Laplace equation

$$\nabla^2\psi_1 = 0, \tag{2.5a}$$

$$\nabla^2\tilde{\psi_1} = 0. \tag{2.5b}$$

Note that the pressures also satisfies the Laplacian. We describe the interface disturbance in the following way

$$\zeta(\theta, \phi, t) = \sum_{l=0}^{\infty} C_l S_l(\theta, \phi)\, \mathrm{e}^{-\beta_l t}, \tag{2.6}$$

where C_l is some constant, $S_l(\theta, \phi) = \sum_{m=-l}^{l} B_{lm} Y_l^m(\theta, \phi)$ are the surface harmonics of order l [8]. We use the surface harmonics as a basis since both pressure and velocity potential satisfy the Laplacian in spherical coordinates.

The linearized inviscid Navier-Stokes equation for both regions is

$$\boldsymbol{\nabla}\rho\partial_t\psi = -\boldsymbol{\nabla}p. \tag{2.7}$$

Since the system is linear we may assume the perturbed fields to be of the same harmonic form, $\mathrm{e}^{-\beta_l t}$, as the disturbance. Thus the general solutions to Eqs. (2.5a) and (2.5b) in spherical coordinates are

$$\psi_1 = \sum_{l=0}^{\infty} A_l \left(\frac{r}{a}\right)^l \mathrm{e}^{-\beta_l t} S_l(\theta, \phi), \tag{2.8a}$$

$$\tilde{\psi_1} = \sum_{l=0}^{\infty} \tilde{A}_l \left(\frac{r}{a}\right)^{-l-1} \mathrm{e}^{-\beta_l t} S_l(\theta, \phi), \tag{2.8b}$$

The solutions in Eqs. (2.8a) and (2.8b) are finite for $r \to 0$ and zero for $r \to \infty$, as we would expect. The objective is now to determine the complex frequency of the wave, β_l.

The expansion of the curvature due to ζ is

$$\kappa = \kappa_0 + \kappa_1 = \kappa_0 + \frac{\left(L^2 - 2\right)}{a^2}\zeta, \tag{2.9}$$

where $L^2 = \frac{\partial_\phi^2}{\sin^2\theta} + \frac{\partial_\theta(\sin\theta\partial_\theta)}{\sin\theta}$ is the spherical Laplacian [9]. Later we shall use the fact that

$$L^2 Y_l^m = l(l+1)Y_l^m. \tag{2.10}$$

By integrating Eq. (2.7) from $a-\epsilon$ to $a+\epsilon$ we obtain the boundary condition (Eq. (2.2)) to zeroth and first order

$$p_0(a) - \tilde{p_0}(a) = \sigma\kappa_0 = \frac{2\sigma}{a}, \tag{2.11a}$$

$$p_1(a) - \tilde{p_1}(a) = \sigma\kappa_1 = \frac{\sigma}{a^2}\left(L^2 - 2\right)\zeta, \tag{2.11b}$$

The disturbance at the interface is related to the velocity potential (and therefore to the pressure) through the following kinematic boundary condition

$$v_r = \partial_t\zeta = \partial_r\psi. \tag{2.12}$$

Using this, along with the given interfacial perturbation, Eq. (2.6), and the velocity potentials, Eqs. (2.8a) and (2.8b), we can determine the coefficients A_l and $\tilde{A}_l$,

$$A_l = -C_l\beta_l\frac{a}{l}, \tag{2.13a}$$

$$\tilde{A}_l = C_l\beta_l\frac{a}{l+1}. \tag{2.13b}$$

Before using Eq. (2.11b) to determine the oscillating frequency, we write out the terms; the pressures at $r = a$ are

$$p_1 = -\sum_{l=0}^{\infty}\rho\beta_l^2 C_l\frac{a}{l}\mathrm{e}^{-\beta_l t}S_l\left(\theta,\phi\right), \tag{2.14a}$$

$$\tilde{p_1} = \sum_{l=0}^{\infty}\tilde{\rho}\beta_l^2 C_l\frac{a}{l+1}\mathrm{e}^{-\beta_l t}S_l\left(\theta,\phi\right). \tag{2.14b}$$

The curvature term is

$$(L^2-2)\zeta = \sum_{l=0}^{\infty}\left(l(l+1)-2\right)C_l\mathrm{e}^{-\beta_l t}S_l\left(\theta,\phi\right). \tag{2.15}$$

This means that for each l, we have

$$\beta_l^2 = -\frac{\sigma}{a^3} \cdot \frac{l(l+1)-2}{\rho/l + \tilde{\rho}/(l+1)}. \tag{2.16}$$

In the limit of $\tilde{\rho} \to 0$ we obtain,

$$\beta_l^2 = -\frac{\sigma}{a^3\rho} l\,(l+2)\,(l-1)\,. \tag{2.17}$$

Here $l = \{0, 1, 2, \ldots\}$. Since the fluid is incompressible, $l = 0$ is not possible. For $l = 1$ there is no oscillation and the motion is simply translational. The lowest oscillatory mode is therefore $l = 2$, which is 5-fold degenerate. Notice how the function $f(l) = l(l+2)(l-1)$ is a monotonically increasing function for $l > 1$. Consequently, β is a complex number, resulting in periodic oscillations rather than decaying. Since the calculations have been done for an inviscid fluid, this was also expected. The slowest vibrating mode has a frequency of

$$f_2 = \frac{1}{2\pi}\sqrt{\frac{8\sigma}{a^3\rho}}. \tag{2.18}$$

A water droplet with a diameter of 5 mm oscillates at around 10 Hz.

2.2 Thermal perturbation

We assume azimuthal symmetry, and as such the temperature field is a function of r and θ only. In general the temperature is written as

$$T = T_0 + \mathrm{Re}\left[\Delta T f\,(\cos\theta)\,\mathrm{e}^{i\Theta t}\right], \tag{2.19}$$

where $\Delta T = T(\boldsymbol{r}) - T_0$, Θ is the forcing frequency, and f is some function of $\cos\theta$. Since the surface tension is a function of temperature we expand this as a Taylor series around T_0,

$$\sigma(T) = \sigma_0\left[1 + \alpha f(\cos\theta)\right], \tag{2.20}$$

where $\alpha = {}^{\partial_T\sigma_0}/_{\sigma_0}\Delta T$. Some typical values for an air/water interface is given in Table 2.1. The perturbation parameter when $\Delta T = 10℃$ and $T_0 = 20℃$ is then $\alpha = 2.25 \cdot 10^{-1}$.

Static temperature field

At the interface $r = a_0$, we still have

$$p - \tilde{p} = \kappa\sigma. \tag{2.21}$$

T_0 [℃]	σ [N/m]	$\partial_T \sigma/\sigma$ [K^{-1}]
20	0.0728	2.25×10^{-2}
30	0.0712	2.30×10^{-2}
40	0.0696	2.50×10^{-2}
50	0.0679	2.57×10^{-2}

Table 2.1: Typical values for air/water interface, taken from [10].

Expanding the fields gives

$$(p_0 - \tilde{p}_0) + \alpha\,(p_1 - \tilde{p}_1) = (\sigma_0 + \alpha\sigma_1)\,(\kappa_0 + \alpha\kappa_1)\,. \tag{2.22}$$

We then sort in orders of α and linearize

$$p_0 - \tilde{p}_0 = \sigma_0\kappa_0, \tag{2.23a}$$
$$p_1 - \tilde{p}_1 = \sigma_0\kappa_1 + \sigma_1\kappa_0. \tag{2.23b}$$

Since there is no time-dependence in this case, the left hand side of Eq. (2.23b) is zero. From Eq. (2.9) we have an expression for κ_1, and if we assume that the displacement of the interface is of the form given in Eq. (2.6) with $\beta_l = 0$, the following relation for the coefficients is obtained

$$C_l = \frac{2a_0^2}{\sigma_0}\frac{1}{l(l+1)-2}D_l, \tag{2.24}$$

Here we have expanded the first order surface tension correction, σ_1, as

$$\sigma_1(\theta) = \sum_{l=0}^{\infty} D_l P_l(\cos\theta). \tag{2.25}$$

If we choose a simple temperature profile at the interface, e.g. $f_1(\cos\theta) = \cos^2\theta$, then

$$T = T_0 + \Delta T \cos^2\theta, \tag{2.26}$$

leading to the coefficients

$$\begin{aligned} D_0 &= \frac{1}{3}\sigma_0 \\ D_1 &= 0 \\ D_2 &= \frac{2}{3}\sigma_0 \\ D_l &= 0,\ l > 2 \end{aligned}$$

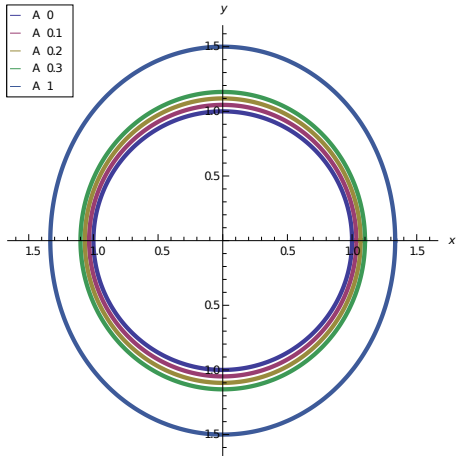

Figure 2.2: Eq. (2.28) shown for different values of the perturbation parameter α. The shape becomes increasingly elongated in the y-direction, and the shape for $\alpha = 1$ is merely shown to illustrate this.

We can now compute the first order correction to the radius which, with the specific temperature field given in Eq. (2.26), gives

$$a = a_0 \left[1 + \alpha \left(\frac{1}{2} - \frac{1}{6} \cos^2 \theta \right) \right]. \tag{2.28}$$

In Fig. (2.2) static shapes of the drop as given in Eq. (2.28) is shown.

Time dependent temperature field

When forcing the system with a frequency $\Theta \neq 0$, the temperature is prescribed in Eq. (2.19). This means that the first order correction to the surface tension is

$$\sigma_1 (\theta) = \alpha \sigma_0 f (\cos \theta) \, \mathrm{e}^{i\Theta t}. \tag{2.29}$$

The function f can be written as a sum of Legendre polynomials with coefficients E_l. Again we have assumed azimuthal symmetry, and so the first order pressures

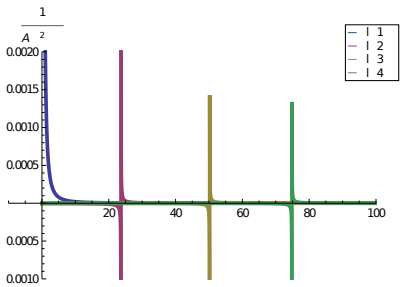

Figure 2.3: The $1/\left(A\Theta^2+\sigma\right)$ part of Eq. (2.32) as a function of Θ.

at the interface (which could now be non-zero) becomes

$$p_1(a) = -\rho \sum_{l=0}^{\infty} i\Theta A_l P_l\left(\cos\theta\right) \mathrm{e}^{i\Theta t}, \tag{2.30a}$$

$$\tilde{p}_1(a) = -\tilde{\rho} \sum_{l=0}^{\infty} i\Theta \tilde{A}_l P_l\left(\cos\theta\right) \mathrm{e}^{i\Theta t}. \tag{2.30b}$$

The relation at the interface is Eq. (2.23b), where the perturbation to the radius is unknown,

$$a_1\left(\theta\right) = \sum_{l=0}^{\infty} F_l P_l\left(\cos\theta\right) \mathrm{e}^{i\Theta t}. \tag{2.31}$$

Inserting into Eq. (2.23b) and solving for the unknown coefficients F_l as a function of the forcing frequency gives

$$F_l\left(\Theta\right) = \frac{2}{a_0} E_l \left[\rho\Theta^2 \frac{a_0}{l} - \tilde{\rho}\Theta^2 \frac{a_0}{l+1} + \frac{\sigma_0}{a_0^2}\left(2 - l(l+1)\right)\right]^{-1}. \tag{2.32}$$

It is now possible to compute the coefficients of the interface disturbance, and also to find the frequency for which this displacement is greater.

Eq. (2.32) is a Lorentzian function,

$$F_l\left(\Theta\right) = k \frac{1}{A\Theta^2 + \sigma}, \tag{2.33}$$

where $k = {}^{2E_l}/_{a_0^2}$, $A = {}^{\rho}/_{l} - {}^{\tilde{\rho}}/_{l+1}$ and $\sigma = {}^{\sigma_0}/_{a_0^3}(2 - l(l+1))$. The resonance frequencies for each mode coincide with the frequency found for the geometrical case, Eq. (2.16). For the water drop suspended in air, these resonances are seen in Fig. (2.3).

2.3 Dimensional and scaling considerations

Another way of achieving the oscillation frequency of an inviscid drop is to use dimensional analysis or scaling arguments. The fundamental parameters in the problem, and their units, are

$$\begin{aligned} [\sigma] &= \tfrac{\text{Energy}}{\text{Area}} &&= \frac{M}{T^2} \\ [\rho] &= \tfrac{\text{Mass}}{\text{Volume}} &&= \frac{M}{L^3} \\ [a] &= \text{Length} &&= L \\ [\omega] &= \tfrac{1}{\text{Time}} &&= \frac{1}{T}. \end{aligned}$$

According to Buckinghams theorem, this leads to $4-3=1$ dimensionless group, in which ω relates to the rest of the parameters in the following way

$$\omega = k\sqrt{\frac{\sigma}{a^3\rho}}, \tag{2.34}$$

where k is some constant. This could also have been obtained by equating the kinetic energy to the surface energy of the system, i.e.

$$\frac{4}{3}\pi a^3 \rho U^2 = \sigma a^2 \pi.$$

Here U is the velocity of the interface, which is approximated as $U = a\omega$. This leads to

$$\omega = \sqrt{\frac{3\sigma}{4a^3\rho}}.$$

Having described the relatively simple case of the oscillations an inviscid droplet with surface tension in three different ways, the focus is now turned towards solving the full Navier-Stokes equations. This is done in the next Chapter, where a numerical Finite Element Method is developed.

Chapter 3

An oscillating drop: numerical approach

This chapter explains the method by which a drop of liquid can be modeled in the Finite Element Method (FEM) program COMSOL (version 4.2). The implementation of the governing partial differential equations (PDEs) in a FEM, along with the underlying numerical theory, is presented. The idea behind this chapter is to give an overview of the FEM theory used in the modeling, but for more extensive insight, the reader is referred to [11], [12] and [13].

In the following, interactions with a solid is not considered, since this is the topic of chapter 5.

The initial geometry in the following is a liquid drop in an elliptic shape. Then surface tension and viscous damping should act to minimize the volume. Remembering the result in the previous chapter (although for an inviscid drop), the oscillatory motion of the drop is expected to be damped and result in a circular shape after some time.

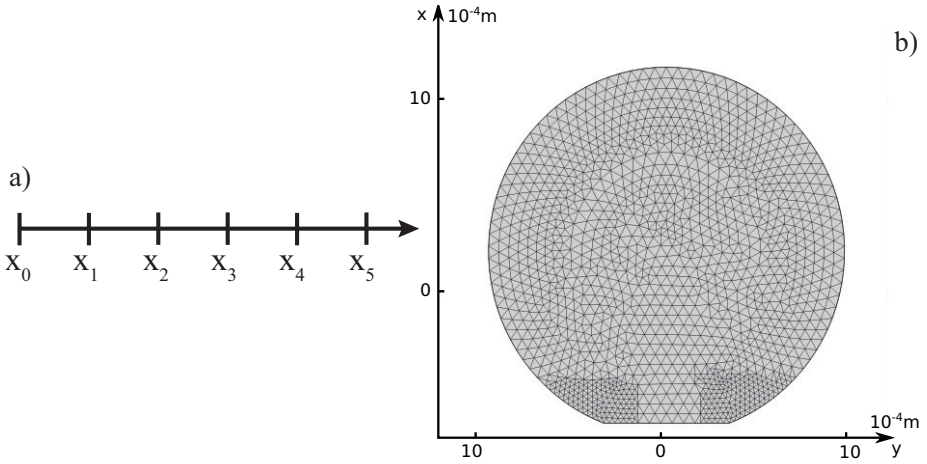

Figure 3.1: Discretization of domains. a) the one-dimensional interval with $M = 5$ elements and $N = 6$ nodes. b) a two-dimensional domain with approximately $M = 2000$ elements and $N = 2000$ nodes.

3.1 The Finite Element Method

The equations to be solved can generally be written as

$$D\mathbf{u}(\mathbf{x}) = \mathbf{f} \quad \text{on} \quad \Omega \tag{3.1}$$

$$B\left[\mathbf{u}(\mathbf{x}), \partial_j \mathbf{u}(\mathbf{x})\right] = 0 \quad \text{on} \quad \Gamma, \tag{3.2}$$

where Ω and Γ is the domain and boundary, respectively. The operator D is a differential operator which, for simplicity, only involves derivatives up to second order. Eq. (3.2) represents the boundary conditions, and ∂_j is the spatial derivative with respect to the $j = (x, y, z)$ direction.

The fundamental idea is to approximate the solution $\mathbf{u}(\mathbf{x})$ by a linear combination of a finite set of basis functions $\phi(\mathbf{x})$, and the standard way of achieving this requires a discretization of the computational domain into a mesh, two examples of which is shown in Figure 3.1. Both domains shown consists of a number of elements (denoted M) and nodes (N), and in 1D the elements are intervals whereas in 2D they are triangular. Mesh generation is practically an area of interest in its own right, so in the following, the meshing techniques of COMSOL has been used. The density of a mesh should be increased in regions of the domain where the solution is expected to have larger gradients, requiring a finer spatial resolution. In the following we consider the one dimensional general case, i.e. $\mathbf{u}$ and $\mathbf{f}$ only have one component.

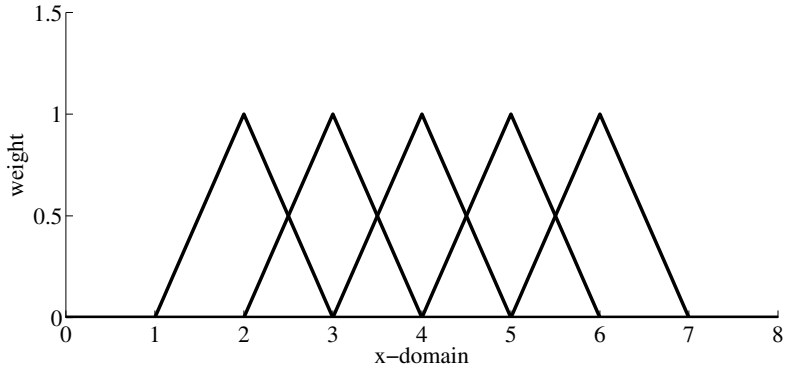

Figure 3.2: Basis functions for the one dimensional case.

The solution is now approximated at each node by using so-called basis functions. These functions must have compact support, i.e. the i'th basis function $\phi_i(\mathbf{x})$ is only non-zero in mesh elements containing the i'th node. An example of basis functions on a one-dimensional domain is shown in Figure 3.2, where the chosen basis consists of piece wise linear functions. Finding an appropriate function space for the basis functions can be done by considering the "weak" solutions of a PDE. The term weak should be understood as an approximate solution, since the restrictions on the solution in terms of differentiability is looser than for the original strong solution. Consider a function space $V : \Omega \to \mathbb{R}$ with the norm

$$\langle u, v \rangle = \int_\Omega u(\mathbf{x}) v(\mathbf{x}) dx. \tag{3.3}$$

In principle, the weak form of a PDE is found by multiplying the equation by a test function, v, and integrating over the domain. For our generic PDE Eq. (3.1), we get

$$\langle Du, v \rangle = \langle f, v \rangle . \tag{3.4}$$

As an example, consider the Laplace operator $D = \nabla^2$. Now, integration by parts yields

$$\left\langle \nabla^2 u, v \right\rangle = \int_\Omega v \nabla^2 u d\mathbf{x} = \int_{\partial\Omega} v \mathbf{n} \nabla u d\mathbf{x} - \int_\Omega \nabla u \cdot \nabla v d\mathbf{x}, \tag{3.5}$$

where $\mathbf{n}$ is a normal vector on the boundary $\partial\Omega$. The first term on the right hand side is zero for suitable choice of test functions v, thus the differentiability requirement on u has been lowered by one order. The function u is called a weak solution to the problem. It is noteworthy that a strong solution is also a weak solution, but the converse is not true. We now seek solutions that are a

linear combination of the chosen basis

$$u(\mathbf{x}) \approx \sum_{i}^{N} \hat{u}_i \phi_i(\mathbf{x}), \tag{3.6}$$

where the test function can be written as

$$v(\mathbf{x}) = \sum_{i} a_i \phi_i(\mathbf{x}). \tag{3.7}$$

Eq. (3.4) now becomes

$$\sum_{i} \langle D\phi_i, \phi_j \rangle \hat{u}_i = \langle f, \phi_i \rangle, \ \forall i, j \in \mathbb{N}. \tag{3.8}$$

This is a system of equations with unknowns $\hat{u}_i$, which can be solved for. Generalizing to D dimensions, the system is

$$\mathbf{A}\hat{\mathbf{u}} = \hat{\mathbf{f}}, \tag{3.9}$$

where $\hat{\mathbf{u}} = (\hat{u}_1, \ldots, \hat{u}_D)$ is a vector of length D to be solved for, $\mathbf{A}$ is a matrix with known entries $A_{ij} = \langle D\phi_j, \phi_i \rangle$, and $\hat{f}_i = \langle f, \phi_i \rangle$ contains the forcing terms of the system. Since the basis functions had a compact support, the matrix $\mathbf{A}$ will be sparse, allowing for fast computations. Nonlinear problems are solved using Newtons iterative method to successively obtain a more accurate solution [11].

Meshes on time-dependent domains

When dealing with two fluid phases (e.g. liquid and gas), there are a number of ways to track the interface. The frameworks presented here are discussed in even more detail in [14], [15] and [16]. We expect the interface to deform somewhat during the simulations, so a mesh that deforms with the fluid was employed. The chosen technique is called the Arbitrary Lagrangian-Eulerian (ALE) reference frame. In a usual Lagrangian description, the nodes of the mesh, χ, is advected with the calculated fluid velocity,

$$\partial_t \chi = \mathbf{u}(\chi, t). \tag{3.10}$$

This formulation has the disadvantage of a quickly distorted mesh, since there are essentially no constraints on the displacement of the nodes. A re-meshing of the domain is therefore often required. If, however, the nodes inside the domain are advected in some smooth way, we obtain the ALE framework. The boundary nodes are still advected with the corresponding fluid velocity. To illustrate the coordinate transformation from the ALE frame to a static Eulerian frame, in

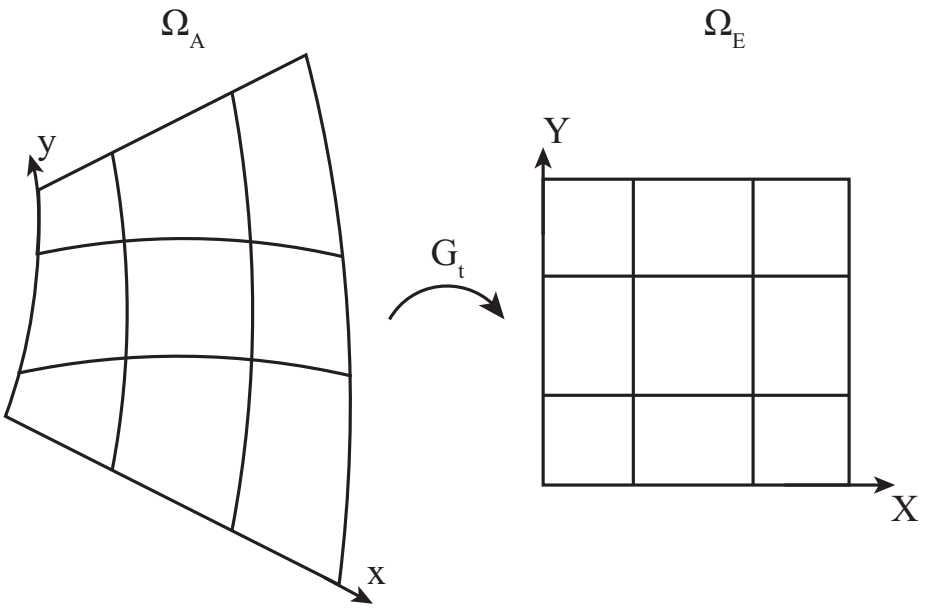

Figure 3.3: The mapping G_t takes the deformed ALE mesh into the static Eulerian configuration.

which we can solve the problem numerically, consider the example of a scalar advection diffusion problem,

$$\partial_t v - \nabla^2 v + (\mathbf{u} \cdot \nabla) v = 0 \tag{3.11}$$

$$\nabla \cdot \mathbf{u} = 0. \tag{3.12}$$

Here $\mathbf{u}$ is some convection velocity. We furthermore assume that the above equations are supplemented with some suitable boundary and initial conditions. The function v in Eq. (3.11) is defined in an Eulerian reference frame, and we now formulate the problem in the ALE frame. To do this, define a homeomorphic (continuous, bijective, and with a continuous inverse) mapping $G_t : \Omega_A \to \Omega_E$, which takes points in the ALE frame into the Eulerian frame (see Figure 3.3),

$$G_t(\mathbf{x}) = \mathbf{X}(\mathbf{x}, t). \tag{3.13}$$

Essentially, switching to the ALE frame results in an added convective term when computing the material derivative since both mesh and fluid moves relative to the Eulerian laboratory frame. The example, Eq. (3.11), becomes

$$\partial_t v - \nabla^2 v + (\mathbf{u} \cdot \nabla) v - (\mathbf{u}_A \cdot \nabla) v = 0, \tag{3.14}$$

where $\mathbf{u}_A = \frac{\partial \mathbf{x}}{\partial t}$ is the particle velocity in the ALE frame, and $\mathbf{u}$ is the convective velocity in the Lagrangian frame. The reader should, for an in-depth treatment

of this subject, consult reference [16] in which the ALE method along with mesh-generation techniques are presented in a clear manner.

The next section sets up the geometry of a levitating droplet and derives the weak formulation of the Navier-Stokes equation with boundary conditions for a free surface.

3.2 Geometry and governing equations

The drop is initially put in a state where it is an ellipse, and the semi-major and semi-minor axis have lengths $a = 2.0000 \cdot 10^{-3}$ m and $b = 1.0000 \cdot 10^{-3}$ m, respectively (see Figure 3.4). The interior of the domain is denoted Ω, and the free boundary Γ_{free}. At all times we define a normal and a tangent vector, $\mathbf{n}(\mathbf{x}, t)$ and $\mathbf{t}(\mathbf{x}, t)$, at each point on the boundary of the drop. In the formulation of the problem, a non-dimensionalized version of the Navier-Stokes equations is used. However, all results have been converted back to the original dimensional variables.

As the number of nodes increases, the computed area approaches the theoretical area. The initial theoretical area of the drop can be calculated as

$$A_{\text{theoretical}}/\pi = 2ab = 6.2832 \cdot 10^{-6}\text{m}^2.$$

The numerical area is calculated by integrating along $\partial\Omega(t = 0)$, yielding

$$A_{\text{mesh 1}}/\pi = 6.2790 \cdot 10^{-6}\text{m}^2,$$

$$A_{\text{mesh 2}}/\pi = 6.2816 \cdot 10^{-6}\text{m}^2,$$

where mesh 1 consists of 2446 nodes and mesh 2 consists of 6344 nodes.

The non-dimensionalized Navier-Stokes equations and incompressibility condition is

$$Re\left(\partial_t \mathbf{u} + (\mathbf{u} \cdot \nabla)\,\mathbf{u}\right) = \nabla \cdot \mathbf{S}, \tag{3.15}$$

$$\nabla \cdot \mathbf{u} = 0, \tag{3.16}$$

where no additional volume force is added, and the hats denoting nondimensional quantities have been omitted for clarity. The corresponding nondimensional boundary conditions on Γ are the following

$$\begin{aligned} \mathbf{n} \cdot \mathbf{S} &= \frac{1}{Ca}\mathbf{n}\nabla_s \cdot \mathbf{n} = \mathbf{n}\kappa \\ \mathbf{n} \cdot \mathbf{S} \cdot \mathbf{t} &= 0. \end{aligned} \tag{3.17}$$

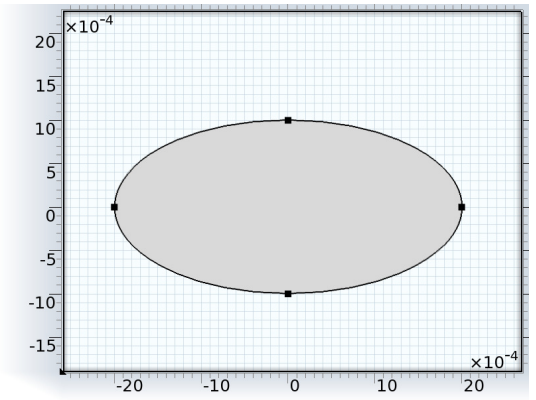

Figure 3.4: The geometry of the drop in its initial state is an ellipse. The units on the x- and y-axis is meter.

Here $\mathbf{n}$ and $\mathbf{t}$ are the normal and tangent vector of the free surface, and ∇_s is the surface divergence operator, sometimes written as $\nabla_s = \nabla - \mathbf{n}\frac{\partial}{\partial n}$, i.e. it is the divergence operator restricted to the surface Γ. Another way of writing this operator is $\nabla_s = \mathbf{t}\partial_s$, where ∂_s is the derivative with respect to the parameterization-parameter of the interface. This means that $\nabla_s \cdot \mathbf{n} = \kappa$, where κ is the curvature of the surface. The first boundary condition is the Young-Laplace equation on the free surface, and the assumption that there are no Marangoni flows is stated in the second condition.

The weak formulation

To implement the model in COMSOL, it is necessary to recast the equations into the weak formulation. This is done by choosing suitable test functions $\mathbf{v} = (v_1, v_2)^T$ and q, multiplying these with Eqs. (3.15) and (3.16) and integrating over the computational domain.

$$\int_\Omega Re\partial_t \mathbf{u} \cdot \mathbf{v} d\Omega + \int_\Omega Re\left(\mathbf{u} \cdot \nabla\right)\mathbf{u} \cdot \mathbf{v} d\Omega = \int_\Omega \left(\nabla \cdot \mathbf{S}(\mathbf{u}, p)\right) \cdot \mathbf{v} d\Omega. \tag{3.18}$$

$$\int_\Omega \left(\nabla \cdot \mathbf{u}\right) q d\Omega = 0. \tag{3.19}$$

To avoid dealing with second derivatives of $\mathbf{u}$, the integral with the stress tensor is considered. We make use of the following identity,

$$\left(\nabla \cdot \mathbf{S}\right) v = \nabla \cdot \left(\mathbf{S}v\right) - \mathbf{S} \cdot \left(\nabla v\right), \tag{3.20}$$

To realize how this identity can be used along with the divergence theorem, we write out the right-hand side integral in Eq. (3.18) as vectors,

$$\int_\Omega (\nabla \cdot \mathbf{S}(\mathbf{u}, p)) \cdot \mathbf{v} d\Omega = \int_\Omega \begin{pmatrix} \nabla \cdot (S_{11},\ S_{21})\, v_1 \\ \nabla \cdot (S_{12},\ S_{22})\, v_2 \end{pmatrix} d\Omega, \tag{3.21}$$

where S_{ij} is the ij'th component of the stress tensor. The identity in Eq. (3.20) is thus applicable for each component, and the integral becomes

$$\int_\Omega (\nabla \cdot \mathbf{S}(\mathbf{u}, p)) \cdot \mathbf{v} d\Omega = \int_\Gamma \mathbf{v} \cdot (\mathbf{n} \cdot \mathbf{S})\, d\gamma - \int_\Omega \mathbf{S} \cdot (\nabla \mathbf{v})\, d\Omega, \tag{3.22}$$

where $\mathbf{n}$ is the outward normal on the boundary Γ. The boundary part of Eq. (3.22) is now considered, and by invoking the boundary conditions from Eq. (3.17), we get

$$\int_\Gamma \mathbf{v} \cdot (\mathbf{n} \cdot \mathbf{S})\, d\gamma = \frac{1}{Ca} \int_\Gamma \kappa \mathbf{v} \cdot \mathbf{n} d\gamma \tag{3.23}$$

From the Frenet-Serret equations we have

$$\partial_s \mathbf{t} = \kappa \mathbf{n}, \tag{3.24}$$

where ∂_s denotes differentiation with respect to arc length. Using this in Eq. (3.23) and integrating by parts we get

$$\frac{1}{Ca} \int_\Gamma \mathbf{v} \cdot \partial_s \mathbf{t} ds = \frac{1}{Ca} - \int_\Gamma \mathbf{t} \cdot \partial_s \mathbf{v} ds + \frac{1}{Ca} \left[\mathbf{v} \cdot \mathbf{t}\right]_{\mathrm{cl}}, \tag{3.25}$$

where $[\cdot]_{\mathrm{cl}}$ means evaluated at the possible end-points of the boundary. When dealing with contact lines between solids and liquids, this part of the boundary integral is important, and will be retained. COMSOL has a built-in functionality for the surface divergence operator, and a final expression is obtained by using $\mathbf{t}\partial_s = \nabla_s$,

$$\frac{1}{Ca} \int_\Gamma \mathbf{t} \cdot \partial_s \mathbf{v} ds = \frac{1}{Ca} \int_\Gamma \nabla_s \mathbf{v} ds, \tag{3.26}$$

which is implemented in COMSOL by entering

$$\frac{1}{Ca}(\mathrm{test}(uTx) + \mathrm{test}(vTy)),$$

for the weak boundary term. We now state the problem in a variational formulation

$$a(\mathbf{u}, \mathbf{v}) = b(\mathbf{v}), \tag{3.27}$$

with

$$\begin{aligned} a(\mathbf{u},\mathbf{v}) &= \int_\Omega Re\partial_t \mathbf{u}\cdot\mathbf{v}d\Omega + \int_\Omega Re\,(\mathbf{u}\cdot\nabla)\,\mathbf{u}\cdot\mathbf{v}d\Omega + \int_\Omega \mathbf{S}\cdot(\nabla\mathbf{v})\,d\Omega \\ &\quad + \int_\Omega q\nabla\cdot\mathbf{u} \\ b(\mathbf{v}) &= \frac{1}{Ca}\int_\Gamma \nabla_s\mathbf{v}ds \end{aligned}$$

3.3 Results

In Figure 3.5 the drop evolution is shown in four steps, starting from $t = 0$ and ending at $t = 1$. From the initial ellipsoidal shape, surface tension and viscosity damping minimizes the energy, resulting in the spherical shape seen in panel d). Figure 3.6 shows a plot of $\frac{A(t)}{A(0)} - 1$, where $A(t)$ is the calculated area of the drop at all times and $A(0)$ is the initial area. The areas are computed by integrating over the time varying computational domain of the drop, $\Omega(t)$. Since the fluid is assumed incompressible we expect the area to be constant, however, this seems to be violated. The divergence of the velocity is not zero everywhere on the domain. Near the boundary, where mesh elements become more distorted, we observe this violation. Although the area is not constant, it should be noted that the observed fluctuation is on the order of 10^{-4} of the original area. By increasing the computational accuracy, or by resolving the domain with a finer mesh, this effect can be reduced to an insignificant level. Since the model behaves as expected and the volume change can be minimized, we now want to append it with a suitable boundary condition to allow for solid-liquid interactions. This is done in the next chapters, where the theory for structured surfaces is developed.

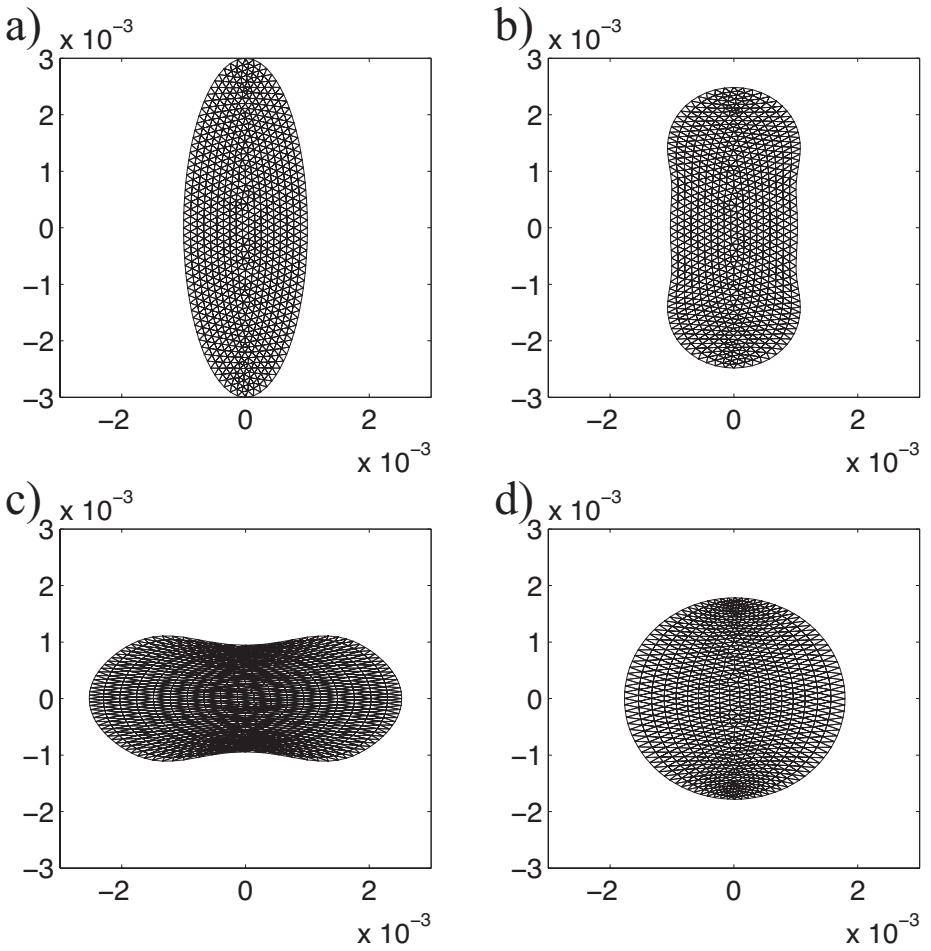

Figure 3.5: The geometry and mesh of the deformed drop at a) $t = 0$, b) $t = 4{\cdot}10^{-3}$, c) $t = 12{\cdot}10^{-3}$, and d) $t = 1$. From an initial ellipsoidal shape the drop minimizes its energy and becomes spherical.

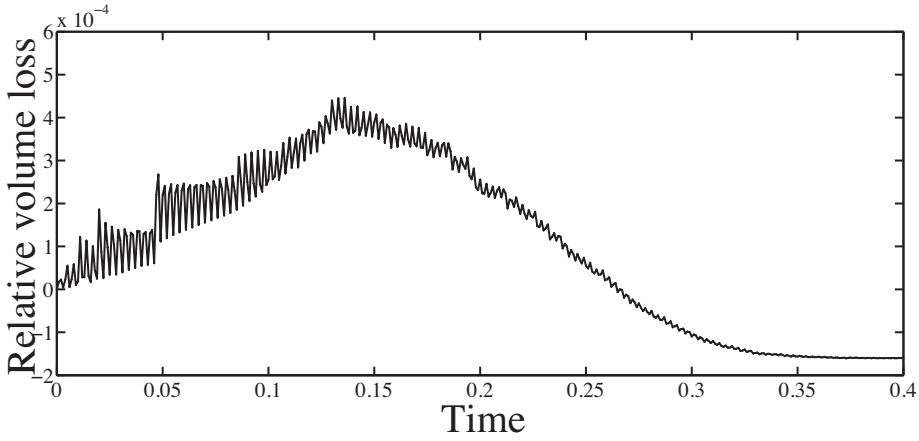

Figure 3.6: The area of the drop fluctuates as much as $\frac{A(t)}{A_0} = 10^{-4}$, where A_0 is the original area. This happens since the divergence of the velocity is not entirely zero, a violation that especially occurs near the boundary of the drop.

Chapter 4

Wetting of structured surfaces

The wetting behavior of a given substrate is a consequence of the interaction with (typically) two fluid phases on the surface, namely liquid and gas. The wetting properties of a given surface are always found with respect to some given liquid since, e.g., the chemical affinity for water to stick to a surface might not be the same as for yogurt.

The contact angle of a liquid residing on substrate is defined as the angle measured through the liquid, see Figure 4.1. A surface is hydrophobic with respect to some liquid if the contact angle of the liquid residing on the surface is above 90°, and super-hydrophobic when the angle is above 150°. Likewise, a hydrophilic material has a contact angle of less than 90°.

There are numerous accounts of wetting related properties in nature, the most famous of which is probably the lotus leaf, see Figure 4.2 [17]. The leaf utilizes a hierarchical structure on a hydrophobic material, resulting in a super-hydrophobic surface. When liquid is removed from the surface of the leaf, it takes along with it dirt and particles, a mechanism which is called self-cleaning. The Namib dessert beetle is another example where nature uses surface patterning. This beetle has developed alternating hydrophobic and hydrophilic regions on its back which allows for fog-collection on hydrophilibic areas, and subsequently transport of liquid to its mouth on the hydrophobic areas [18].

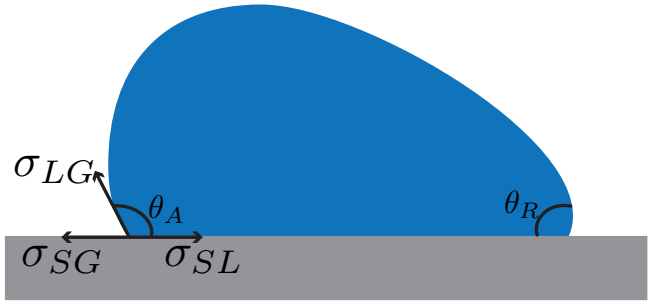

Figure 4.1: Schematic of a drop on a surface. The interfacial energies between liquid-solid (σ_{LS}), liquid-gas (σ_{LG}) and solid-gas (σ_{SG}) are show. The receding (θ_R) and advancing (θ_A) contact angle is also depicted.

Figure 4.2: An example of hydrophobicity: water droplets on a lotus leaf. The contact angle is above 90 °, and the water-repellency of the leaf is due to a hierarchical micro- and nanostructure. Copyright by tanakawho on Flickr.

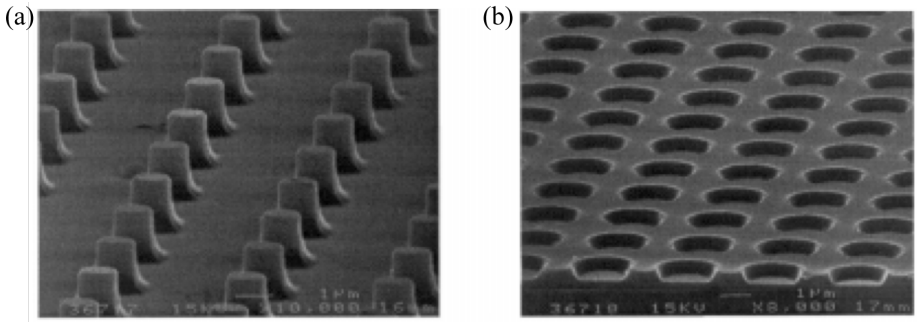

Figure 4.3: Scanning Electron Microscope images of two microstructured surfaces. (a) nearly cylindrical posts, and (b) shallow cavities. The width of the posts and the diameter of the cavities is approximately 1 μm. Copyright by Bico *et al.* [22].

This is an example of controlling phase transitions through texturing, and also having directional transport using gradients in the texture. Another delicate design is found on the wings of some butterfly species, where a flexible nano- and micro-structure results in directional adhesive forces. When the butterfly flaps its wings, liquid is removed from the surface, removing particles that would otherwise impair its flying capabilities [19].

In recent years the examples above, along with many others, have been an inspiration for the fabrication of micro- and nano-structured surfaces, two examples of which are shown in Figure 4.3. In this chapter, the theory of wetting on surfaces will be presented, and the influences of chemical and physical patterning is explained. We also introduce concepts relating to the dynamics of contact angles and the boundary condition at a solid-liquid interface.

Imagine a perfectly flat homogeneous surface, upon which a liquid is deposited. There are three phases involved, namely liquid, gas and solid. All interfaces between these phases have been formed at an energetic cost, and the interfacial energy between the phases are denoted σ_{LS}, σ_{LG}, and σ_{SG}, which are the liquid-solid, liquid-gas and solid-gas interfacial interfacial energies. Note that σ_{LG} was previously denoted σ. Figure 4.1 shows a schematic of the situation. A given drop can be stable over a range of contact angles, giving rise to a phenomena called contact angle hysteresis. We will return to this subject later in this section.

For now, consider the change in interfacial energy associated with some small displacement dx, see Figure 4.4. By minimizing the energy we derive Youngs

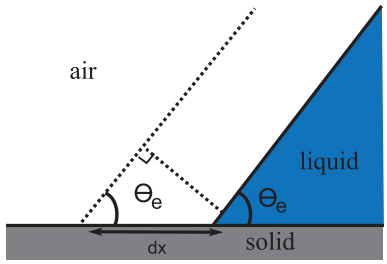

Figure 4.4: The situation where liquid, solid, and gas meets. If the liquid is displaced some infinitesimal length dx, we can set up the interfacial energies associated with this change. The surface is perfectly flat and chemically homogeneous.

formula for a static drop on a perfectly flat homogeneous surface,

$$\cos\theta_e = \frac{\sigma_{SG} - \sigma_{SL}}{\sigma_{LG}}. \tag{4.1}$$

Here θ_e is the Young contact angle. This expression has to be satisfied locally everywhere. The spreading parameter S is useful in determining the behavior of a deposited liquid,

$$S = \sigma_{SG} - (\sigma_{SL} - \sigma_{LG}) = \sigma_{LG}\,(k-1)\,, \tag{4.2}$$

where $k = \cos(\theta_e)$. Essentially, S measures the difference in surface energy of a substrate in its dry and wet form. For $S < 0$, the contact angle θ_e is defined, and the drop partially wets the surface. If $S > 0$, there is total wetting, and obviously the contact angle can not be defined. These phenomena are shown in Figure 4.5 through the parameter k.

Physical texturing

The description of the contact angle so far has been macroscopic and under the assumption of a perfectly flat and homogeneous substrate. Perfectly flat surfaces are, however, hard to realize, and typically there will be some degree of roughness on the surface. One of the first experiments that examined the influence of surface roughness on the apparent contact angle was performed by Robert and Rulon [20]. They measured advancing and receding contact angles as a function of surface roughness by successively heating a waxed surface, and concluded that roughness has a significant impact on the contact angle, and also on the observed hysteresis. In 1936 Wenzel [21] proposed a way of describing the apparent contact angle, θ, of a liquid on a chemically homogeneous surface,

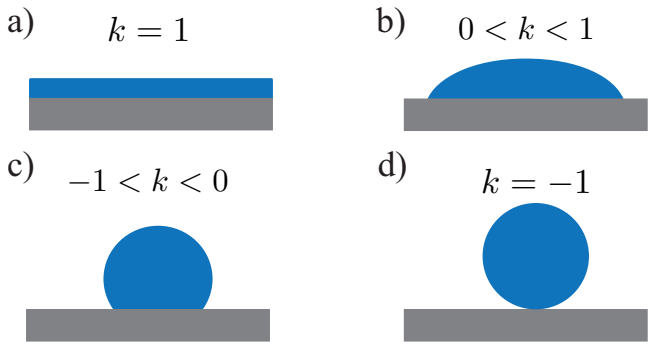

Figure 4.5: The four possible behaviors as a function of the parameter $k = \cos(\theta_e)$. a) For $k = 1$ the liquid totally wets the surface. b) Intermediate values, $0 < k < 1$ results in partial wetting with a contact angle less than 90°. c) The hydrophobic case of $-1 < k < 0$ results in a contact angle above 90°, and for d) $k = 1$, the liquid only contacts the surface at a single point.

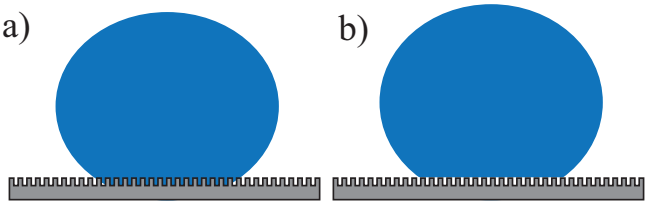

Figure 4.6: a) The Wenzel state where the drop has penetrated into the grooves of the surface. b) The fakir state where the drop is suspended on top of the physical textures.

but with physical texturing. The local contact angle is given by Eq. (4.1), and it is assumed that the characteristic size of the roughness is much smaller than that of the drop, and the liquid should furthermore penetrate into all grooves of the surface as it is depicted in Figure 4.6 a).

Consider again a small displacement dx, see Figure 4.7 a). The roughness is defined by the roughness factor, r, which is the ratio of the actual surface to the projected surface, so $r > 1$. The displacement leads to a change in energy dE, which is

$$dE = \sigma_{LG} dx \cos\theta + \sigma_{SL} r dx - \sigma_{SG} r dx.$$

Minimizing this energy yields

$$\sigma_{LG} \cos\theta = r \left(\sigma_{SG} - \sigma_{SL}\right),$$

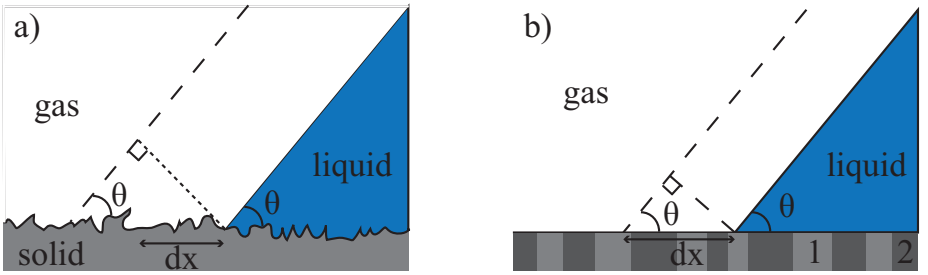

Figure 4.7: a) A closeup of the situation with a rough surface, where liquid, solid, and gas meets. If the liquid is displaced some infinitesimal length dx, we can set up the interfacial energies associated with this change. Adapted from [22]. c) Similar closeup for a heterogeneous surface consisting of material 1 and 2.

which then gives Wenzels formula

$$\cos\theta = r\cos\theta_e. \tag{4.3}$$

The apparent contact angle is proportional to the Young contact angle, and leads to an enhancement of the underlying properties of the surface; texturing lowers the contact angle of an originally hydrophilic material, and increases the contact angle of a hydrophobic surface.

Chemical texturing

The situation where the surface consists of regions with chemically different characteristics was treated by Cassie and Baxter [23, 24]. The surface is now considered perfectly flat and thought to be comprised of two materials. Let θ_{e1} and θ_{e2} denote the Young contact angle of these two materials, and let f_1 and f_2 be the fractional surface areas, i.e. $f_1 + f_2 = 1$. Again, it is assumed that the drop dimensions are much larger than the spread of the different regions of substance 1 and 2, see Figure 4.7 b).

Following the small displacement approach an expression is obtained for the energy variation,

$$dE = f_1\left(\sigma_{SL} - \sigma_{SG}\right)_1 dx + f_2\left(\sigma_{SL} - \sigma_{SG}\right)_2 dx + \sigma_{LG}\cos\theta dx,$$

where the subscripts 1 and 2 denote that the interfacial stresses correspond to regions 1 and 2. Minimizing yields the Cassie-Baxter equation

$$\cos\theta = f_1\cos\theta_{e1} + f_2\cos\theta_{e2}, \tag{4.4}$$

where f_1 and f_2 are the *propabilities* of sweeping are 1 and 2 during the displacement. The apparent contact angle lies in the interval $[\theta_{e1}, \theta_{e2}]$. If the Wenzel and Cassie-Baxter approaches are combined, a model for a rough, chemically heterogeneous surface is obtained.

A hydrophobic surface has higher wet surface energy than dry surface energy,

$$\sigma_{SG} < \sigma_{SL},$$

and relating this to the Young contact angle, Eq. (4.1), we get

$$\cos\theta_e = \frac{\sigma_{SG} - \sigma_{SL}}{\sigma_{LG}} < 0 \Rightarrow \theta_e > 90°.$$

When there is a tendency to have a dry surface, the liquid interface does not necessarily follow the underlying geometry. It is given that Youngs equation is satisfied locally at the solid-liquid contact line, but air can be trapped in the grooves underneath the drop, leading to a surface which can be considered as consisting of air and solid, i.e. a Cassie-Baxter situation and we use Eq. (4.4). This situation is also referred to as the fakir state [25], see Figure 4.6 b).

If Eq. (4.4) is used with $\theta_{e1} = \theta_e$, $\theta_{e2} = \pi$, $f_1 = \phi_s$ and $f_2 = 1 - \phi_2$, the result is

$$\cos\theta^* = \phi_s\left(\cos\theta_e + 1\right) - 1. \tag{4.5}$$

This equation leads to some interesting observations. First, when Youngs contact angle of the solid goes to 180°, so does the apparent contact angle,

$$\theta_e \to \pi \Rightarrow \theta^* \to \pi.$$

Second, if the solid fraction becomes very small, the apparent contact angle almost becomes 180°,

$$\phi_s << 1 \Rightarrow \theta^* \to \pi.$$

It should be noted, however, that creating a surface that would lead to an apparent contact angle of 180° is not physically realizable since this would imply either $\phi_s = 0$ or $\theta_e = 180°$. This is in contrast to Wenzels model, Eq. (4.3), which stated that an apparent contact angle of 180° is possible whenever the product of r and $\cos\theta_e$ is -1.

It is possible to examine the behavior of Eq. (4.5) as $\phi_s \to 0$ [26]. This is done by solving for the solid fraction,

$$\phi_s = \frac{\cos\theta^* + 1}{\cos\theta_e + 1} = \frac{\cos\theta^*}{k} + \frac{1}{k}. \tag{4.6}$$

Now $\phi_s = \phi_s(\theta^*)$. If it is assumed that $\cos\theta^* \to -1$ it is possible to expand Eq. (4.6):

$$\phi_s \approx \frac{1}{k}\left(\theta^* - \pi\right)^2,$$

which leads to an expression for the apparent contact angle.

$$\theta^* = \pi - \sqrt{\phi_s k} \tag{4.7}$$

At low solid fractions it is seen that the apparent contact angle varies very rapidly. This is one of the reasons why contact angles of 180° are impossible to obtain. Inserting $k = 1/2$ (corresponding to $\theta_e = 120°$) and $\phi_s = 0.1$, the apparent contact angle is 160°.

The above description has been a very idealistic approach into solid-liquid interactions. Naturally, a droplet is a three-dimensional object, and the solid-liquid-gas interface is therefore a line, instead of two points. Another complication is the fact that drops are observed to be stable over a range of contact angles.

Contact angle hysteresis

Multiple stable contact angles for a given droplet on a surface has been experimentally observed, and this effect is called contact angle hysteresis. It originates from pinning of the contact line at the physical or chemical textures of the surface, and is measured as the difference between the advancing and receding contact angle, see Figure 4.1,

$$\Delta\theta = \theta_A - \theta_R. \tag{4.8}$$

A drop of radius R sticking on a window is pinned due to the hysteresis effect. If the window is at an angle α with the horizon, the gravitational pull scales as $\rho g \sin\alpha R^3$. Similarly, the sticking force owing to contact angle hysteresis scales as $\sigma R(\cos\theta_R - \theta_A)$, and balancing these forces gives

$$\frac{R^2}{\Delta\theta} = l_c \sin\alpha, \tag{4.9}$$

where l_c is the capillary length. Assuming that the hysteresis effect is independent of drop size, we conclude that smaller drops sticks easier than bigger drops.

A liquid in the Wenzel state has an increased area of contact with the surface and the energy required to create liquid-gas interfaces is therefore also increased. This results in a stronger pinning on the surface due to a big hysteresis effect. The roll-off angle α_R is also increased in the Wenzel state. On the contrary, in the Casse-Baxter state, droplets have a significantly reduced area of contact with the solid, resulting in almost immediate roll-off ($\alpha_R \approx 1°$), due to a very low hysteresis effect. Typically, a droplet in the Wenzel state has a hysteresis

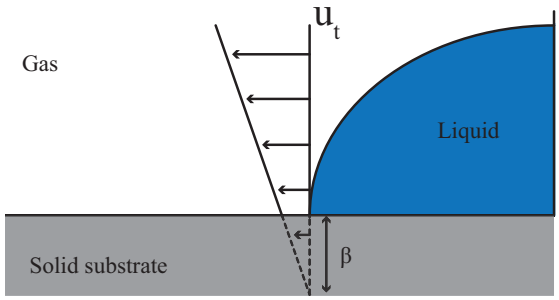

Figure 4.8: The Navier slip boundary condition gives rise to an effective fluid velocity at the solid-liquid boundary. The slip length β, is the distance below the surface where the fluid velocity would be zero (assuming a linear velocity profile).

effect ranging from $\Delta\theta = 50°$ to $\Delta\theta = 100°$, whereas drops in the Cassie state have $\Delta\theta = 5°$ to $\Delta\theta = 20°$ [27, 28].

Self cleaning surfaces are thus not only characterized by their static contact angle, but also by $\Delta\theta$; the most efficient self cleaning surfaces have a high static contact angle and a low hysteresis effect.

Slip length

In summary, the Cassie-Baxter fakir state traps air underneath the liquid, giving rise to a much smaller contact area with the solid resulting in a low degree of hysteresis. In this state, a moving fluid glides on the air trapped underneath it, and only contacts the solid in a small area [29]. Typically, solid-liquid interfaces have a no-slip boundary conditions, however, in the case of micro- and nano-structured surfaces, experiments have shown that there exists an effective slip length. This length is defined in the Navier boundary condition [3], and in a nondimensional form it is stated as

$$\mathbf{u} \cdot \mathbf{n} = 0 \tag{4.10}$$

$$\mathbf{u} \cdot \mathbf{t} = -\hat{\epsilon}\mathbf{n} \cdot \mathbf{S} \cdot \mathbf{t}. \tag{4.11}$$

The slip condition is a friction slip condition, equating the tangential velocity to the tangential shear stresses in the fluid. In full dimensions, $\hat{\epsilon}$ has units of x_0/η, i.e. $\epsilon = \hat{\epsilon}\frac{x_0}{\eta} = \frac{\beta}{\eta}$. The parameter β is denoted the slip length, and can be interpreted as a fictitious distance to the solid, i.e. the distance below the surface where the tangential velocity of the fluid is zero, see Figure 4.8. Setting

$\beta = 0$ results in the usual no-slip condition, but for $\beta \neq 0$ an intermediate slip is obtained. Recent experiments on spray-coated hydrophobic surfaces gave rise to slip lengths ranging from 39 μm to 213 μm [30] for liquid in the Cassie-Baxter state. These large slip lengths are accompanied by large drag reductions [31], which is another interesting application of hydrophobic surfaces.

This does not mean, however, that the no-slip condition is invalid for hydrophobic textured surfaces. The Navier slip condition should be seen as an approximation or smoothing of the stresses at the solid-liquid boundary when describing macroscopic flows. A complete description at all scales would involve no-slip conditions on solid-liquid boundaries, and a liquid-air surface penetrating slightly into the grooves of the surface, below the drop. However, setting up a numerical model of this complete description of the fluid flow would require a substantial amount of computational time, since all features at the microscopic level should be spatially resolved by a mesh. In the following chapter, we assume a drop with size on the order of millimeters is in the Cassie-Baxter state, and utilize the Navier slip condition to describe its macroscopic behavior.

Chapter 5

A droplet on a structured surface

In this chapter, we extend the model from the previous chapter to include a liquid-solid boundary. We investigate the behavior of the drop on an inclined plane, and also on a leveled surface with spatially varying contact angle. The text resembles to some extent the one found in the paper attached in Appendix A.2, but occasional in-depth explanations are given here. Furthermore, section 5.3 is not included in the paper.

5.1 Introduction

The dynamic behavior of drops on an inclined hydrophobic surface has effect on the self-cleaning properties of the surface. Depending on the dynamic viscosity, η, and liquid-air surface tension, σ, of the liquid, the drop can follow different regimes. Viscous drops, $\eta > \sqrt{\sigma \rho l_c \alpha}$, where l_c is the capillary length and α the small inclination angle, follow the Mahadevan-Pomeau model [32], and exhibit a solid-like rotation. This regime lasts until surface tension no longer dominates the inertial forces, i.e. when the capillary number is above unity, $Ca > 1$.

For less viscous liquid drops, experiments have shown the initial descent to have

a constant acceleration, $v(t) \sim t \sin(\alpha)$, where α is the small incline of the surface [33], indicating a pure sliding motion. This regime persists until air drag and viscous friction between solid and liquid balances the gravitational pull, resulting in a back-bending drop [34]. Other applications of structured surfaces has been considered, e.g., Patankar [35] considers the use of patterned surfaces as a driving device for lab-on-a-chip systems. By oscillating an increasingly textured surface vertically, drop motion can be induced, a situation also studied elsewhere [36, 37]. The influence of gradients in the surface texture on a drop impacting the surface was considered by Reyssat *et al.* [38], where an asymmetric wetting was observed, explaining why vibrated drops move on structured surfaces with variable texture density.

As previously mentioned, the large slip and associated large velocities seen on hydrophobic surfaces occur when the drop resides on top of the created structures. Cassie [23] and Wenzel [21] gave the first descriptions of the apparent contact angle of a drop residing either suspended or submerged on a structured surface. The models describe the static droplet, and gives rise to an apparent contact angle. However, there are a range of stable contact angles, owing to the hysteretic nature of the problem [26]. Among others, Patankar [35] has made experimental efforts to characterise the hysteresis on different structured surfaces, determining that neither of the two first models fully explain the hysteresis effect. Furthermore, there is a challenge regarding the moving contact line. Pomeau [39] proposes the effect of evaporation/condensation near the moving contact line, which also is in experimental agreement. However, in order to have slip on a surface, the Navier-slip condition can be applied; this boundary condition removes the stress singularity arising at the triple point in the case of a no-slip condition [40, 41, 42]. A review on general slip conditions is given by Rothstein [43], in which it is concluded that for situations of greater length-scale than the microscopic level, the Navier slip-condition is well-suited. A recent study by Srinivasan et al. [30] on multi-scale structured spray-coated surfaces resulted in slip lengths on the scale of 100 μm, indicating that, for small-scale flows, the no-slip boundary condition should likely be replaced.

The FEM as a numerical framework has been used to study both statics and dynamics of drops. This numerical method is also denoted a sharp interface method, since the boundary separating different phases is well-defined. The static shape of a pendant drop hanging from a surface, and a static drop residing on a surface with a given static contact angle was examined by Saksono & Peric [5]. Their numerical solution matched well against a parameterization of the Young-Laplace equation. Dynamic effects, such as the evolution of the contact angle of droplets initially displaced [44] and oscillating droplets [45] have also been studied through FEM, and Brackbill et al. [46] and Walkley et al. [47] conclude that the method is in general suitable to describe free surface flows. Other numerical methods have been implemented, e.g. a Lattice-Boltzmann

model, which builds upon a diffuse interface, which does not explicitly solve the governing equations for the fluid flow [48]; e.g., simulations of a droplet climbing an inclined plane was done by Das & Das [49], where the gradients needed to sustain climbing at different inclination angles are examined.

Thampi et al. [50] recently applied a Lattice-Boltzmann model in order to study drops moving down an inclined plane. They specifically noted the remarkable dependence of the rotating motion in the drop on the parameter $q = \frac{4\pi \times Area}{Perimeter^2}$, a measure of how close to a circle the drop is. The closer q is to unity, the more rotation is observed inside the drop. They also noted the increasing rolling motion as the viscosity ratio between liquid and surrounding gas increases. Furthermore, they introduced a clever way to determine the amount of rotation inside the drop, based on a triple decomposition of the velocity gradient, enabling them to distinguish between the sliding, shearing and rolling motion of the drop. However, they did not compare to experimental results, but considered the steady state of the model and not the initial descent of the droplets, this being the scope of the present study. A similarity for all the mentioned numerical studies is the use of a 2-dimensional drop to study the dynamics and statics. As is the case in our study, it is believed, that the result is generalizable to the 3-dimensional case.

In the next sections, we focus on the initial steady accelerating descent of a droplet on an inclined plane, and on the oscillations of a droplet in a potential created from gradients in contact angle.

The numerical model and the numerical scheme used to obtain the simulations is presented, and we show how the slip coefficient can be used as a characterising parameter for a superhydrophobic surface, by comparing with experimental data found in the literature. We furthermore compare the results from the model with known rolling and sliding examples to highlight the rotating motion inside the drop, and also determine the energies related to translation and internal fluid flow. Using numerical tracer particles, interesting results for specific particle trajectories inside the drop are presented. In the contact angle potential, we show that the droplet responds nonlinear with respect to the applied strength of the potential, something which might be attributed to the internal oscillation frequency of the drop.

Geometry

The chosen geometry is shown schematically in Figure 5.1, where the computational domain is Ω, the free boundary is Γ_{free}, and the solid-liquid boundary is Γ_{solid}. The union of these two is the entire boundary, $\Gamma = \Gamma_{\text{free}} \bigcup \Gamma_{\text{solid}}$, and

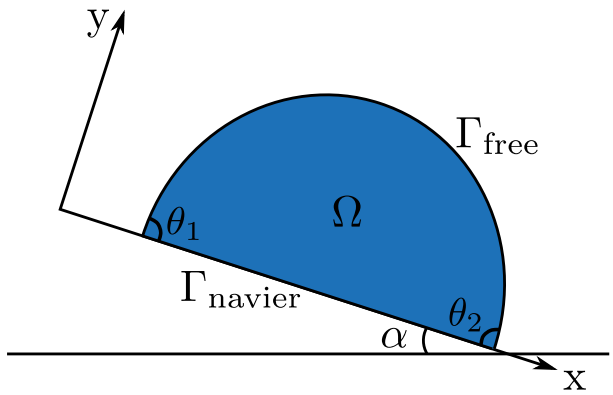

Figure 5.1: The drop on an inclined plane. The inclination angle is α. Ω is the computational domain, Γ_{free} and Γ_{solid} are the free and solid-liquid boundaries. The contact angles at left and right side are θ_1 and θ_2. All these quantities are allowed to vary in time. The diameter of the drop is $D = 2R_0$. We model gravity as a body force in the x-direction.

they have no overlap, $\Gamma_{\text{free}} \bigcap \Gamma_{\text{solid}} = \emptyset$. At each boundary, we assign a normal and tangent vector set, $(\mathbf{n}_F, \mathbf{t}_F)$ and $(\mathbf{n}_S, \mathbf{t}_S)$. The contact angles at the left and right side of the drop are denoted θ_1 and θ_2 respectively. Note that in general $\theta_1 \neq \theta_2$. The diameter of the drop is $D = 2R_0$. The domain and the boundaries are allowed to change with time as the system evolves. The chosen coordinate system allows for implementation of a spatially varying prescribed contact angle.

Governing equations

The extended model including the solid surface boundary, Γ_{solid}, is reflected in an additional term in Eq. (3.23),

$$\int_{\Gamma} \mathbf{v} \cdot (\mathbf{n} \cdot \mathbf{S})\, d\gamma \quad = \quad \int_{\Gamma_{\text{free}}} \mathbf{v} \cdot (\mathbf{n} \cdot \mathbf{S})\, d\gamma + \int_{\Gamma_{\text{solid}}} \mathbf{v} \cdot (\mathbf{n} \cdot \mathbf{S})\, d\gamma. \tag{5.1}$$

$$\tag{5.2}$$

Now, the first term on the right hand side has already been treated (Eq. (3.26)), but the contact line contribution has to be included in this model,

$$\int_{\Gamma_{\text{free}}} \sigma \mathbf{v} \cdot \partial_s \mathbf{t}_F ds = -\int_{\Gamma_{\text{free}}} \sigma \mathbf{t}_F \cdot \partial_s \mathbf{v} ds + \left[\sigma \mathbf{v} \cdot \mathbf{t}_F\right]_{\text{cl}}. \tag{5.3}$$

For the contact line term we decompose the test function,

$$\mathbf{v} = (\mathbf{v} \cdot \mathbf{n}_S)\mathbf{n}_S + (\mathbf{v} \cdot \mathbf{t}_S)\mathbf{t}_S, \tag{5.4}$$

where we note that the no-penetration boundary condition $\mathbf{v} \cdot \mathbf{n}_S = 0$ removes the first term. Inserting Eq. 5.4 into Eq. 5.3 we obtain

$$\begin{aligned} \int_{\Gamma_{\text{free}}} \sigma \mathbf{v} \cdot \partial_s \mathbf{t}_F ds &= -\int_{\Gamma_{\text{free}}} \sigma \mathbf{t}_F \cdot \partial_s \mathbf{v} ds \\ &+ \left[\sigma(\mathbf{v} \cdot \mathbf{t}_S)\,(\mathbf{t}_S \cdot \mathbf{t}_F)\right]_{\text{cl}}. \end{aligned} \tag{5.5}$$

For suitable choice of $[\mathbf{t}_F]_{\text{cl}}$ we get $\mathbf{t}_S \cdot [\mathbf{t}_F]_{\text{cl}} = \cos\theta$. The situation can be seen in Figure 5.2. Eq. (5.5) now becomes

$$\begin{aligned} \int_{\Gamma_{\text{free}}} \sigma \mathbf{v} \cdot \partial_s \mathbf{t}_F ds &= -\int_{\Gamma_{\text{free}}} \sigma \mathbf{t}_F \cdot \partial_s \mathbf{v} ds \\ &+ \sigma \cos\theta \left[(\mathbf{v} \cdot \mathbf{t}_S)\right]_{\text{cl}}. \end{aligned} \tag{5.6}$$

On the solid-liquid boundary, we use the Navier boundary condition stated in Eq. (4.11) and get

$$\int_{\Gamma_{\text{solid}}} \mathbf{v} \cdot (\mathbf{n} \cdot \mathbf{S})\, d\gamma = -\frac{1}{\hat{\epsilon}} \int_{\Gamma_{\text{solid}}} (\mathbf{v} \cdot \mathbf{t}_S)\,(\mathbf{u} \cdot \mathbf{t}_S)\, d\gamma. \tag{5.7}$$

One term remains, namely the inclusion of external forces. Gravity is written as $\mathbf{f}_g = g\mathbf{e}$, where $\mathbf{e}$ is a normal vector in the direction of gravity. This leads to a nondimensional weak term,

$$\int_{\Omega} \mathbf{f} \cdot \mathbf{v} \partial\Omega = \frac{1}{Fr} \int_{\Omega} \mathbf{e} \cdot \mathbf{v} \partial\Omega, \tag{5.8}$$

where Fr is the aforementioned Froude number.

This concludes the addition of the solid-liquid boundary, and in the next section we describe the numerics and mesh used.

Simulations and meshing

The model was implemented in the numerical framework of COMSOL v. 4.2 [51]. The geometry was created as described, and then meshed using the programs meshing tools; care was taken to set up an initial mesh that would resolve the boundaries adequately. Since the boundary and domain of the droplet is moving in time, the Arbitrary Lagragian-Eulerian method was used [12]. The mesh on the boundaries is displaced with the fluid, whereas inside the drop, it is smoothly

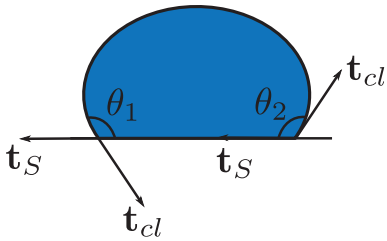

Figure 5.2: The left and right side of the drop and corresponding contact angles (θ_1 and θ_2 respectively), along with the solid tangents ($\mathbf{t}_s$) and contact line tangents ($\mathbf{t}_{\mathrm{cl}}$).

advected by solving a Winslow partial differential equation [52]. Remeshing of the domain was done when the quality of any mesh element would fall below a given threshold. The largest gradients in velocities was expected to be observed near the triple line, necessitating a finer mesh in these areas, see Figure 5.3.

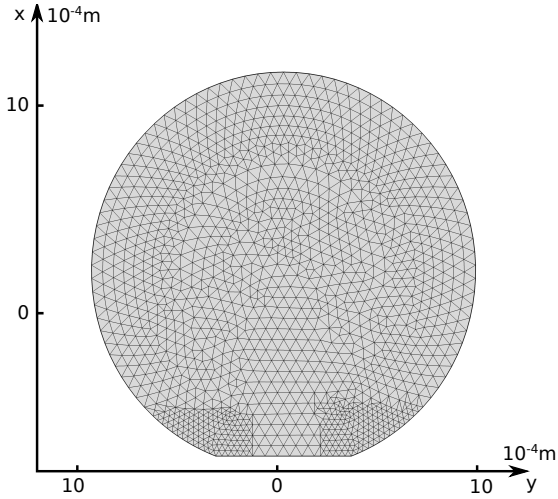

Figure 5.3: The initial mesh is shown for a drop with $\theta_1 = \theta_2 = 160°$. Notice the more finely resolved mesh structure near the contact line points.

To find the static shape of the drop on a hydrophobic surface we initially set $\alpha = 0$, and then let the drop evolve from a starting shape with $\theta_1 = \theta_2 = 90°$ to the new equilibrium shape. This configuration was then saved, remeshed and used as a starting point for the rest of the simulations. There were approximately

2300 mesh nodes, corresponding to roughly 6000 degrees of freedom.

5.2 The inclined plane

In the following section we present results relating to the motion of a droplet in the two situations mentioned at the beginning of the Chapter. We start by showing results relating to the shape of the droplet, and then continue with a description of the internal flow field and the oscillations in the x- and y-direction.

Drop shapes

In the case of $\alpha = 0$, the drop shape deforms solely due to gravity and surface tension. The Bond number, $Bo = \frac{\rho g R_0}{\sigma}$, is a measure of the relative influence of gravity compared to surface tension effects. Figure 5.4 shows the evolution of the drop shape with changing Bond number, and a fixed contact angle of 140°. For lower Bond numbers the drop shape becomes increasingly circular, due to decreased gravitational effects. A similar result would have been obtained, had the surface tension been increased accordingly.

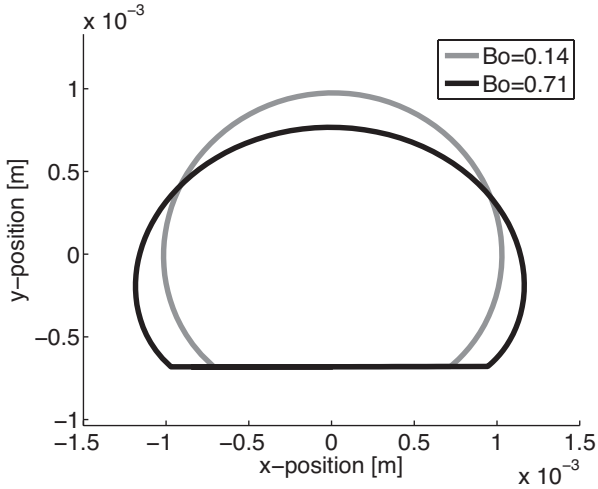

Figure 5.4: Static drop shapes for increasing Bond number and static contact angle of 140°.

When the inclination angle is different from 0, the drop moves down the surface, provided the gravitational pull surpasses the contact angle hysteresis force. Three drop shapes are shown in Figure 5.5 for moving droplets with a 10° hysteresis, and three different contact angles. The Figure depicts how the contact area with the surface decreases as the contact angle increases.

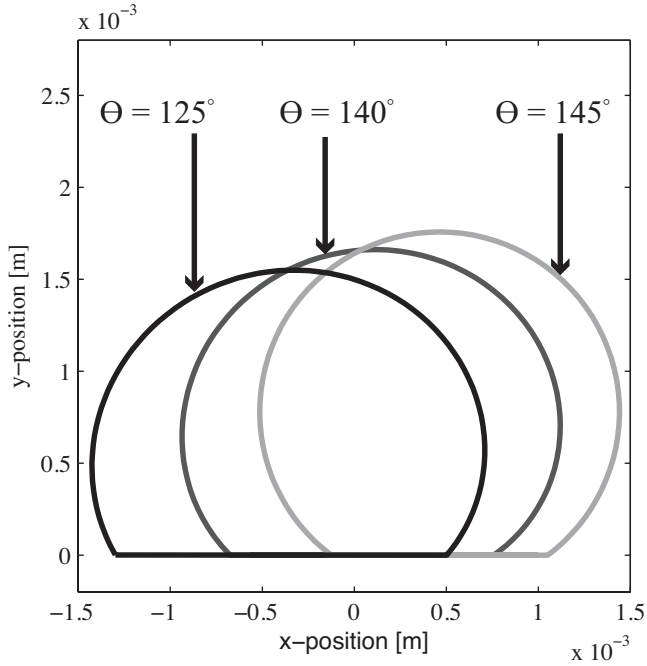

Figure 5.5: Drop shapes for moving droplets with contact angles of $\theta = 125°$, $\theta = 140°$ and $\theta = 145°$ with a 10° hysteresis. The coordinates have been translated to allow for comparison.

Sliding velocity as a function of slip parameter

We now focus on the dynamical effects of drops moving down an inclined plane. The influence of the slip parameter β, see eq. (4.11), on a droplet of radius $R_0 = 0.85$ mm residing on a surface inclined $\alpha = 1°$, with $\theta = 160°$ and hysteresis $\Delta\theta = 10°$ is shown in Figure 5.6. In the plot, five solutions are shown for β increasing in value from 10^{-6} m to 10^{-2} m. Also, data found in the literature with the same system parameters are shown. The effect of increasing the slip length saturates at some threshold, in practice resulting in an upper

bound on the acceleration of the droplet. Furthermore, for $\beta = 10^{-6}$ m and $\beta = 10^{-5}$ m, a steady state is reached, owing to a balancing of the gravitational pull with the hysteresis force and the viscous dissipation in the drop. For larger slip lengths, the steady state is not reached, but would have been, had longer simulation times been used. The experimental data is described to some extent by the model with $\beta = 10^{-3}$ m and $\beta = 10^{-2}$ m, with little difference between these two solutions.

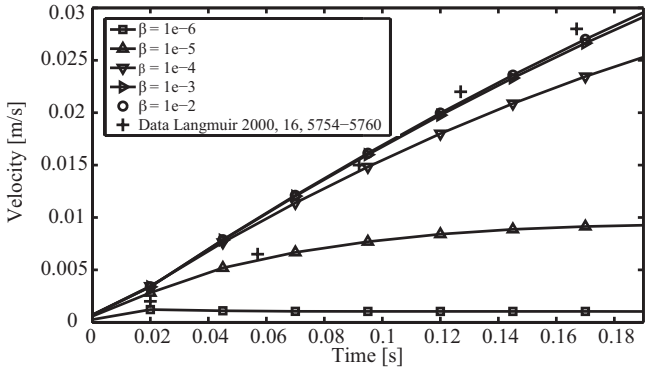

Figure 5.6: Velocity of a drop as a function of time for different values of β. $\alpha = 1°$, with $\theta = 160°$ and hysteresis $\Delta\theta = 10°$. Also plotted is data found in the literature for similar system parameters [31].

The Navier-slip condition employed at the solid-liquid interface effectively means that the drop is sliding down the surface with friction. However, this sliding motion gives rise to some rotation inside the drop, and we therefore expect a somewhat smaller velocity than for a purely sliding object. A comparison of the solution for $\beta = 10^{-3}$ m with four known purely rolling objects, and a purely sliding object, is seen in Figure 5.7. As expected, the solution for the droplet lies between the purely sliding object and the purely rolling objects. This clearly indicates that some rotation is going on inside the drop, dissipating energy and slowing down the descent of the drop. However, it should be noted that the descent is still remarkably close to a frictionless sliding motion on the surface, i.e. there is very little drag from the solid on the liquid drop.

Energy considerations

The total kinetic energy of the drop is given by

$$E_{\text{total}} = E_{CM} + E_R = \frac{1}{2} m v_{CM}^2 + E_R, \tag{5.9}$$

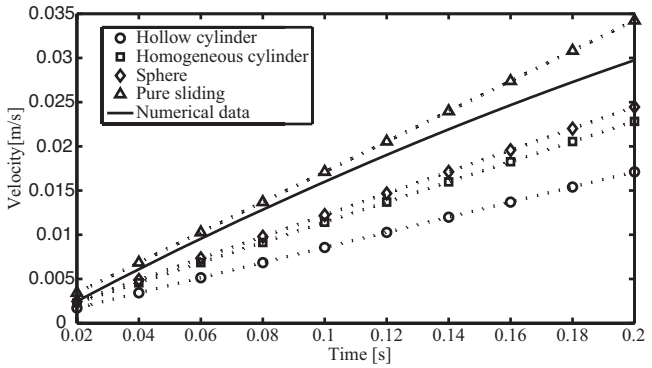

Figure 5.7: Velocity as a function of time for a purely sliding object, our numerical solution, and four purely rotating objects. In all cases, $\alpha = 1°$, and for the droplet, additionally $\theta = 160°$ and $\Delta\theta = 10°$.

where v_{CM} is the velocity of the centre of mass, and E_R is the residual energy of the drop, relating to the rotational energy, seen from the accelerated centre of mass coordinate system. We compute E_R as the difference between E_{total} and E_{CM}, since they can both be easily obtained by considering each element in the mesh and the average of all elements, respectively. Figure 5.8 shows the fraction $\frac{E_{CM}}{E_R}$ for three droplets with $\alpha = 1°$, $\theta = 140°, 145°, 150°$ and hysteresis $\Delta\theta = 10°$. For $t < 0.1$ s, the translational energy grows and becomes 40-50 times larger than the energy E_R of the internal flow. The unsteady motion observed for $t < 0.1$ s is due to surface waves; once these waves are damped sufficiently, the motion becomes steady. At later times, $t > 0.1$ s, a saturation is seen, and the amount of translation to internal flow energy becomes almost constant at a value of around 35.

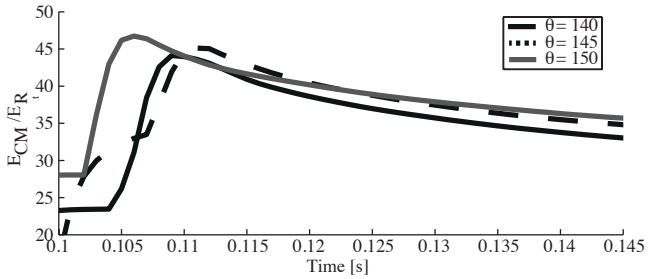

Figure 5.8: The fraction $\frac{E_{CM}}{E_R}$ as a function of time for $\alpha = 12°$, $\theta = 140°, 145°, 150°$ and hysteresis $\Delta\theta = 10°$. The graph shows the relative magnitude of the energy associated with translation and internal flow. The surface is tilted at $t = 0.1$ s.

To consider the effect of gravity on the droplet dynamics we show, in Figure 5.9, the fraction $\frac{E_{CM}}{E_R}$ for two different Bond numbers. For the higher Bond number, the droplet rotational energy is increased, which could possibly be due to a larger contact area with the surface.

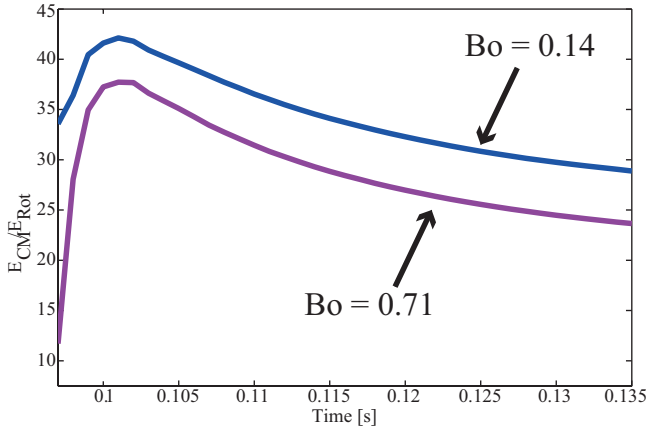

Figure 5.9: The fraction $\frac{E_{CM}}{E_R}$ as a function of time for increasing Bond number. The inclination is $\alpha = 1°$, the contact angle is 140° and the surface is tilted at $t = 0.1$ s.

Velocity field inside the drop

The internal flow in the drop is visualized in Figs. 5.10-5.12. In Figure 5.10 the drop is shown in the laboratory frame, whereas in Figs. 5.11 and 5.12, the drop is shown in the frame of reference moving with the centre of mass of the drop, which is in the x-direction (to the right). Figure 5.10 shows the drop at $t = 0.08$ s; the colour surface depicts the z-component of the vorticity (the only non-zero component). The figure indicates that essentially all fluid rotating motion is located below the centre of mass in the drop. Furthermore, the vorticity resembles the one obtained in previous studies [50]. Figs. 5.11 and 5.12 depict the evolution of the velocity field in the centre of mass frame as the average velocity increases from time $t = 0.045$ s to $t = 0.19$ s, respectively. Clearly, there is a rotating circulation inside the drop, however, the velocities associated with rotation vary substantially as a function of the position inside the drop. The normalized arrows indicate the direction of the flow, and the contour surface shows the magnitude of the velocity. We note that the point around which the flow rotates, shifts upwards and towards the trailing edge of the droplet as the average velocity increases. Through Particle Image Velocimetry measurements

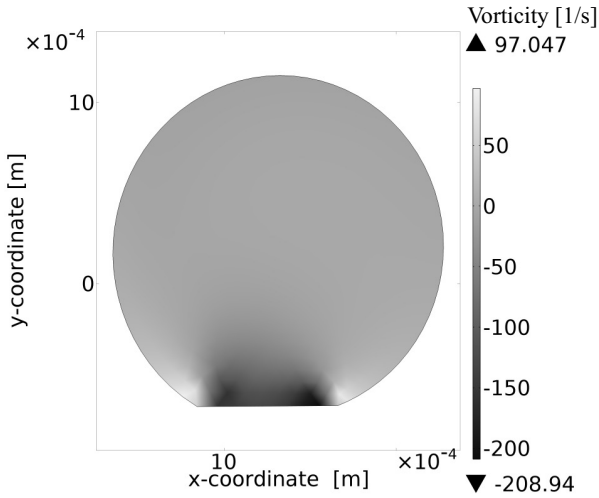

Figure 5.10: A drop with $\theta = 160°$, and $\Delta\theta = 10°$ on an incline of $\alpha = 1°$. The drop is depicted in the laboratory frame, and the colour code shows the z-component of the vorticity.

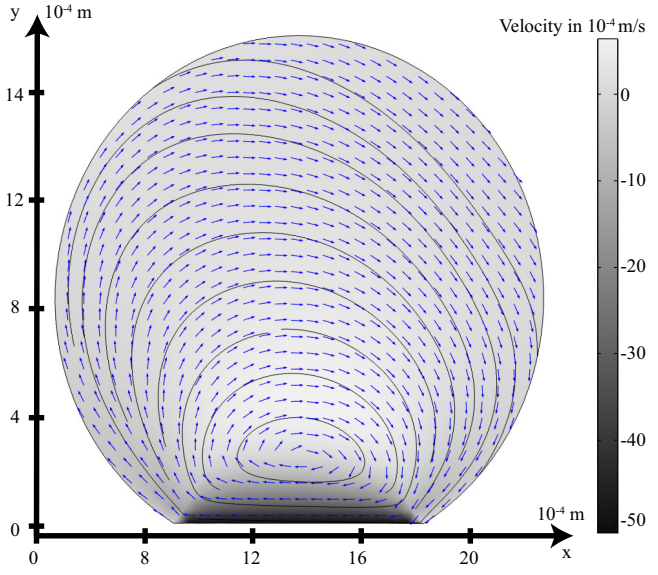

Figure 5.11: A drop with $\theta = 160°$, and $\Delta\theta = 10°$ on an incline of $\alpha = 1°$. The drop is depicted in the centre of mass frame of reference, moving to the right. The velocity field direction is indicated by normalised arrows and the streamlines and contour plot shows the size of the velocity. The simulation time is $t = 0.045$ s.

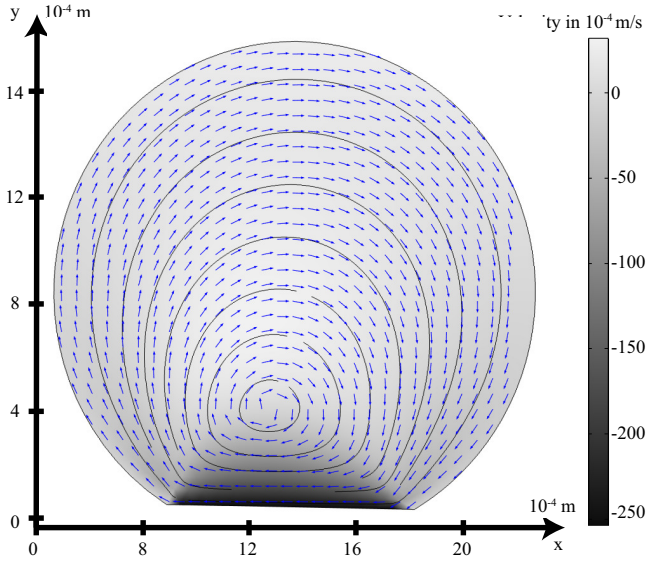

Figure 5.12: A drop with $\theta = 160°$, and $\Delta\theta = 10°$ on an incline of $\alpha = 1°$. The drop is depicted in the centre of mass frame of reference, moving to the right. The velocity field direction is indicated by normalised arrows and the streamlines and contour plot shows the size of the velocity. The simulation time is $t = 0.19$ s.

it is possible to experimentally track particles located inside drops. Figure 5.13 shows the trace of three particles located inside the numerically computed droplet. The small particles were advected with the fluid flow and assumed to have a very small density compared to the fluid density. When placed near the centre of the drop, the trajectory clearly reveals the circulatory motion in the droplet; however, when placed near the boundary, very small displacements are observed, owing to the weak internal flow observed here.

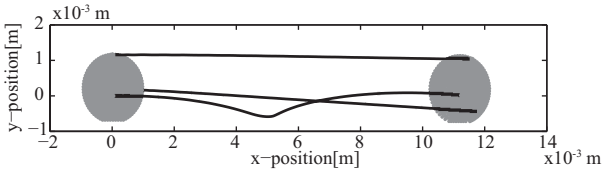

Figure 5.13: The evolution of three particles placed inside the drop and advected with the fluid velocity field. The drop evolves from left ($t = 0$ s) to right ($t = 0.6$ s).

5.3 The potential well

We have created a "potential well" from sharp gradients in the contact angle. The idea is to put a less hydrophobic stripe on a hydrophobic surface. In Figure 5.14 a schematic of the spatially varying contact angle is shown. The potential is modelled as

$$\mathrm{Pot}_\theta = \theta_0 + \frac{\Delta\Psi}{2}\left[2 - \tanh\left(\frac{x - x_L}{\epsilon}\right) + \tanh\left(\frac{x + x_R}{\epsilon}\right)\right], \tag{5.10}$$

where θ_0 is the angle inside the potential, $\Delta\Psi$ is the difference in contact angle, x_L and x_R is the left and right boundary of the potential, and ϵ is the characteristic distance over which the potential varies. By initially placing a drop asymmetrically in the potential one expects the drop to oscillate back and forth in the potential until all energy has been dissipated due to viscous friction. In the following we have fixed $\theta_0 = 2$ (115°), and only varied the strength of the potential, $\Delta\Psi$.

Figure 5.15 shows the horizontal velocity of the centre of mass as a function of time for four different potentials. All oscillations follow the same behaviour: after some transient period they decay until finally being damped out. It is seen that, even though the potential is stronger for $\Delta\Psi = 0.7$ rad (40°), the amplitude and decay length is significantly larger for $\Delta\Psi = 0.6$ rad (34°). To

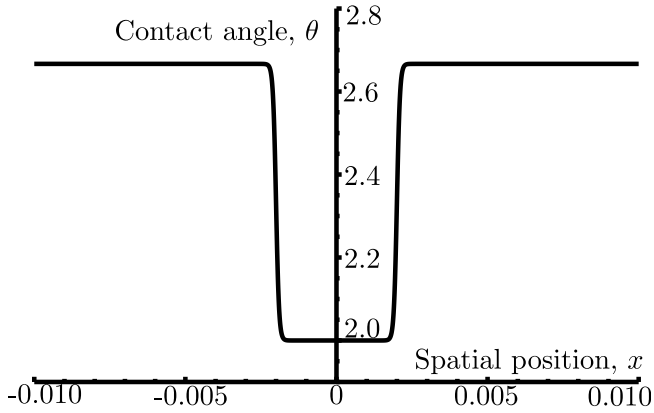

Figure 5.14: An example of the potential well with $\theta_0 = 2$ rad (115°), $\Delta\Psi = 2/3$ rad (38°), $x_L = x_r = 10^{-3}$, $\epsilon = 10^{-4}$.

get a clearer image of the relation between the oscillations and the forcing, we have plotted the peaks of the oscillations for each potential in Figure 5.16. We have considered nine different potentials in order to see how they relate. The figure shows that the three weakest potentials are almost identical and at the same time standing out from the remaining six. It is also seen that a potential with $\Delta\Psi = 0.6$ rad (34°) has the same characteristics as a potential with $\Delta\Psi = 0.75$ rad (43°), and similarly for $\Delta\Psi = 0.5$ rad (29°) and $\Delta\Psi = 0.7$ rad (40°). It is not surprising that the drop responds in a nonlinear way since the dynamics inside the droplet also influence the motion. We attribute the strong response to the internal oscillation frequency of the drop, something also discussed previously.

The oscillations of the drop is not only horizontal, Figure 5.17 shows the trajectory of the center of mass of the drop as it oscillates in the potential. The variation in both x- and y-axis is on the order of 10^{-3}m. The figure shows how the center of mass oscillates in both directions until finally stopping at an equilibrium point. It should be noted that the figure shown is for a surface with a contact angle of 161° contact angle; for smaller angles, the variation in the y-direction becomes smaller. The oscillatory frequency in the y-direction is higher than in the x-direction, and one could expect some none trivial coupling between the oscillations in the two principal directions.

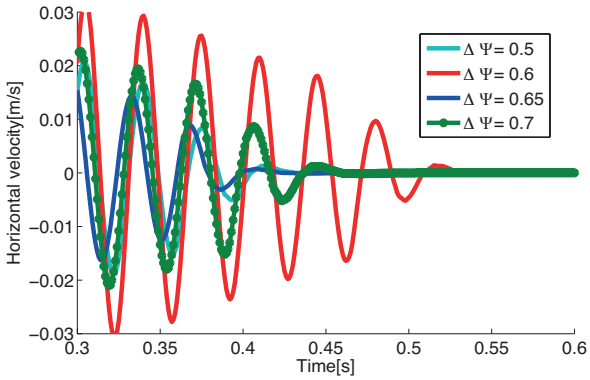

Figure 5.15: The horizontal velocity as a function of time. Shown for four different potentials.

5.4 Conclusion and Discussion

In the first part of this thesis We have set up a two dimensional Finite Element Method numerical model which is able to calculate the flow inside a droplet deposited on a hydrophobic surface. The full Navier-Stokes equation was solved inside the droplet domain, whereas on the free boundary, the Young-Laplace equation was used. We used a slip condition on the solid-liquid boundary, and argued that this was reasonable when describing the macroscopic motion of the droplet. The presented results regarding the droplet on the inclined plane agreed to some extent with present literature, even though the numerical method used here is significantly different.

The developed model has both advantages and disadvantages. Starting with the former, it is noted that the numerical framework is applicable for all types of surfaces, including those which are hydrophilic. Furthermore, a large range of drop sizes can be used, limited only by the computational power available. This is possible since gravity is included in the model, and the drop deforms with Bo, which was shown in Figure 5.4. In general, the framework is quite robust and the need for re-meshing of the domain is minimal, due to the ALE formulation. Another advantage of the model is the possibility to give an expression for the contact angle, e.g. enabling spatial variations in the contact angle or using a velocity dependent formulation of the contact angle [53].

One of the significant simplifications of the model is the reduction of the dynamics to two dimensions. During the studies, a three dimensional model was under development, and the formulation closely resembles the two dimensional

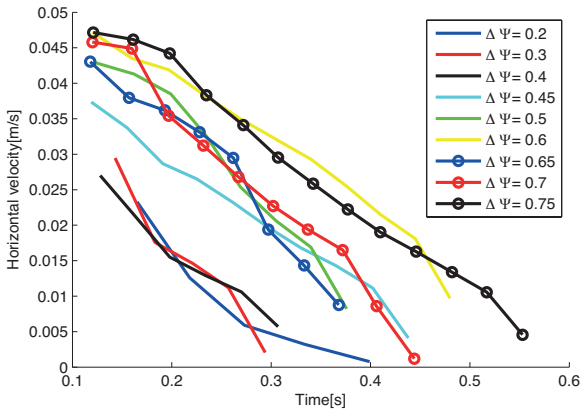

Figure 5.16: The peaks of the oscillations as a function of time. Still shown for different contact angle gradients.

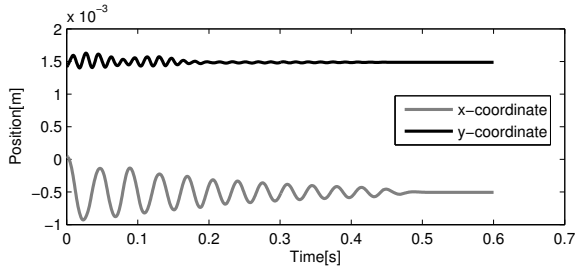

Figure 5.17: Oscillations in the x- and y-direction for $\theta_0 = 2$ (115°), $\Delta\Psi = 0.8$ (46°). The damping in the two directions is not of equal magnitude.

one. However, the computational complexity increases when adding a dimension, and the result was a model that never converged. It should be mentioned that, to our knowledge, all numerical models considering drop-solid interactions are two dimensional.

The drag from the liquid surrounding the drop is not taken into account, and this gives a limit of validity on the velocity of the droplet. The maximum Reynolds numbers in the simulations of the drop on the inclined plane is $Re_{\max} \approx 30$. A rough comparison can be made between our model and a Stokes flow, for which an approximate formula for the Stokes drag can be obtained [54, 55]. The drag

becomes important when it surpasses the gravitational forces, i.e.

$$Bo \ll \frac{9}{2}\frac{\eta_a}{\sqrt{\sigma\rho R_0}}\max|u(t)|\left(1+\frac{1}{12}Re_{\max}\right), \tag{5.11}$$

where η_a is the dynamic viscosity of the surrounding liquid. Putting in characteristic numbers, we see that this inequality is satisfied for the velocities observed in the simulations (up to 0.05 m/s). Of course, the model is more complex than the flow around a spherical drop, since interactions near the contact line which are complicated may arise. However, the above serves to somewhat justify not modeling the surrounding liquid.

Finally, the smoothing assumption at the solid-liquid boundary is a subject for discussion. Evidently, the model does not take into account the micro- and nanoscale features of a given surface, and We argued why this was not possible when seeking to describe the macroscopic behavior of the drop. Implementing the Navier slip condition adds a free parameter to the model, allowing an adjustment to experimental data. Although an effective slip length has been observed, it is important to remember that this does not mean there is an actual slip condition at the microscopic scale. When introducing the slip parameter, it should be seen as a compromise between wanting to describe the macroscopic flow while still capturing the essential parts at the microscopic level. Whether this has been achieved is hard to tell, but the results of the internal flow patterns in our model are comparable to lattice-Boltzmann simulations where microscopic structures are included.

Part II

Droplets bouncing on a vibrating surface

The second part of this thesis deals with droplets bouncing on a vertically vibrated fluid bath, first considered by Walker [56] in 1978 and recently by Couder and coworkers [57]. This system is interesting since it comprises the first known example of a macroscopic particle-wave duality with pilot-wave mechanics. Such a system naturally gives rise to interesting discussions of philosophical nature [58], especially since deBroglie postulated elementary particles to be governed by their own pilot wave [59]. However, in the following we undertake a physical and mathematical investigation of the system, and it turns out that the bouncing drops comprise a dynamical system in the mathematical sense with a very rich behavior.

We begin with an introductory chapter, covering the experimental set-up of the system and the mathematical model governing the droplet's vertical and horizontal motion. Then follows two in-depth studies. The first is an experimental characterization of the vertical bouncing modes of the droplets, which is supplemented by theoretical predictions. The results of this chapter has been published in Physics of Fluids [60]. The second study concerns the situation where the fluid bath is also rotated about a vertical axis. We present an extensive numerical study of the phase transitions (presented in a regime diagram) and analyze the different classes of orbits and compare with experimental results. A manuscript based on the findings in this chapter is currently under preparation, to be written in collaboration with Anand U. Oza, Daniel M. Harris, Ruben Rosales and John W. M. Bush.

Chapter 6

Introduction

6.1 The experiment

Consider a fluid of density ρ, kinematic viscosity ν and surface tension σ in a horizontal bath of depth H and diameter D, driven by a vertical vibration of amplitude A and frequency $f = \omega/(2\pi)$ (see Figure 6.1). The effective gravity in the vibrating bath frame of reference is

$$g^*(t) = g + \gamma \sin(2\pi f t), \tag{6.1}$$

where g is the gravitational acceleration, and $\gamma = A\omega^2$ is the forcing acceleration. At low forcing acceleration, the fluid remains quiescent (perfectly flat) in the vibrating frame; however, above a critical acceleration amplitude γ_F corresponding to the Faraday threshold, the layer becomes unstable to a field of standing Faraday waves. If the fluid is regarded as ideal (no resistance to shear stresses), it is possible to apply the perturbative method also used in Chapter 2 to the oscillating fluid bath. The result is a parametric instability of the fluid surface, where the amplitude of the waves are governed by Mathieu's equation [61]. In the parameter region of interest, the waves are subharmonic, with half the frequency of the vibrational forcing, $\omega_F = \omega/2$. Their wavelength $\lambda_F = 2\pi/k_F$ is prescribed by the standard surface wave dispersion relation [62, 63]:

$$\omega_F^2 = \left(gk_F + \frac{\sigma k_F^3}{\rho}\right) \tanh(k_F H). \tag{6.2}$$

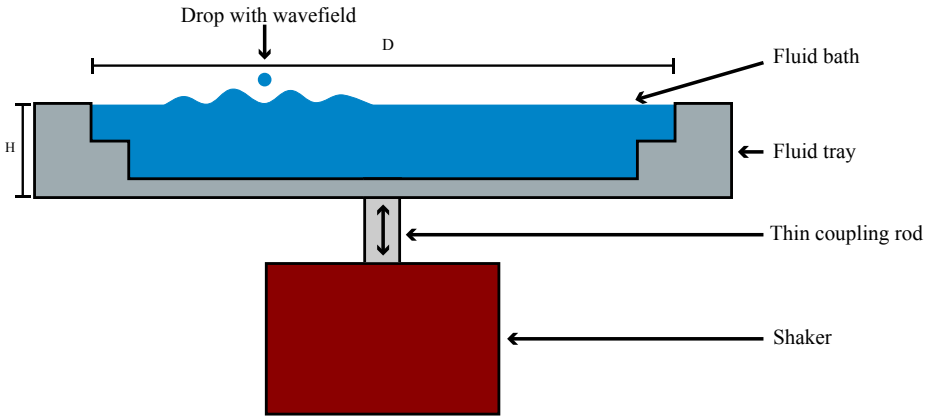

Figure 6.1: The experimental setup consists of a fluid tray mounted on top of an industrial shaker, vibrating the tray vertically.

It is important to note that in the experiments of interest, the vibrational forcing is less than the Faraday threshold, $\gamma < \gamma_F$, and consequently, the interface would remain flat if not for the presence of a droplet.

When a fluid drop of unperturbed radius R_0 is placed on a vibrating bath (see Figure 6.2), there are essentially three outcomes: either the droplet may coalesce, bounce in place or walk across the fluid surface. This was first characterized by Couder's group, [64, 65]. For $\gamma < \gamma_B$, where γ_B is the bouncing threshold, the applied forcing is insufficient to levitate the drop, resulting in coalescence with the bath, since the intervening air layer thins until reaching a critical thickness at which Van der Waals forces between drop and bath initiate coalescence. For $\gamma > \gamma_B$, this air layer is sustained during impact due to the layer being squeezed and thus drained slowly, enabling a stable bouncing state. Walker [66] first reported the stabilization of bouncing drops on a vertically vibrated soap solution. Beyond a critical forcing threshold, $\gamma > \gamma_w$, where γ_w is the walking threshold, the stationary bouncing state is destabilized by the underlying wave field, giving rise to a dynamic state in which the drops walk across the fluid bath. The walking regime arises only for a limited range of drop sizes and forcing conditions, and a drop in this configuration is called a walker.

In the experiment, the drops are created by extracting a submerged needle from the fluid bath. This technique can create drops of different radii, depending on the angle and thickness of the needle along with the speed of retraction. Typical drop sizes range from 0.20 mm to 1.00 mm, depending on the viscosity of the oil.

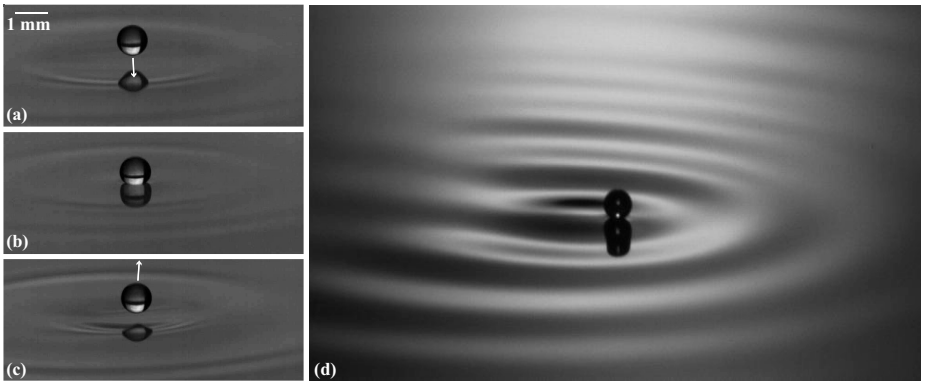

Figure 6.2: A walking drop of diameter 0.48 mm on a vibrating bath of 20 cS silicone oil vibrating at 70 Hz, (a) before, (b) during and (c) after impacting the surface. The arrows indicate the direction of motion. (d) A walking drop and its associated wave field. From [60]

A schematic illustration of the experimental setup is shown in Figure 6.1. A circular tray with $D = 76$ mm and $H = 16$ mm is vertically vibrated with a sinusoidal amplitude A and frequency f. The peak acceleration is $\gamma = (2\pi f)^2 A$. The dimensionless quantity $\Gamma = \gamma/g$, is from now on used as the forcing parameter for the system. Similarly we define the dimensionless Faraday threshold as $\Gamma_F = \gamma_F/g$.

If multiple drops are created on the surface, and $\gamma_B < \gamma < \gamma_w$, they will produce structures that are related to the Archimedean tilings of the plane [67, 68]. The system comprising the many droplets is an example of a self-organizing system, where the wave field of the individual drop interacts with the surrounding drops.

Since the bath is vibrating at the frequency $\omega_{\text{bath}} = 2\pi f$, and the drop has an internal oscillation on the order of (recall Eq. (2.34)),

$$\omega_{\text{drop}} = \sqrt{\frac{\sigma}{R_0^3 \rho}}, \tag{6.3}$$

a natural dimensionless parameter is the ratio of these two frequencies,

$$\Omega = \frac{\omega_{\text{bath}}}{\omega_{\text{drop}}} = 2\pi f \sqrt{\frac{R_0^3 \rho}{\sigma}}. \tag{6.4}$$

This parameter is the vibration number, and is a proxy for drop size [55] since, in the experiments, the frequency is fixed. The vibration number is thus a function of the radius of the drop, $\Omega = \Omega(R_0^{3/2})$.

The drop itself acts as a local perturbation of the surface and gives rise to a standing field of Faraday waves, centered at the point of impact [64]. The temporal decay of this wave field is determined by the distance of the forcing to the Faraday threshold, and one measure of this distance is the fraction γ/γ_F. The closer the forcing is to the Faraday threshold, the less the waves are damped. Another measure is also useful, namely the memory parameter

$$M_e(\gamma) = \frac{T_d}{T_F(1-\gamma/\gamma_F)}, \tag{6.5}$$

where T_D is the viscous decay time of the waves without forcing [65], and $T_F = 2/f$ is the period of the Faraday waves. This quantity increases as the Faraday threshold is approached from below and appears in the formula for the wave created at drop impact. We will, however, primarily use the fraction γ/γ_F as an indication of the memory in the system when discussing results.

6.2 Mathematical model

The mathematical description of the system comes in three parts which deals with the vertical dynamics, the wave field created when the drop impacts the bath, and the horizontal dynamics. A thorough derivation of these three parts is not the scope of this chapter, and instead the reader is referred to the papers referenced below. However, in the following, an overview of the equations describing a bouncing droplet is given.

The vertical dynamics is described by an ordinary differential equation, modeling the interaction between fluid bath and drop as a logarithmic spring. The first iteration of the model was based on investigations of drops bouncing on soap films [69, 70, 71], and here the drop-bath interaction was considered linear. Subsequently, drops impacting a rigid surface was considered [72], until the model in its present form was obtained by considering drops bouncing on a vibrated fluid surface, also taking into account the nonlinear relation in the drop-bath interaction [55]. This nonlinearity was observed by considering the dependence of the normal coefficient of restitution, $C_R^N = \frac{V_{\text{in}}}{V_{\text{out}}}$, and the contact time between bath and drop, T_C, on the Weber number $We = \rho R_0 V_{\text{in}}^2/\sigma$. Here V_{in} and V_{out} is the speed of the droplet immediately before and after impacting the surface. The model has been derived asuming $We \ll 1$, which indicates that the inertial forces are small compared to surface tension forces, and means that the impact dynamics is slow compared to the surface wave dynamics. The model is based on a quasi-static approach in which the instantaneous shape of drop and bath are approximated by quasi-static shapes characterized by few parameters (the drop is expanded as a sum of spherical harmonics, similar to

the calculations in Chapter 2). Calculating the Lagrangian of the system and using the Euler-Lagrange equation yields an ordinary differential equation for the vertical motion of the droplet,

$$-mg^*(t) = m\ddot{z} \quad \text{in free flight } ((z-h) \geq 0 \text{ or } F_N \leq 0)\ , \tag{6.6}$$

$$-mg^*(t) = \left(1 + \frac{c_3}{\ln^2 |\frac{c_1 R_0}{z-h}|}\right) m\ddot{z} + \frac{4}{3}\frac{\pi\mu R_0 c_2(\nu)}{\ln |\frac{c_1 R_0}{z-h}|}(\dot{z}-\dot{h}) + \frac{2\pi\sigma(z-h)}{\ln |\frac{c_1 R_0}{z-h}|} \quad \text{during contact.} \tag{6.7}$$

Here z is the drop center of mass and $z-h$ is the height of the drop above the bath surface. The drop experiences a reaction force which depends on the relative position of the height of the drop and bath, $z-h$, and further, there is a drag force depending on the relative speed of the drop and bath $\dot{z}-\dot{h}$. The droplets inertia is corrected by its internal flow, this is the first term on the right hand side. During impact

$$F_N(t) = m\ddot{z} + mg^*(t), \tag{6.8}$$

is the normal component of the reaction force acting on the drop. The effective gravity in the bath frame of reference is $g^*(t)$, and during free flight only gravity is assumed to act on the drop, and viscous dissipation is assumed to dampen the droplet oscillations sufficiently so that the drop is nearly spherical when impacting the fluid bath. This assumption is important, and it is possible to calculate the drop sizes for which it holds. For $\nu = 50$ cS oil, the drop radius has to be $R_0 < 8$ mm, and for $\nu = 20$ cS oil, $R_0 < 1.3$ mm [55]. In the experiments, these conditions are met. The parameters c_1, c_2, and c_3 are obtained by fitting the model to either the normal coefficient of restitution, C_R^N, and the contact time T_C of the drop, or some of the well-known phase transitions in the regime diagram. The values are $c_1 = 2$, $c_3 = 1.4$, $c_2 = 12.5$ for 20 cS oil and $c_2 = 7.5$ for 50 cS oil. The logarithmic nonlinearity in the drop-bath is reflected in the term $\ln |\frac{c_1 R_0}{Z}|$, which becomes increasingly linear with c_1.

Evidently, the bath height h is not perfectly flat, and could potentially influence the dynamics. We will assume the entire surface height to be a superposition of the waves created by the drop at each impact [65],

$$h(\mathbf{x}, t) = \sum_{n=1}^{N} h_n(\mathbf{x}, t). \tag{6.9}$$

Molacek & Bush [73] showed that a drop impacting the surface at $(\mathbf{x}_n, t_n)$ creates approximately a standing wave prescribed by a zeroth order Bessel function of the first kind decaying exponentially in time. Here, we use their approximation

in the long-time evolution of a fully analytical model, also developed in [73]. For a drop impacting at $(\mathbf{x}_n, t_n)$, the created wave is then

$$h_n(\mathbf{x}, t) \approx AJ_0\left(k_F(\mathbf{x} - \mathbf{x}_n)\right) \mathrm{e}^{-\frac{(t_n - t)}{T_F M_e}}, \tag{6.10}$$

where

$$A = \sqrt{\frac{2}{\pi}} \frac{k_F R_0}{3k_F^2 R_0^2 + Bo} \frac{R_0 k_F^2 \sqrt{\mu_{eff}}}{\sigma} \frac{\cos(\pi f t)}{\sqrt{t - t_n}} \int F_N(t') \sin\left(\pi f t'\right) \mathrm{d}t'. \tag{6.11}$$

Here $Bo = \rho g R_0^2/\sigma$ is the Bond number, T_d is the characteristic decay time of the unforced waves, which depends on the fluid viscosity and the Faraday wavenumber. The effective or phenomenological viscosity, μ_{eff}, is required to ensure that the decay rate of the approximation matches that in the fully analytical model (see [73], Appendix A.1). The integral of the reaction force, $F_N(t)$ is carried out over the duration of contact. We see that the waves are damped exponentially in time, and the memory parameter M_e determines the strength of the damping.

The horizontal dynamics of a bouncing droplet can be obtained by assuming the drop to be in resonance with the bath, i.e. it is in the period-doubled region bouncing periodically in the vertical direction with period $T = \frac{4\pi}{\omega}$. In the following, we let $\overline{f(t)}$ denote the time-average over one period T of the function f. By balancing horizontal forces on the drop, we get [73, 74]

$$m\ddot{\mathbf{x}} + D\dot{\mathbf{x}} = -\overline{F(t)\nabla h(\mathbf{x}, t)}, \tag{6.12}$$

where

$$D = 0.17\frac{\sqrt{\rho R_0}}{\sigma} mg + 6\pi R_0 \mu_a \left(1 + \frac{gR_0}{12}\nu_a f\right), \tag{6.13}$$

is the total instantaneous drag coefficient. The subscript a denotes air. The first term represents the momentum drag induced during impact, the second term the aerodynamic drag induced during flight [73]. In Eq. (6.12), $F(t)$ is the vertical force coefficient on the drop, and the entire right hand side corresponds to the propulsive force the drop experiences when it impacts the possibly sloped interface of the fluid bath. All terms are time-averaged over the bouncing-period T.

We want to obtain expressions for the right hand side of Eq. (6.12). The fluid bath height, Eq. (6.10), for a single impact at $(\mathbf{x}_n, t_n)$ in the time-averaged periodically bouncing case reduces to a slightly simpler expression,

$$h_n(\mathbf{x}, t) = AJ_0\left(k_F\left|\mathbf{x} - \mathbf{x}_n\right|\right) \mathrm{e}^{-\frac{(t - t_n)}{T_F M_e}}. \tag{6.14}$$

Here

$$A = \sqrt{\frac{2}{\pi}} \frac{\kappa_F^3 R_0^2 \sqrt{\mu_{eff}}}{3\kappa_F^2 R_0^2 + Bo} \frac{mg\sqrt{T_F}}{\sigma} \sin\frac{\phi}{2} \cos\frac{\phi}{2},$$

where ϕ is the mean phase of the wave during the contact time between drop and bath. This quantity depends, in general on viscosity, drop size and forcing in the system Eq. (6.14) essentially strobes out the vertical dynamics by considering time-averages over one bouncing period. The total fluid height is then obtained by summing over all impacts, i.e.,

$$h(\mathbf{x}, t) = \sum_{n=-\infty}^{t/T_F} A J_0\left(k_F \left|\mathbf{x} - \mathbf{x}_n\right|\right) \mathrm{e}^{\frac{-(t-nT_F)}{T_F M_e}}. \tag{6.15}$$

Following Oza *et al.* [75], the sum is transformed to an integral, which is a valid approximation as long as the timescale of the vertical dynamics, T_F, is much smaller than the timescale of the horizontal dynamics, T_H. This essentially means that the horizontal dynamics has to be much slower than the vertical. Assuming the drop is in a period doubled vertical bouncing mode (in Chapter 7 we show that this is a good assumption), the vertical bouncing period is $T_V \approx \frac{1}{f} = 0.0125$ s, and a drop travels roughly 4 mm during a period. This gives a velocity of 320 mm/s. In comparison, the highest observed velocities in the horizontal direction is on the order of 10 mm/s, so the approximation is valid. Another simplification in the stroboscopic approach is the replacement of $\frac{1}{\sqrt{t-t_n}}$ in Eq. (6.10) with $\frac{1}{\sqrt{T_F}}$, which is done since the exponential term $\mathrm{e}^{\frac{-(t-nT_F)}{T_F M_e}}$ dominates the long-time behavior. The sum is finally approximated as

$$h(\mathbf{x}, t) = \frac{A}{T_F} \int_{-\infty}^{t} J_0\left(k_F \left|\mathbf{x} - \mathbf{x}_n(s)\right|\right) \mathrm{e}^{-(t-s)/(T_F M_e)} ds. \tag{6.16}$$

We are now ready to find a final expression for the term $-\overline{F(t)\nabla h(\mathbf{x}, t)}$ in Eq. (6.12). The time-average of the vertical force is mg since the vertical bouncing is assumed periodic, i.e. $\overline{F(t)} = mg$. Taking the gradient of the fluid bath interface, Eq. (6.16), and using that $\frac{dJ_0(z)}{dz} = -J_1(z)$, yields the complete integro-differential equation governing the horizontal dynamics of the droplet,

$$m\ddot{\mathbf{x}} + D\dot{\mathbf{x}} = \frac{F}{T_F} \int_{-\infty}^{t} \frac{J_1\left(k_F \left|\mathbf{x}(t) - \mathbf{x}_n(s)\right|\right)}{\left|\mathbf{x}(t) - \mathbf{x}_n(s)\right|} \left(\mathbf{x}(t) - \mathbf{x}_n(s)\right) \mathrm{e}^{-(t-s)/(T_F M_e)} ds, \tag{6.17}$$

where $F = mgAk_F$. This equation is in practice complicated to solve because of the dependence on the previous solutions, represented in the integral. One could also call Eq. (6.17) a delay differential equation, with an infinite delay time. Through stability analysis of Eq. (6.17), it is possible to show that a droplet

walking in a straight line, is stable to perturbations in the line of direction, and neutrally stable to perturbations perpendicular to the line of direction [74].

In the next Chapter we present an experimental characterization of the vertical bouncing mode of the drops, as a function of the system parameters.

Chapter 7

Experimental mode characterization

The first characterization of the droplet behavior was done by Couder's group. They investigated the behavior in terms of the drop diameter $d = 2R_0$ and dimensionless forcing acceleration $\Gamma = \gamma/g$ [64, 76, 65]. Protiere *et al.* [64] conducted experiments with a viscosity-frequency combination of 50 cS-50 Hz and summarized their results in a regime diagram illustrating the droplet behavior in the d-Γ plane. For low forcing accelerations, simple bouncing arises, where the drop hits the bath once every driving period. Increasing the acceleration generally leads to a period-doubled bouncing state, where the drop hits the bath once every two driving periods. For relatively small and large drops, a period doubling cascade may follow, culminating in chaotic bouncing or walking. For the larger drops, an intermittent regime can arise in which the drop changes from one bouncing state to another in a possible aperiodic way. These structures are well-known in dynamical systems theory, and arise in many physical systems [77]. We will return to the dynamical systems description of the bouncing drops when considering a rotating and vibrating fluid tray in chapter 8.

For drops within a limited size range, there is a critical $\Gamma_w = \gamma_w/g$ above which they walk along the surface of the bath. The walking region has previously been thought to solely consist of a period doubled bouncing. However, the model developed in [55, 73] predicts that other vertical bouncing modes may

be found inside the region. In the following, the results of an experimental study of the vertical modes of bouncing and walking drops is presented. In section 7.2, a selection of the obtained modes are presented and a specific mode, the mixed state, is highlighted. The results are collected in three regime diagrams showing the phase transitions in the system, which are then discussed and related to theoretical predictions. My contribution is the experimental characterization and input as to which theoretical regime diagrams to compute.

7.1 Experimental set-up

In Figure 7.1 a schematic illustration of the experimental set-up is presented. A circular fluid tray of diameter 76 mm and depth 16 mm is excited vertically in a sinusoidal manner with frequency f and amplitude A. The tray is mounted with a square air bearing carriage, to minimize lateral vibrations. The slider bar of the air bearing is connected through a thin coupling rod to an industrial shaker, which is mounted on a leveling platform. A power amplifier controlled by a data acquisition system through custom software drives the shaker. To ensure a correct forcing is supplied, two piezoelectric accelerometers are mounted on the fluid tray. They serve as input to a feedback loop which maintains the desired vibration amplitude, giving a tolerance of 0.01 g in the vibrational acceleration amplitude.

Oil drops are created by rapidly extracting a submerged needle from the fluid bulk. Of the droplets formed, we select those of radius R_0 between 0.20 mm to 0.51 mm. The undeformed drop radius R_0 is measured optically with a high-speed camera, recording at 4000 frames per second. The optical set-up results in a pixel density of $71 - 88$ pixels per mm, leading to an uncertainty in drop radius of $\pm 1.5\%$. The horizontal motion of the drop is captured from above with a Machine Vision CCD camera and is tracked using particle-tracking software.

Measurements for a single drop size was performed by either increasing or decreasing the driving acceleration in a stepwise manner from some initial value of Γ, with typical step size $d\Gamma = 0.1\Gamma$. The entire bouncing and walking region could then be explored by varying γ between γ_B and γ_F.

The mode with which a drop bounces is noted by $(m, n)^i$, where the integer superscript i increases with the state's mean mechanical energy, specifically, the drop's combined kinetic and gravitational potential energy. A typical spatio-temporal diagram of a droplet is shown in Figure 7.2, the mode shown is (2,1). The temporal part comprises 255 ms, and the spatial part is 4 mm. The arrows indicate the drop position as the upper white curve, and its reflection in the

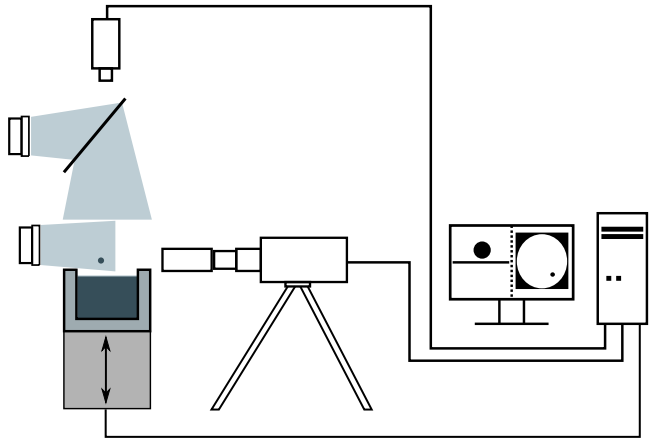

Figure 7.1: Schematic illustration of the experimental set-up. The vibrating bath is illuminated by two LED lamps, and the drop motion recorded by two digital video cameras. The top view camera captures images at 17.5–20 frames per second, while the side view camera records at 4000 frames per second. The video processing is done on a computer. From [60]

bath as the lower gray curve which is surrounded by black curves. Also marked is an example of a drop impact on the bath and the positions where the bath reaches its maximums height. The quantities m and n, i.e. the number of bath oscillations and drop bounces, respectively, are also shown. The ratio m/f represents the period of the bouncing mode, during which the drop contacts the surface n times.

The spatio-temporal diagrams are obtained by considering each frame in a video sequence of the vertical bouncing mode of the drop. An example of such a frame is shown in Figure 7.3. The drop position and its reflection in the bath is determined, and all frames are then successively stacked.

We decided to consider three different combinations of oil viscosity and forcing frequency, namely 20 cS-80 Hz, 50 cS-50 Hz and 20 cS-70 Hz. The oil with kinematic viscosity $\nu = 20$ cS has density $\rho = 949$ kg/m^3 and surface tension $\sigma = 20.6$ mN/m, and the oil with $\nu = 50$ cS has $\rho = 965$ kg/m^3 and $\sigma = 20.8$ mN/m. The Faraday threshold γ_F is the found for each combination of experimental parameter by increasing the forcing amplitude γ until standing waves spontaneously form at the surface.

Since the 20 cS-80 Hz combination exhibited the theoretically richest behavior

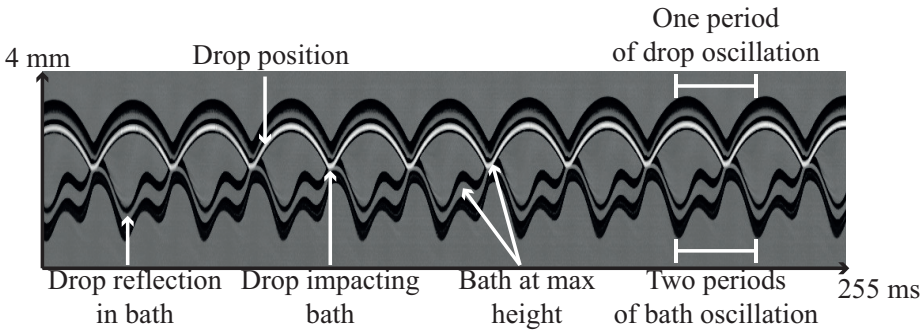

Figure 7.2: Spatio-temporal diagram of a (2,1) mode with interpretative arrows showing the drop reflection in the bath, the drop position, the drop impacting the bath, the math positions of max height of the bath, and finally the periods of the drop and bath oscillations, respectively.

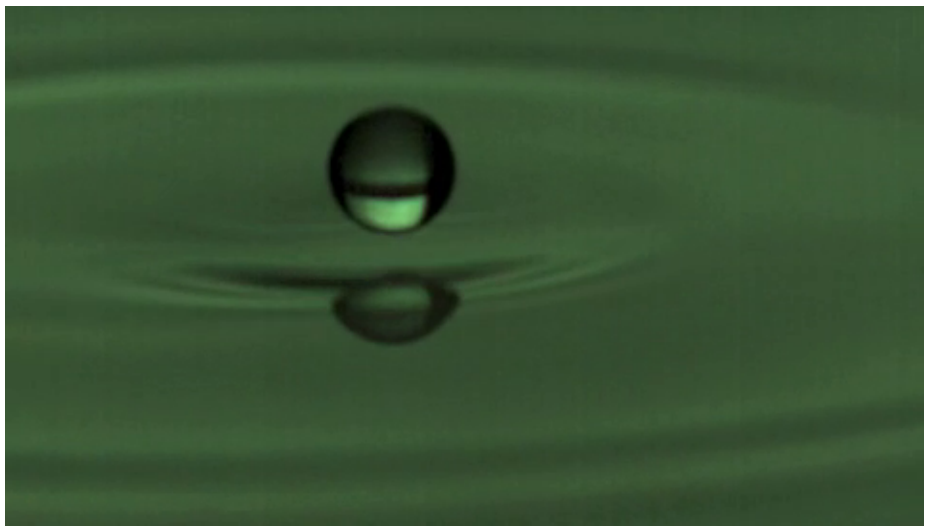

Figure 7.3: A snapshot of a video sequence capturing the bouncing mode of a droplet of radius $R_0 = 0.72$ mm.

Viscosity-Frequency	Regime diagram	Bouncing and walking modes
20 cS-80 Hz	Figure 7.4(a)	$(2,1)^1$, $(2,1)^2$, (2,2), **(4,2)**, **(4,3)**, **(4,4)**, chaotic. Figure 7.5
50 cS-50 Hz	Figure 7.4(b)	$(\mathbf{2},\mathbf{1})^{\mathbf{1}}$, $(\mathbf{2},\mathbf{1})^{\mathbf{2}}$, **chaotic**. Figure 7.6
20 cS-70 Hz	Figure 7.4(c)	**(2,2)**, (4,3), **(13,10)**, $(2,1)^1$, $(2,1)^2$, **mixed mode**, chaotic. Figure 7.7

Table 7.1: The walking and bouncing modes observed for the three viscosity-frequency combinations examined. Modes in bold typeface are those for which an associated spatio-temporal diagram is included (see Figs. 7.5-7.7)

in both bouncing an walking region, a full investigation in both regions was made. For the other two combinations, the walking region was characterized. Figure 7.4 presents the droplet behavior in the Γ-Ω for all three combinations. Accompanying the regime diagram is spatio-temporal diagrams showing selected vertical bouncing modes. Spatiotemporal diagrams of selected bouncing and walking modes are presented in Figures 7.5-7.7. For quick reference and overview of the observed bouncing modes, see Table 7.1.

7.2 Results

In the three regime diagrams reported in Figure 7.4, the horizontal axis is the dimensionless forcing $\Gamma = \gamma/g$, and the vertical axis is the dimensionless vibration number Ω. Individual markers correspond to experimental observations, with square and round markers denoting stationary bouncing and walking states, respectively. The color of the marker denotes the observed bouncing or walking mode. We first describe the experimental results, and then compare with theoretical predictions. References to spatiotemporal diagrams for specific modes are given when presenting the regime diagrams.

20cS -80 Hz

Figure 7.4(a) shows the regime diagram for the 20 cS-80 Hz combination. This is the most detailed exploration of the entire walking and bouncing regime we produced.

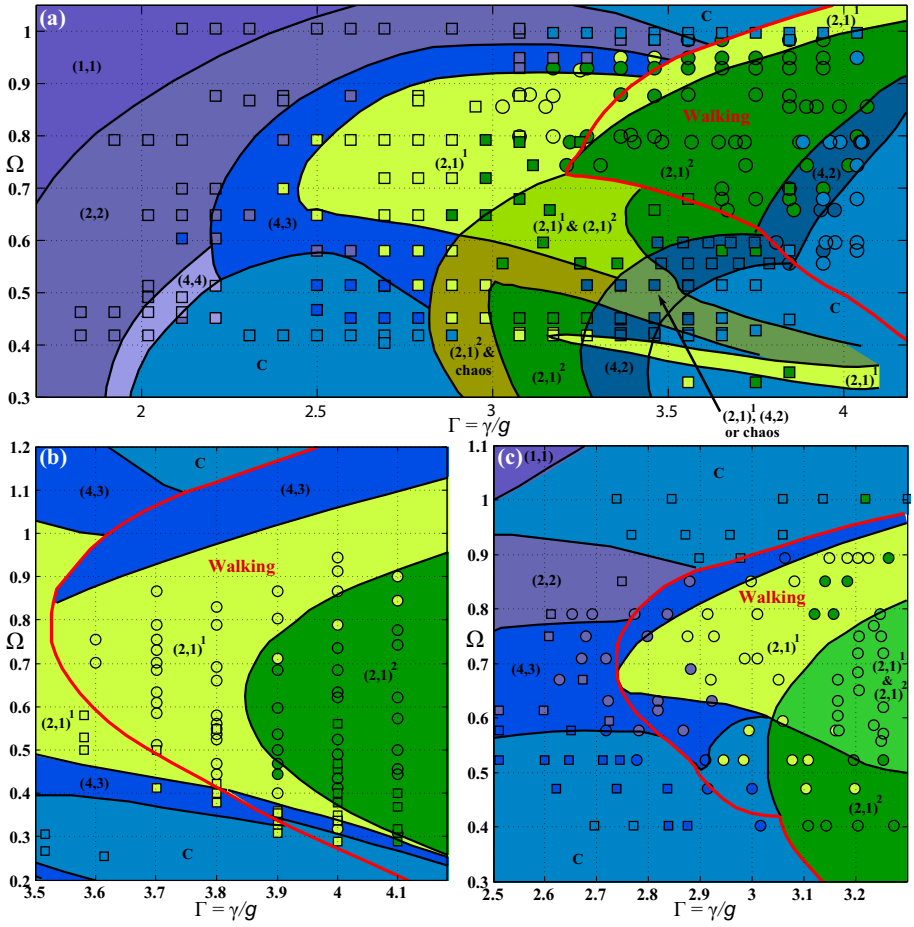

Figure 7.4: Regime diagrams indicating the dependence of the droplet behaviour on the dimensionless driving acceleration, $\Gamma = \gamma/g$, and the vibration number, $\Omega = 2\pi f\sqrt{\rho R_0^3/\sigma}$. (a) The 20 cS-80 Hz combination, for which $\Gamma_F = 4.22 \pm 0.05$. (b) The 50 cS-50 Hz combination, for which $\Gamma_F = 4.23 \pm 0.05$. (c) The 20 cS-70 Hz combination, for which $\Gamma_F = 3.33 \pm 0.05$. Coloured areas correspond to theoretical predictions, the solid red line denoting the theoretically predicted walking threshold. Experimental data is presented as square or round markers, with square markers denoting stationary bouncing states, round markers walking states, and their color indicating the associated mode. From [60]

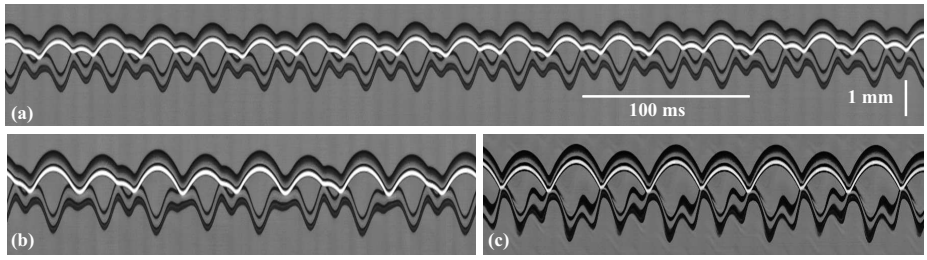

Figure 7.5: Spatiotemporal diagrams of the bouncing modes observed for the 20 cS-80 Hz combination. (a) Bouncing mode (4,4). $\Gamma = 2.3$, $\Omega = 0.45$. (b) Bouncing mode (4,3). $\Gamma = 2.7$, $\Omega = 0.45$. (c) Bouncing mode (4,2). $\Gamma = 3.5$, $\Omega = 0.42$. From [60]

Starting at lower forcing values, $1.5 < \Gamma < 2.3$, the $(2, 2)$ bouncing mode is dominant, but a small region of the $(4, 4)$ mode (Figure 7.5(a)) is observed for vibration numbers $\Omega \lesssim 0.5$. In this regime diagram, several $m = 4$ modes are observed as Γ is increased. In a region around $\Gamma \approx 2.6$ and $\Omega \approx 0.5$, the $(4, 3)$ mode (Figure 7.5(b)) arises. The $(4, 2)$ mode (Figure 7.5(c)) appears for almost all vibration numbers investigated, for $\Gamma > 3.3$, spanning both the bouncing and walking regimes.

The period doubled $(2, 1)$ bouncing modes extends from $\Gamma = 2.5$ up to Γ_F for vibration numbers between 0.6 and 1. Outside the walking region the drops are found in the low energy mode, $(2, 1)^1$, and then transitions into the high energy $(2, 1)^2$ mode as Γ is increased across the walking threshold. The $(2, 1)$ bouncing states also arise for smaller drops, $\Omega \approx 0.4 - 0.5$, along a band with Γ ranging from 2.9 to 3.3, at which a period doubling transition creates a (4,2) mode that eventually gives way to a chaotic region.

We observed three separate regions of either complex or chaotic motion. One exists in a region with $2.3 < \Gamma < 3$ and $\Omega \approx 0.4$. Drops bounce chaotic or complex in the region near $3.5 < \Gamma < \Gamma_F$, $0.4 < \Omega < 0.8$ spanning both the bouncing and walking regions. For larger drops ($\Omega \approx 1$) there is a region stretching from the bouncing ($\Gamma \approx 3.1$) into the walking regime, and up to the Faraday threshold. Generally, near the Faraday threshold, we observe the bouncing mode to be chaotic, with only a relatively small window of periodic bouncing, for $0.8 < \Omega < 1$, above which chaotic bouncing is observed. For $\Omega \approx 1$, stationary chaotic bouncing drops were observed that, when perturbed with a submerged needle, could be induced to transition into a stable $(2, 1)$ walking mode.

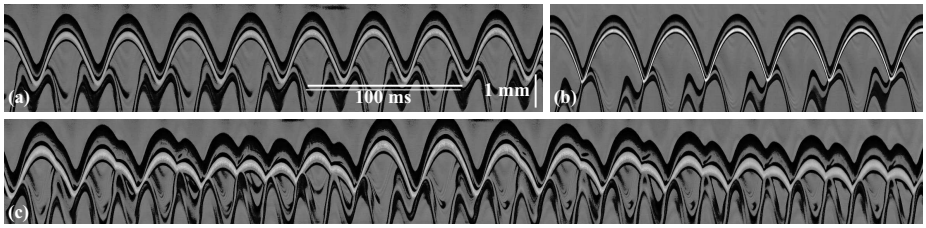

Figure 7.6: Spatiotemporal of the modes observed for the 50 cS-50 Hz combination. (a) Walking mode $(2,1)^1$. $\Gamma = 3.7$, $\Omega = 0.59$. (b) Walking mode $(2,1)^2$. $\Gamma = 4.0$, $\Omega = 0.44$. (c) Chaotic bouncing with no apparent periodicity. $\Gamma = 4$, $\Omega = 0.94$. From [60]

50 cS -50 Hz

For the 50 cS-50 Hz combination shown in Figure 7.4(b), we basically observed $(2,1)^1$, $(2,1)^2$, and chaotic bouncing, which all are presented in Figure 7.6. The observed walking modes were the $(2,1)^1$ and $(2,1)^2$ modes, where there was a noticeably difference in horizontal drop speed being, varying with a factor of roughly 4, with the higher velocity in the $(2,1)^1$ mode. The $(2,1)^1$ mode (Figure 7.6(a)) has a longer contact time with the liquid bath than the higher energy $(2,1)^2$ mode (Figure 7.6(b)), for which a much more rapid shift in momentum occurs during impact. The phase of impact relative to the bath is also different. The drop is generally in the $(2,1)^1$ mode near the walking threshold, but transitions to the $(2,1)^2$ mode as Γ is increased, remaining in this state until the Faraday threshold is reached. Chaotic bouncing is observed for lower forcing and drop size (Figure 7.6(c)).

20 cS -70 Hz

Some more exotic bouncing modes were observed for the 20 cS-70 Hz combination (Figure 7.4(c)). For drops bouncing in place, three bouncing modes are observed. For large ($\Omega \approx 1$) and small ($\Omega \approx 0.4$) vibration numbers, chaotic or highly complex bouncing states are evident. The spatiotemporal evolution of a complex $(13,10)$ mode is shown in Figure 7.7(a). Intermediate vibration numbers gives rise to (4,3) and (2,2) bouncing modes, with the former being observed for drops with $\Omega \approx 0.4 - 0.6$, and the latter for $\Omega \approx 0.6 - 0.8$. Figure 7.7(b) shows the spatio-temporal diagram of a drop in the (2,2) mode. Such a drop is referred to as a limping drop, due to the unequal step sizes. The (4,3) and (2,2) modes stretch into the walking region, where the $(2,1)$ modes are dominant. Once again, the $(2,1)^2$ mode is generally observed at lower Ω than

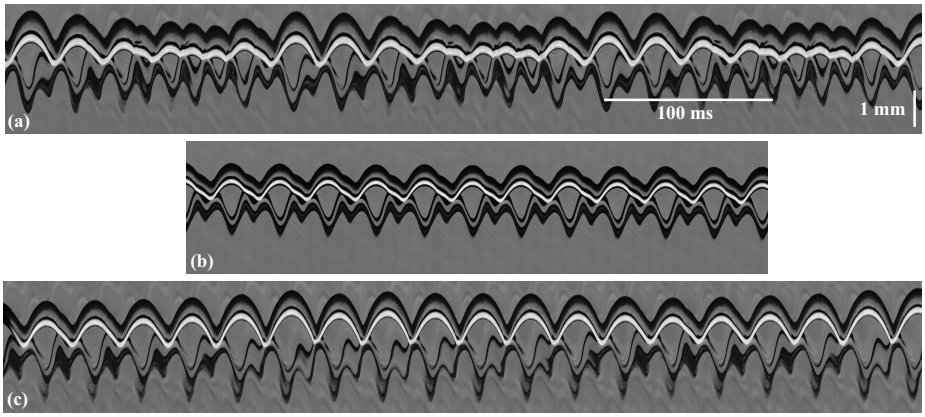

Figure 7.7: Spatiotemporal diagrams of the modes observed for the 20 cS-70 Hz combination. (a) The exotic bouncing mode (13,10), highly complex periodic motion. $\Gamma = 3.3$, $\Omega = 0.97$. (b) The limping drop, a (2,2) walking mode. $\Gamma = 2$, $\Omega = 0.42$. (c) The mixed walking state, shown here evolving from $(2,1)^1 \rightarrow (2,1)^2 \rightarrow (2,1)^1 \rightarrow (2,1)^2$. $\Gamma = 3.4$, $\Omega = 0.72$. From [60]

the $(2,1)^1$ mode.

Inside the walking regime (for $\Gamma > 3.1$ and $0.55 < \Omega < 0.8$) we observed a particular interesting bouncing state. Here the drop alternates between the two period doubled $(2,1)$ modes, as shown in Figure 7.7(c). In the figure, the drop is shown evolving from $(2,1)^1$ to $(2,1)^2$ to $(2,1)^1$ to $(2,1)^2$. Evidently, the height of the jumps are nearly equal, but the phase of impact shifts rapidly over a period of roughly 10 jumps. A horizontal trajectory of the drop in the mixed state is shown in Figure 7.8(a). The shading of the trajectory reflects its local horizontal speed which fluctuates by a factor of 4 as it switches between the fast $(2,1)^1$ mode and the slow $(2,1)^2$ mode. Figure 7.8(b) shows the velocity of the mixed mode as a function of arc-length. The variation of the velocity occurs over a distance of approximately one Faraday wavelength, resulting in the highly peaked power spectrum shown in Figure 7.8(c). Although the mixed state is in general robust, it can be destabilized. Interactions with the boundary of the experimental setup, or with a submerged needle may cause the drop to shift into either $(2,1)^1$ or $(2,1)^2$, depending on the magnitude of the perturbation. A situation where the drop interacts with the boundary is presented in Figure 7.8(d), which shows a color coded trajectory of a mode switcher shifting into the high energy $(2,1)^2$ mode after being perturbed by an approach to the boundary at nearly normal incidence. We note that we might alternatively have denoted the mixed state by a purely periodic mode, (24,12); however, we find it useful to

distinguish between the two phases of its motion ($(2,1)^1$ and $(2,1)^2$), in which its speed is markedly different.

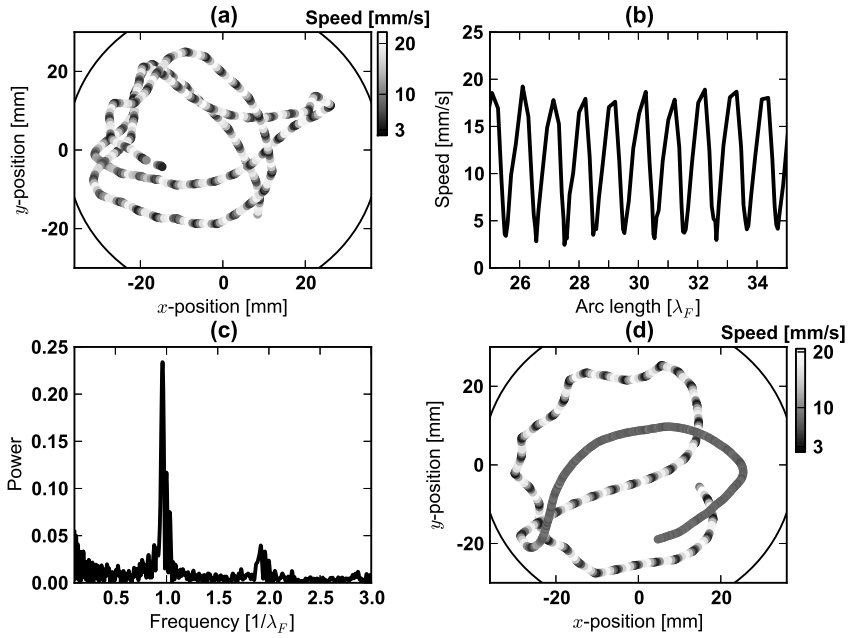

Figure 7.8: Mixed state walkers observed with the 20 cS-70 Hz combination. $\Gamma = 3.4$, $\Omega = 0.72$. (a) The trajectory for a drop in the mixed state, shaded according to the speed. The circular bath domain is indicated. (b) The observed variation of walking speed with arc-length, as normalised by the Faraday wavelength. (c) A Fourier power spectrum of the normalised velocity fluctuations, which indicates that the mode-switching arises periodically, after the droplet has walked a distance of approximately $0.95\lambda_F$. (d) Trajectory of a mixed mode, shaded according to speed, that destabilises into a $(2,1)^2$ walker after collision with the boundary near $(x, y) = (-25, -20)$ mm.From [60]

Chapter 8

Vibrating and rotating fluid tray

In this chapter the results of a combined numerical and experimental study of droplets bouncing on a vibrated and rotated fluid bath will be presented. This set-up was first considered experimentally by Fort *et al.* [78], and subsequently by Oza *et al.* [75] who also did numerical simulations. My contribution in the following lies in the numerical investigation, and the experiments has been performed by Dan Harris at MIT.

Consider Figure 8.1 where a schematic of the experimental set-up is presented. The fluid tray is vibrated vertically as before, and is also set in rotation around the center line of the bath, with rotation rate $\mathbf{\Omega_R} = \Omega_R \hat{\mathbf{z}}$.

The numerical description of the system starts with the previously described trajectory equation, Eq. (6.17). In the following, we denote the drop position in the bath frame of reference, seen from above and centered at the bath center line, by $\mathbf{x} = (x, y)$. Due to the rotation of the bath, the fluid interface is parabolic with the height being prescribed by [75]

$$h_0(\mathbf{x}) = H + \frac{\Omega_R^2}{2g} |\mathbf{x}|^2 - \frac{\Omega_R D^2}{16g}, \tag{8.1}$$

where H is the bath height with no rotation and D is the bath diameter. Since

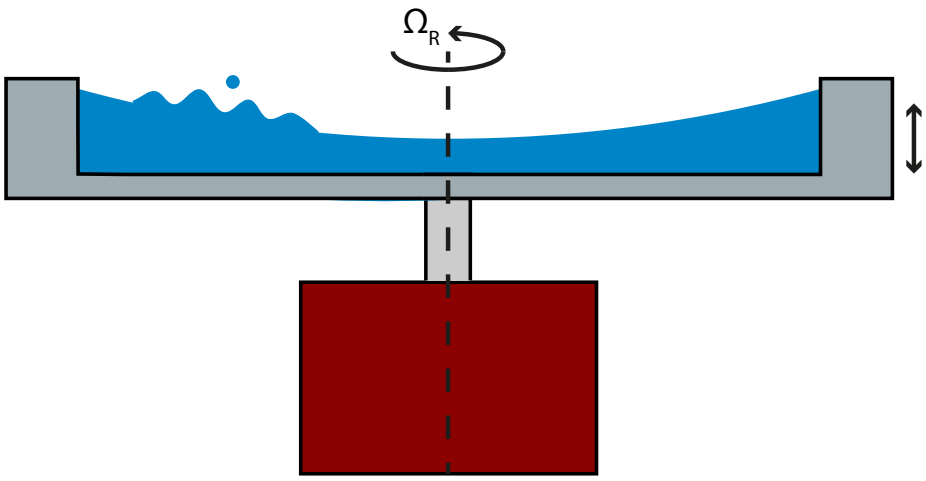

Figure 8.1: The experimental set-up. The fluid bath is vibrated vertically and rotated around an vertical axis at the center of the bath. The rotation rate about the centerline is denoted $\mathbf{\Omega_R} = \Omega_R \hat{\mathbf{z}}$.

the frame is rotating, the drop experiences a fictional Coriolis force,

$$\mathbf{F_{co}} = -2m\mathbf{\Omega_R} \times \dot{\mathbf{x}} = (2m\Omega_R y, -2m\Omega_R x, 0)\,, \tag{8.2}$$

and also a fictitious centrifugal force

$$\mathbf{F_{ce}} = -m\mathbf{\Omega_R} \times (\mathbf{\Omega_R} \times \mathbf{x}) = \left(m\Omega_R^2 x, m\Omega_R^2 y, 0\right). \tag{8.3}$$

Furthermore, there is an time-averaged propulsive force on the drop due to the parabolic fluid surface,

$$\mathbf{F_p} = \overline{F(t)\nabla h_0\left(\mathbf{x}\right)}, \tag{8.4}$$

where $F(t)$ is the instantaneous vertical forcing on the drop. Since the drop is assumed to bounce periodically in the vertical direction, $\overline{F(t)} = mg$ [73]. If we assume that the total fluid interface height can be written as a superposition of the parabolic shape and the standing wave field, $\nabla h_0\left(\mathbf{x}\right)$ is easily calculated, and we obtain for the propulsive force

$$\mathbf{F_p} = m\mathbf{x}\Omega_R^2. \tag{8.5}$$

This force cancels the centrifugal force, Eq. (8.3), and the resulting trajectory equation becomes

$$\begin{aligned} m\ddot{\mathbf{x}} + D\dot{\mathbf{x}} \quad = \quad & \frac{F}{T_F}\int_{-\infty}^{t} \frac{J_1\left(k_F\left|\mathbf{x}(t)-\mathbf{x}(s)\right|\right)}{\left|\mathbf{x}(t)-\mathbf{x}(s)\right|}\left(\mathbf{x}(t)-\mathbf{x}(s)\right)\mathrm{e}^{-(t-s)/(T_f M_e)}ds \\ & -2m\Omega_R \times \dot{\mathbf{x}}, \end{aligned} \tag{8.6}$$

which basically is Eq. (6.17) with an added Coriolis force term. We nondimensionalize the system by scaling length as $\hat{x} = k_F x$, and time as $\hat{t} = \frac{t}{T_F M_e}$, resulting in the dimensionless system of equations (without hats for clarity),

$$\kappa\ddot{\mathbf{x}} + \dot{\mathbf{x}} = \beta \int_{-\infty}^{t} \frac{J_1\left(|\mathbf{x}(t) - \mathbf{x}(s)|\right)}{|\mathbf{x}(t) - \mathbf{x}(s)|} \left(\mathbf{x}(t) - \mathbf{x}(s)\right) \mathrm{e}^{-(t-s)} ds - \Omega_R \times \dot{\mathbf{x}}. \tag{8.7}$$

Here, $\kappa = \frac{m}{DT_F M_e}$, and $\beta = \frac{Fk_F T_F M_e^2}{D}$, where the parameters F, D, T_d, and γ_F are determined from [73].

As stated previously, Eq. (8.7) is a delay-differential equation, which can only be considered analytically through certain assumptions. In the current set-up one could expect there to be periodic solutions for some parameter values, and in these regions Floquet theory could be useful [77]. However, the more interesting solutions turns out to be aperiodic, so we must use a more brute-force method to investigate the system. One approach is to assume a solution in the form of a circular orbit, i.e.

$$(x(t), y(t)) = (r_0 \cos(\omega t), r_0 \sin(\omega t)), \tag{8.8}$$

where r_0 is the orbital radius, and ω is the orbital frequency of the drop. Assuming the solutions to be circular orbits seems like a reasonable assumption in a system with a Coriolis force. In order to make a classification of the behavior of the system, we need to determine which parameters to use. In the previous Chapter, we considered the drop size (through the vibration number Ω) and the forcing. We will again use the forcing, and a second parameter to use could be the rotation rate of the fluid bath. This would allow for comparison of results with experiments, since the rotation rate is controllable in the experimental set-up. In the classical situation of a hockey puck sliding on a frictionless parabolic surface, there is a one-to-one correspondence between the rotation rate of the surface and the radius of the resulting circular orbit of the puck (in the rotating frame of reference). However, in the case of our system, it turns out that multiple radiis exist for the same rotation rate [79]. If we use the circular orbit assumption, Eq. (8.8), in Eq. (8.7), a set of algebraic equations is obtained,

$$-\kappa r_0 \omega^2 = \beta \int_0^\infty J_1\left(2r_0 \sin\frac{\omega z}{2}\right) \sin\frac{\omega z}{2} \mathrm{e}^{-z} dz + \Omega_R r_0 \omega \tag{8.9}$$

$$r_0 \omega = \beta \int_0^\infty J_1\left(2r_0 \sin\frac{\omega z}{2}\right) \cos\frac{\omega z}{2} \mathrm{e}^{-z} dz. \tag{8.10}$$

We now have a definition between r_0 and Ω_R, given some value of M_e. In Figure 8.2, the nondimensional radius has been plotted as a function of nondimensional rotation rate for four different memories. We observe that at low memory, (a), there is an almost classical relation between r_0 and Ω, but as γ is increased in panels (b)-(d), inflection and turning points develop. The result is that multiple

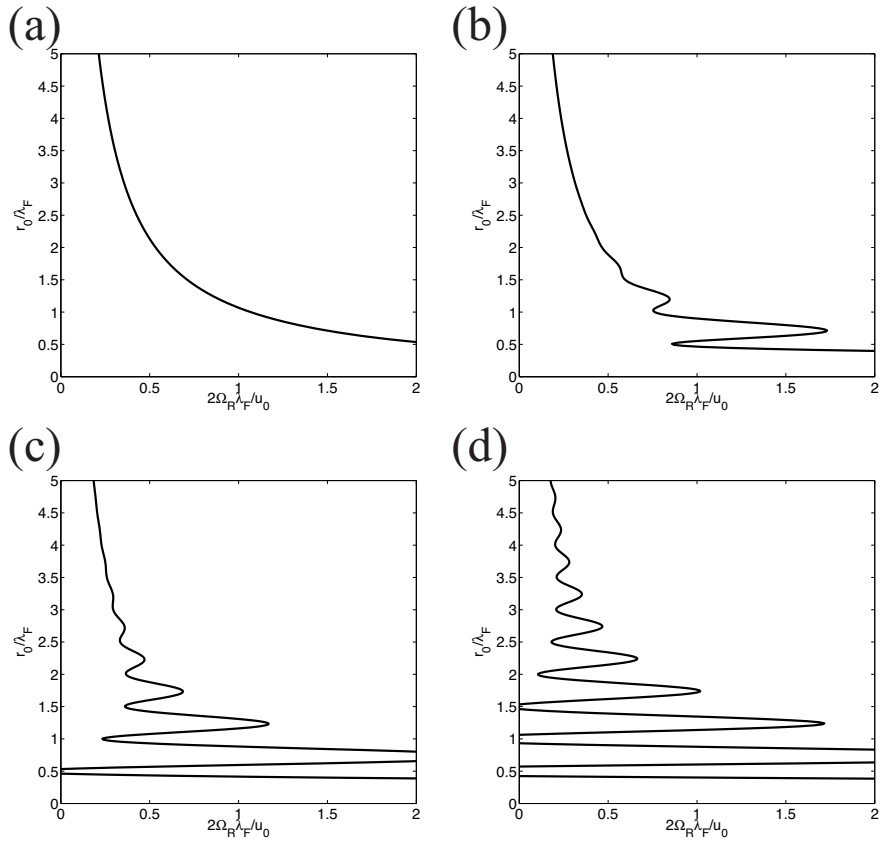

Figure 8.2: The relation between the theoretical circular orbital radius r_0/λ_F and the dimensionless rotation rate $2\Omega_R\lambda_F/u_0$ for (a) $\gamma/\gamma_F = 0.85$, (b) $\gamma/\gamma_F = 0.95$, (c) $\gamma/\gamma_F = 0.97$ and (d) $\gamma/\gamma_F = 0.98$.

values of r_0 exists for a single value of Ω, i.e. the function can not be regarded as a bijection. For this reason we choose r_0 and γ/γ_F as the parameters to vary numerically. Experimentally, the rotation rate is used, but one can uniquely compute this quantity from r_0.

An important result concerns the stability of the circular orbits. Oza *et al.* [75] showed, by doing linear stability analysis around the circular orbits and changing to polar coordinates, that the branches on the r_0-Ω_R curve which had $\frac{dr_0}{d\Omega} > 0$ were unstable in the sense that the linearized problem had eigenvalues with a positive real part. The converse, that $\frac{dr_0}{d\Omega} < 0$ gives circular orbits, is not true in general, and this is the motivation for the current study.

The governing equation (8.7) was implemented in MATLAB and solved by an Adams-Bashforth 4-point multistep method. This method requires four initial points in order to extrapolate the next, so all computations were started in a circular orbit of the kind shown in Eq. (8.8). Furthermore, a small perturbation was added in x- and y-direction to ensure that the orbit would not be trapped in a small invariant unstable subspace [77]. The time-step taken at each simulation depends on the value of M_e (or γ/γ_F), and was between $\Delta t = 2^{-5}$ at low memory and $\Delta t = 2^{-9}$ at very high memory. The maximum time simulated, tmax, depended on the degree of statistics needed, and was between tmax = 1000 and tmax = 20000. The integral was computed using Simpson's rule [80].

By simulations and sweeps in parameter space, a regime diagram has been produced. We classify the observed orbits in a limited number of categories which are then investigated in depth. In increasing order of complexity, the qualitative behaviors found are circular orbits, unstable orbits, wobbling circular orbits, drifting circular orbits , wobbling-leaping orbits, and erratic orbits.

8.1 Regime diagram

A full numerical exploration of the r_0/λ_F-γ/γ_F plane is shown in Figure 8.3. Essentially, the observed orbits can be classified in the six categories shown below the diagram. For low memory, $\gamma/\gamma_F < 0.92$ the orbits are circular for all r_0. Increasing the forcing then gives rise to the emergence of several tongues in which the orbit, started at some value of r_0, spirals outwards away from the circular solution and settles in another circular orbit with a radius different from r_0. These tongues occur at $r_0/\lambda_F = 0.6$, $r_0/\lambda_F = 1.1$, and $r_0/\lambda_F = 1.6$, i.e. with a spacing of $\frac{1}{2}\lambda_F$. They grow in width as the forcing is increased, and reflect the appearance of a real, positive eigenvalue in the linear stability analysis [75]. At very high memory, $\gamma/\gamma_F > 0.97$, erratic orbits are observed

inside these tongues. This is possibly due to the overlap of other tongues, and indeed we observe three new bands at the following values of $(r_0/\lambda_F, \gamma/\gamma_F)$. $n = 0$: $(0.35, 0.965)$, $n = 1$: $(0.85, 0.95)$, and $n = 2$: $(1.35, 0.96)$. Comparing with [75], these new tongues seem to reflect solutions with complex eigenvalues with positive real part in the linear analysis. For the two right-most tongues

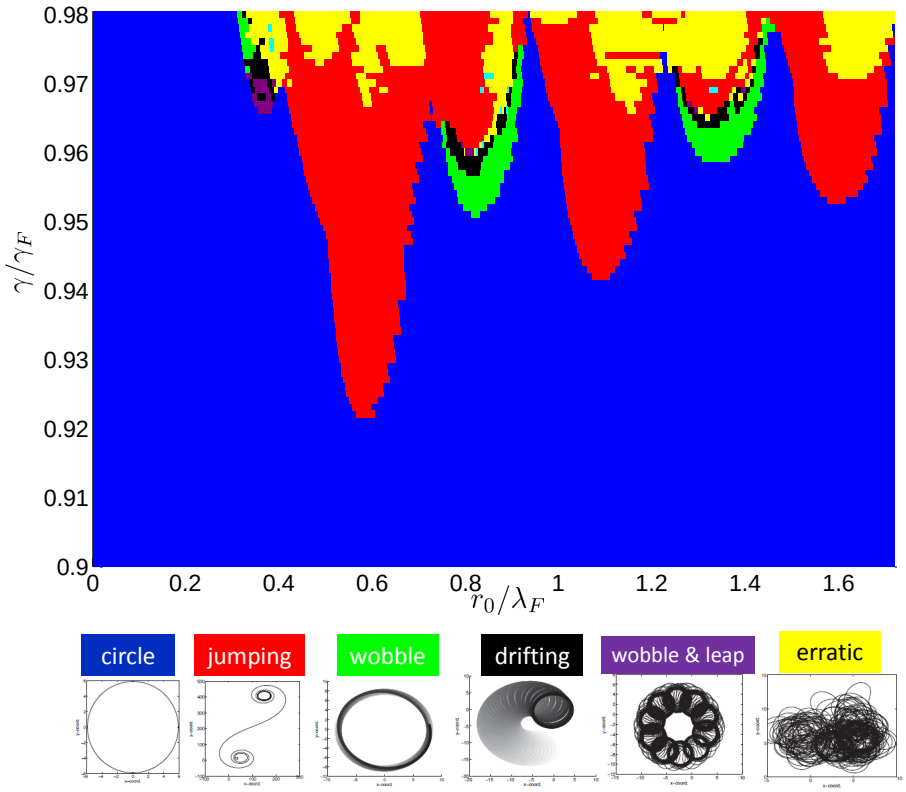

Figure 8.3: Regime diagram for Eq. (8.7). For a given value of γ/γ_F, the drop is initialized in a circular orbit of radius r_0. The corresponding value of Ω_R is calculated using Eqs. (8.9)-(8.10). The drop is given a perturbation $\delta = (0.02, 0.01)$ at time $t = 0$. The solution is obtained using using a time evolution ranging from $\Delta t = 2^{-5}$ to $\Delta t = 2^{-9}$, and at least tmax $= 1000$. Furthermore, $\Delta\gamma/\gamma_F = 0.001$, and the spatial resolution in r_0 varies from $\Delta r_0/\lambda_F = 0.1$ to $\Delta r_0/\lambda_F = 0.5$.

$(n = 1, 2)$, the evolution when increasing the forcing, apparently starts with a circular orbit onto which an additional frequency is imposed, resulting in what looks like a wobbling orbit. Then follows a type of orbit that seems to

be comprised of circular orbits, where the center of these circles drifts in some way. At the very high memory limit, the orbits are a mix between unstable and erratic, where the latter is characterized by a spaghetti-like structure.

In the left-most tongue ($n = 0$) we observe a class of wobble-leap orbits in which the orbit is wobbling and after a period of time jumps from into another wobbling orbit with the same radius, but different coordinates of the center of the orbit. Following this strange behavior is then the drifting, wobbling and ultimately erratic behavior at very high memory. We will now describe and characterize each of these classes individually.

8.2 Wobbling orbits

A common feature in the regime diagram is the emergence of a wobbling state when crossing from a stable region into the light-green region (see Figure 8.3). In doing so, a second frequency is observed, the first being ω, which is the frequency associated with the circular orbit. The wobbling frequency ω_{WOB} is close to $n_w\omega$, where n_w is an integer, depending on the system parameters. To compute the radius of a given orbit, a Fourier analysis of the trajectory is done, giving rise to a frequency ω_N, the numerical oscillation frequency of the circular orbit of the drop, and the associated period T_N. The coordinates of the center of the orbit can now be computed as $(x_c, y_c) = (\overline{x}, \overline{y})$, where the average is done over the period T_N. This allows us to compute the instantaneous radius of the orbit as

$$\overline{r}(t) = \sqrt{(\overline{x} - x(t))^2 + (\overline{y} - y(t))^2}. \tag{8.11}$$

This approach works when the orbits are well-behaved and have an nearly circular oscillation. When dealing with the erratic orbits, we need to compute the instantaneous radius of curvature by considering a finite number of data points that comprise a far from periodic circular solution.

In Figure 8.4 a numerical plot of two orbits with approximate wobbling frequency 2ω and 3ω is shown. The effect of the wobbling on the circular orbit is seen to be ellipsoidal for $n_w \approx 2$, Figure 8.4(a), and for $n_w \approx 3$, the trajectory deforms into a triangular-like shape, Figure 8.4(c). Since the simulations are started in a non-equilibria (a circular orbit), it is possible to track the evolution from the circular state to the new steady state. This is depicted in panels (b) and (d), where the orbital radius r is plotted as a function of time. For the stable circular orbit, this radius would be constant. However, in the wobbling case, the radius grows exponentially for $0 < t < 10$ and $0 < t < 45$, and then saturates and the new steady state is reached at $t = 12$ and $t = 70$. The sub-panels of (b) and (d) shows a zoom of $r(t)$, illustrating the frequency of the oscillations.

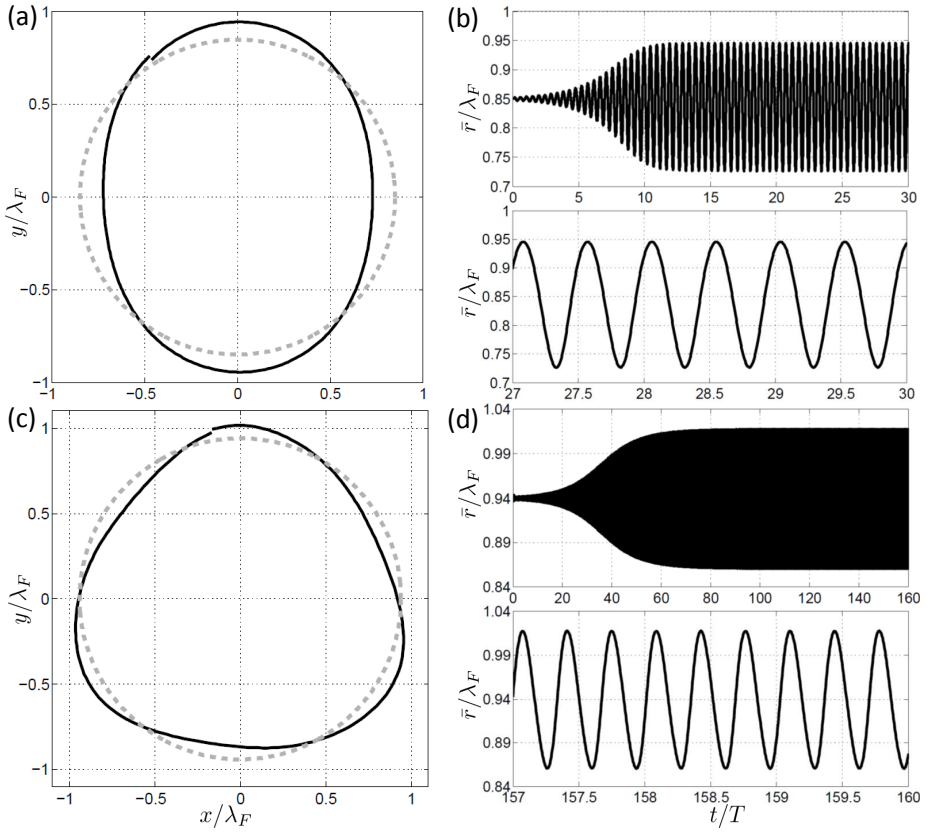

Figure 8.4: (a) and (c): Examples of wobbling orbits. Panel (a) shows a nearly 2ω wobbling orbit, and (c) a nearly 3ω wobbling orbit. The corresponding (unstable) circular orbit is indicated by the dashed line. (b) and (d): Plots of the orbital radius $r(t)$ as a function of t/T, where T is the orbital period. In the upper plots, note that the radius grows and then saturates, which is characteristic of a Hopf-type instability. The lower plots are zoomed in, and show that the wobbling frequency is $\approx 2\omega$ in (b) and $\approx 3\omega$ in (d).

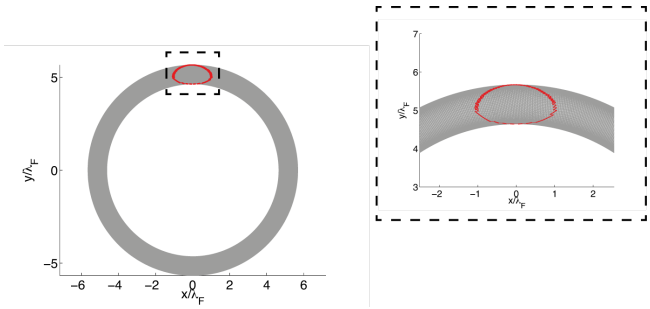

Figure 8.5: A wobbling orbit at $\gamma/\gamma_F = 0.9533$ and $r_0/\lambda_F = 0.8316$. The gray curve is the actual trajectory, the red curve is the (x, y) coordinate at each revolution, where $\dot{x}(t) = 0$, i.e. a Poincaré map. The Poincaré map appears to be an invariant closed set, indicating that a Torus (or secondary Hopf) bifurcation has occured.

A behavior with exponential growth and then a saturation into a limit-cycle is the characteristics of Hopf-type bifurcations, and to investigate this further, a Poincaré map of the wobbling orbit is presented in Figure 8.5. The surface of intersection is chosen to be where $\dot{y}(t) = 0$, and $\dot{x} > 0$, giving rise to the red points in the figure, which correspond to (x, y) values of the intersections. These points illustrate the Poincaré map for the wobbling orbit [81]. The black curve in the figure is the actual trajectory of the drop. We note that for the circular orbit, a corresponding Poincaré map would have produced a single point, but in the case of a wobbling orbit it appears to be a closed invariant curve, indicating that a torus bifurcation (also known as a secondary Hopf bifurcation) has occurred.

A comparison of the numerical (panels (a) and (c)) and experimental (panels (b) and (d)) wobbling amplitude and frequency is shown in Figure 8.6. The markers correspond to different values of memory, indicated by the legend at the bottom of the figure. There is a good qualitative agreement in the wobbling amplitude, as indicated in panels (a) and (b), where the normalized amplitude is plotted as a function of the normalized rotation rate. The amplitude grows fast after reaching a critical point, and then saturates. However, the curves are not symmetrical and in the higher memory, other types of orbit occur, yielding the disconnected data sets.

As stated previously, the wobbling frequency depends on the system parameters. This is illustrated in panels (c) and (d), where a plot of $\omega_{\mathrm{WOB}}/\omega$ is shown for the numerics and experiments, respectively. Where the wobbling amplitude was a function of the memory, the frequency appears not to be. There is a good agreement between the observed numerical and experimental wobbling frequencies. The numerical results, however, present a more complete picture

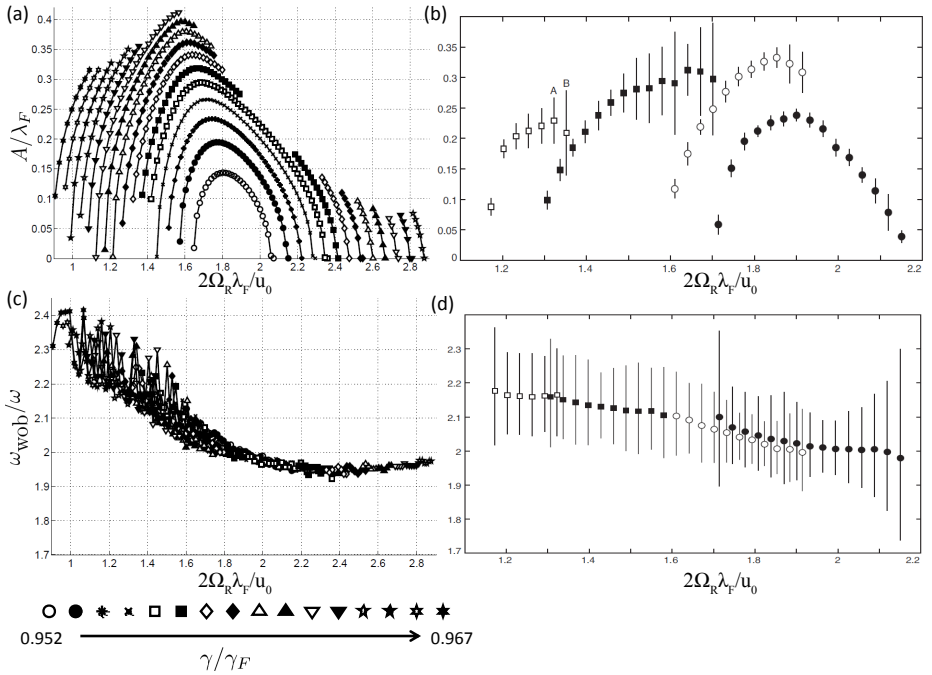

Figure 8.6: Numerical characterization of wobbling orbits (panels (a) and (c)), compared against experimental data from [82] (panels (b) and (d)). Panels (a) and (b) show the dependence of the wobbling amplitude A on the rotation rate Ω_R for various values of memory γ/γ_F. Panels (c) and (d) show the dependence of the wobbling frequency ω_{wob} on the rotation rate Ω_R. The wobbling frequency is normalized by the orbital frequency ω. The symbols in panels (a) and (c) correspond to different values of the memory γ/γ_F, as shown in the legend at the bottom.

of the dependence on the rotation rate simply because more data is obtainable.

8.3 Precessing (drifting) orbits

By increasing the memory, we encounter the next class of orbits, namely a type of precessing or drifting orbits. These are orbits where the center of the orbit precesses in some shape, and they are found in the regions marked with black coloring in the regime diagram, Figure 8.3. A numerical example of a drifting orbit is seen in Figure 8.7(a), where the actual trajectory is the gray curve and the center orbit is marked with solid black. The trajectory consists of a single loop, marked by the dashed black curve. Apparently, the center orbit precesses in a circle. Panels (b) and (c) depict the orbital radius as a function of time and the orbital center coordinates (x_c, y_c) as a function of time. Note that the time-axis is similar in the two plots, showing that the center orbit drifts on a much slower timescale than the actual droplet trajectory. The two lower panels, (d) and (e), shows the similarity of a specific numerically computed orbit with an experimentally observed orbit. In panel (e), the solid red curve is the center orbit and the dashed gray line is the droplet trajectory.

The drifting orbits come in seemingly different classes, but it turns out that they can be well approximated by two frequencies and two amplitudes. Before we classify the orbits, let us consider the case where the center orbits in a circle, i.e. the situation shown in Figure 8.7(a). We want to investigate the drifting orbits, and recalling the regime diagram in Figure 8.3, for a suitable fixed memory, the usual picture when sweeping through r_0 is a circular orbit evolving into a wobbling circular orbit which then becomes a drifting orbit. Increasing r_0 further results in the transition into another wobbling region, and in the end circular orbits again emerge. This is shown in Figure 8.8, where panels (a), (b), (c) are for $\gamma_/\gamma_F = 0.957$, and panels (d), (e), (f) are for $\gamma_/\gamma_F = 0.958$.

The top panels, (a) and (d), show the theoretical orbital radius r_0 as a function of nondimensional rotation rate $2\Omega_R\lambda_F/u_0$. The blue colored line indicates that the observed orbit is circular, the green line that the orbit is unstable in some sense (in this case, wobbling or drifting). The vertical lines and markers on part of the green segment represents the amplitude of the wobbling circular orbit, which is comparable to the previous Figure 8.6, panels (a) and (b). The mid-region on the green line is where drifting orbits are observed. Evidently, as the memory is increased, the wobbling region gets smaller and the drifting region expands. Panels (b) and (e) shows the radius with which the center orbit drifts, R_{drift}, normalized by the Faraday wavelength. For $\gamma_/\gamma_F = 0.957$ the function is concave whereas for $\gamma_/\gamma_F = 0.958$, part of the function becomes convex. The

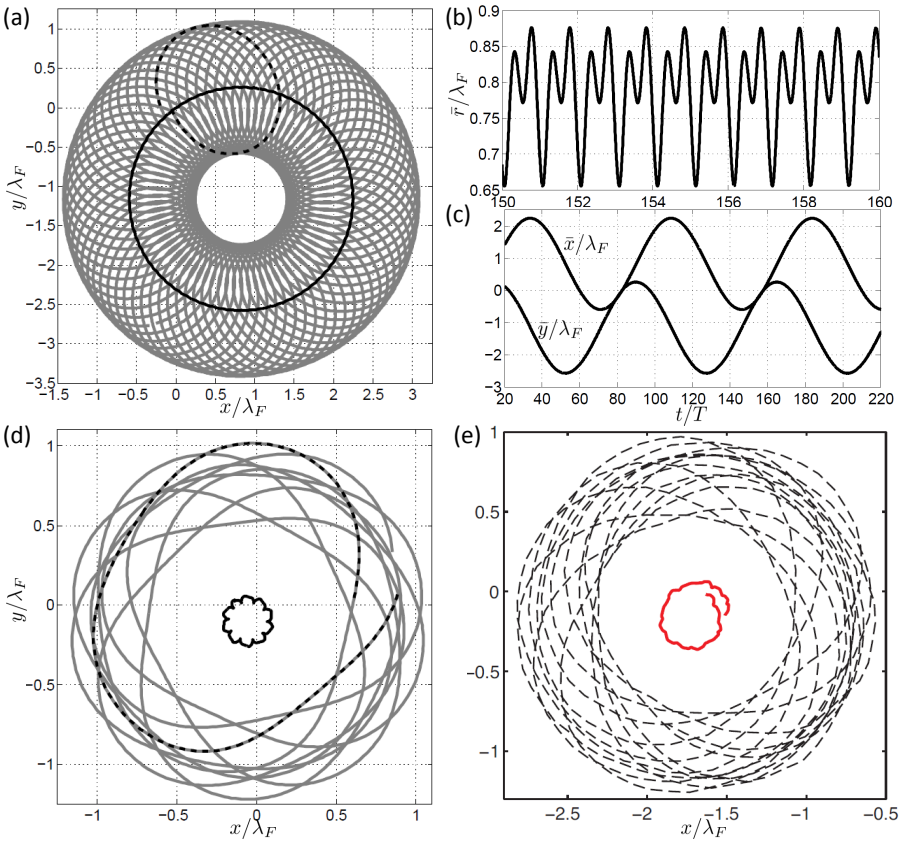

Figure 8.7: (a) Numerical simulation of a drifting trajectory at $n = 1$. The trajectory (gray line) consists of a loop (black dashed line) drifting along a larger circle (black solid line). (b) Plot of the orbital radius $r(t)$ as a function of t/T, where T is the orbital period. (c) Plot of the orbital center (x_c, y_c) as a function of t/T . Note that the center moves on a much slower timescale than the radius r. (d) Numerical simulation of another drifting trajectory, in which the center does not move along a precise circle. (e) Experimentally observed drifting trajectory from [82] . The trajectory is indicated by the black (dashed) line, and the center by the solid red line.

bottom panels (c) and (f) shows the drifting period T_{drift} normalized with the orbital period T_{orb}, again confirming that the timescale of the drifting behavior is much greater than the timescale of the orbital behavior. Where we, in the previous section, explained the transition from a stable circular orbit to a wobbling orbit by a Hopf type of bifurcation, there is no apparent reason for the emergence of the drifting orbits.

As mentioned, there exists different types of precessing orbits. In Figure 8.9 a selection is shown for the $n = 0$ and $n = 1$ branch. By varying the rotation rate, it is possible to observe the transition from orbits where the center drifts in star-shaped patterns with an increasing number of "corners". The number of corners is sometimes hard to define, since the curves are not periodic, i.e. they do not close. It actually turns out, that these center orbits can be thought of as epicycles, which in the general form in Cartesian coordinates can be written

$$\begin{pmatrix} x(t) \\ y(t) \end{pmatrix} = \sum_k a_k \begin{pmatrix} \cos(\omega_k t + \phi_k) \\ \sin(\omega_k t + \phi_k) \end{pmatrix} + \begin{pmatrix} c_x \\ c_y \end{pmatrix}, \tag{8.12}$$

where a_k is the amplitude, ω_k is the frequency of the oscillation and ϕ_k is the phase, and c_x, c_y are constants. Epicycles of order 2 have the following expression

$$\begin{pmatrix} x(t) \\ y(t) \end{pmatrix} = a_1 \begin{pmatrix} \cos(\omega_1 t + \phi_1) \\ \sin(\omega_1 t + \phi_1) \end{pmatrix} + a_2 \begin{pmatrix} \cos(\omega_2 t + \phi_2) \\ \sin(\omega_2 t + \phi_2) \end{pmatrix} + \begin{pmatrix} c_x \\ c_y \end{pmatrix} \tag{8.13}$$

The epicycles are different from the usual Fourier transform since it is assumed that the orbit is symmetric in x and y, with only a possible difference in the phase. We fitted epicycles to the x and y component of the orbits observed in the top-row of Figure 8.9, by using a least squares optimization method, and surprisingly, all the precessing orbits could be characterized by an epicycle of order 2. The fitted values for the two coordinates gave to good approximation the same value. This means that each of these orbits has, essentially, two amplitudes and two frequencies associated with it. We also tried to further increase the order of the epicycle fit, but this did not yield changes in the leading terms. Figure 8.10 show the data along with the fitted curves, and Table 8.1 contains the fitted values. We note that the amplitude a_1 is actually approximately equal to r_0, indicating that the center orbit precesses around the originally specified radius for the drop orbit. The aperiodic nature of the orbits originate in the ratio $\frac{\omega_1}{\omega_2}$. If both these numbers are rational, the epicycle yields a closed periodic curve. Consider Figure 8.10(b), which indeed looks remarkably periodic. For this specific orbit, $\frac{\omega_1}{\omega_2} = 3.0065$, which is indeed close to an integer. Similarly for the 5-corners orbit we have $\frac{\omega_1}{\omega_2} = 4.4481$ and as visualized, the orbit does not seem to close. Note however, that the orbits have been plotted for a short amount of time, and that it is not possible, in general, to determine visually if an orbit closes or not within this period. Of all the possible combinations of the

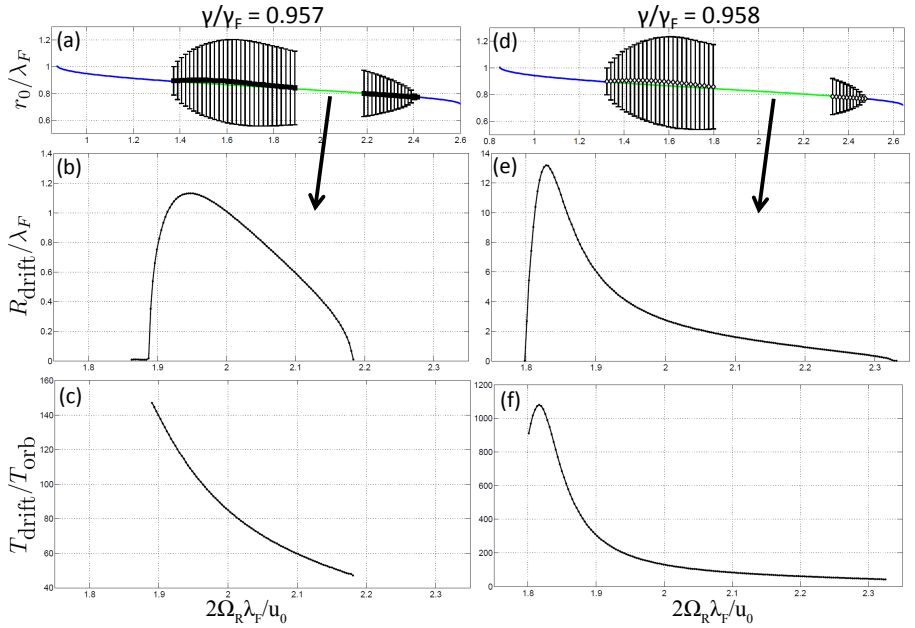

Figure 8.8: Numerical characterization of drifting orbits at $n = 1$. Top panels (a) and (d): the curve shows the theoretical orbital radius r_0 as a function of the nondimensional rotation rate $2\Omega_R\lambda_F/u_0$, calculated using Eqs. (8.9)-(8.10). The blue segments indicate circular orbits, and the green unstable solutions due to an oscillatory instability. The trajectory equation (8.7) was numerically simulated within the green regions, and both wobbling and drifting orbits were found. The markers correspond to the mean orbital radius $\bar{r}$ of a wobbling orbit, and the error bars indicate the wobbling amplitude. The unmarked green regions correspond to drifting orbits, in which the orbital center (x_c, y_c) drifts in a circle. Middle panels (b) and (e) show the radius R_{drift} of the orbital center, and the lower panels (c) and (f) the period of the orbital center T_{drift} normalized by the orbital period T_{orb}. Panels (a–c) correspond to $\gamma/\gamma_F = 0.957$ and (d–f) to $\gamma/\gamma_F = 0.958$.

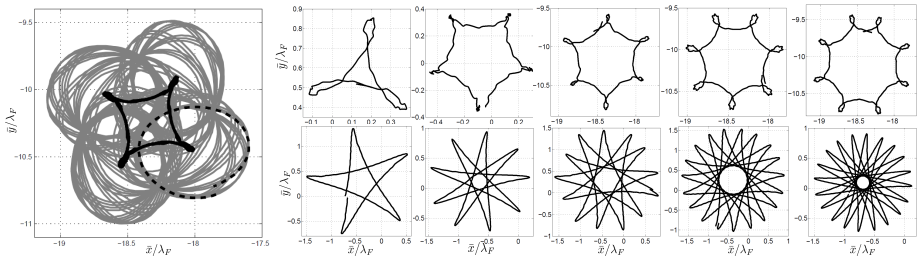

Figure 8.9: Numerical simulations of drifting orbits, for various values of γ/γ_F and rotation rate Ω_R. In the leftmost figure, the gray curve corresponds to a trajectory, which consists of a loop (dotted black curve) that drifts along a square epicycle (black curve). The plots along the top row show the orbital centers of some drifting orbits at $n = 0$, and the bottom row shows those corresponding to $n = 1$.

	a_1 $[2\pi/\lambda_f]$	$a_2[2\pi/\lambda_f]$	$\omega_1[1/t]$	$\omega_2[1/t]$
3-corners	0.6345	1.1920	0.7138	0.3157
4-corners	0.7256	1.7608	0.6449	0.2145
5-corners	0.8186	1.9796	0.5658	0.1272
6-corners	0.7787	3.0088	0.5810	0.1111
7-corners	0.7968	3.0568	0.5587	0.0911
8-corners	0.7931	3.6190	0.5607	0.0837

Table 8.1: Table with fitted values for the orbits

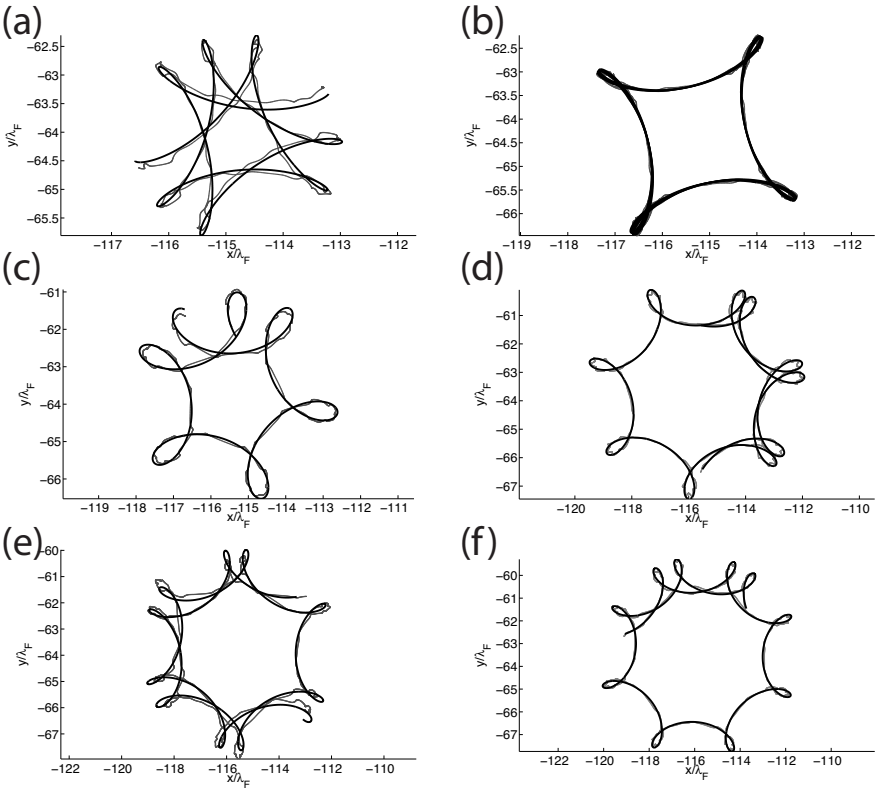

Figure 8.10: Plots of epicycles with (a) 3 corners, (b) 4 corners, (c) 5 corners, (d) 6 corners, (e) 7 corners, and (f) 8 corners. The solid gray line is the numerical data and the solid black line is the fitted trajectory.

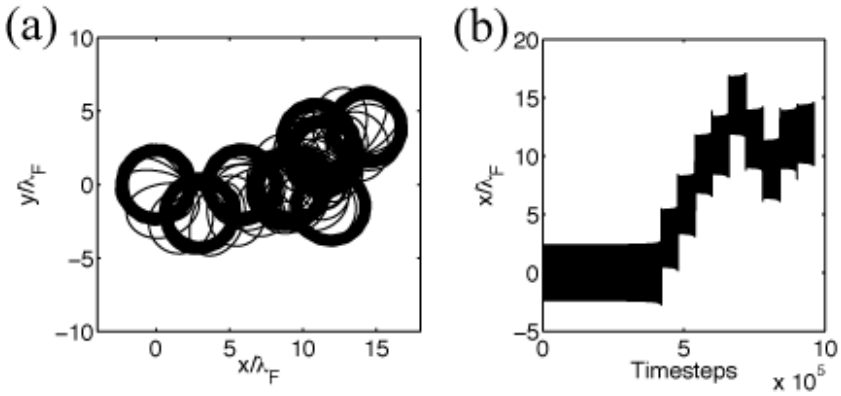

Figure 8.11: (a) The (x, y) numerical trajectory of a droplet in a wobble-leap orbit. (b) $x(t)$ of the same orbit, indicating the time spent before leaping.

parameters in Table 8.1, we found the most useful one, in terms of classifying the precessing orbits, to be the ratio $\frac{\omega_1}{\omega_2}$.

8.4 Wobble-leap dynamics

The next interesting situation is denoted wobble-leap, owing to the fact the orbit wobbles in a circular orbit in a transient period, after which it leaps and settles at another position in space. This latter behavior is repeated, and the time between leaps can be periodic or aperiodic. An example of this type of orbit is shown in Figure 8.11, where panel (a) shows the (x, y) trajectory of the droplet. Clearly, the drop switches between different positions in the plane. To get a clearer view of the time spent wobbling before leaping, panel (b) shows $x(t)$, where the time is given as the number of time-steps taken. The initial condition is a circular orbit with radius r_0, and we observe a transient period of wobbling ($0 < t < 4 \cdot 10^4$), before the drop leaps the first time. Consequently, the drop is "trapped" in the wobble-leap dynamics. By computing a Fourier spectrum where increasingly more time-steps are included, we have observed the exponential growth of the frequency related to the wobbling, see Figure 8.12. The evolution of this frequency is related to the orbital radius in the orbit, $\overline{r}(t)$. Loosely speaking, the leaping could occur when the drop can access the next level of radiis, i.e. when the wobbling of the orbital radius is roughly equal to $\lambda_F/2$. In Figure 8.13, $|\overline{r}(t)|$ is plotted for a wobble-leap orbit at $\gamma/\gamma_F = 0.965$ and $r_0 = 0.370$. The vertical lines are computational errors induced when the

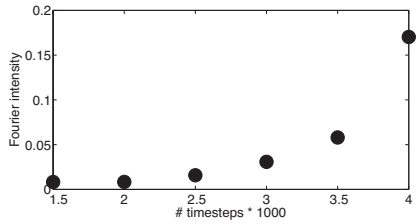

Figure 8.12: The normalized amplitude of the frequency related to wobbling.

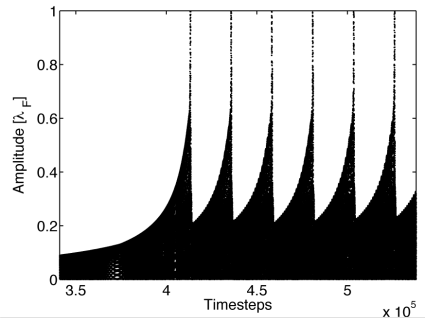

Figure 8.13: The orbital radius $\overline{r}(t)$ as a function of the timesteps taken for a wobble-leap orbit at $\gamma/\gamma_F = 0.965$ and $r_0 = 0.370$.

drop leaps to the next position in space and do not reflect the actual radius. We note that the drop leaps when the wobbling is on the order of $\lambda_F/2$, but the exact value is not constant but we have not found any relevant dependence on system parameters so far.

However exotic this wobble-leap trajectory may seem, it also exists experimentally. In Figure 8.14 we compare a specific numerical trajectory, (a) and (b), to an experimentally observed orbit, panel (e). The solid curve in (b) is the center orbit with the stable points of wobbling denoted with black markers. Similarly, the center orbit is marked with a red solid line in (e), and we note the resemblance between the two orbits. Panels (a), (c) and (d) shows the orbital radius, x-component of the trajectory, and y-component of the trajectory, respectively.

To illustrate the variety the wobbling-leaping orbits come in, Figure 8.15 is presented. Here, the orbital center motion (x_c, y_c) is depicted for various values of memory and rotation rate at the $n = 0$ branch.

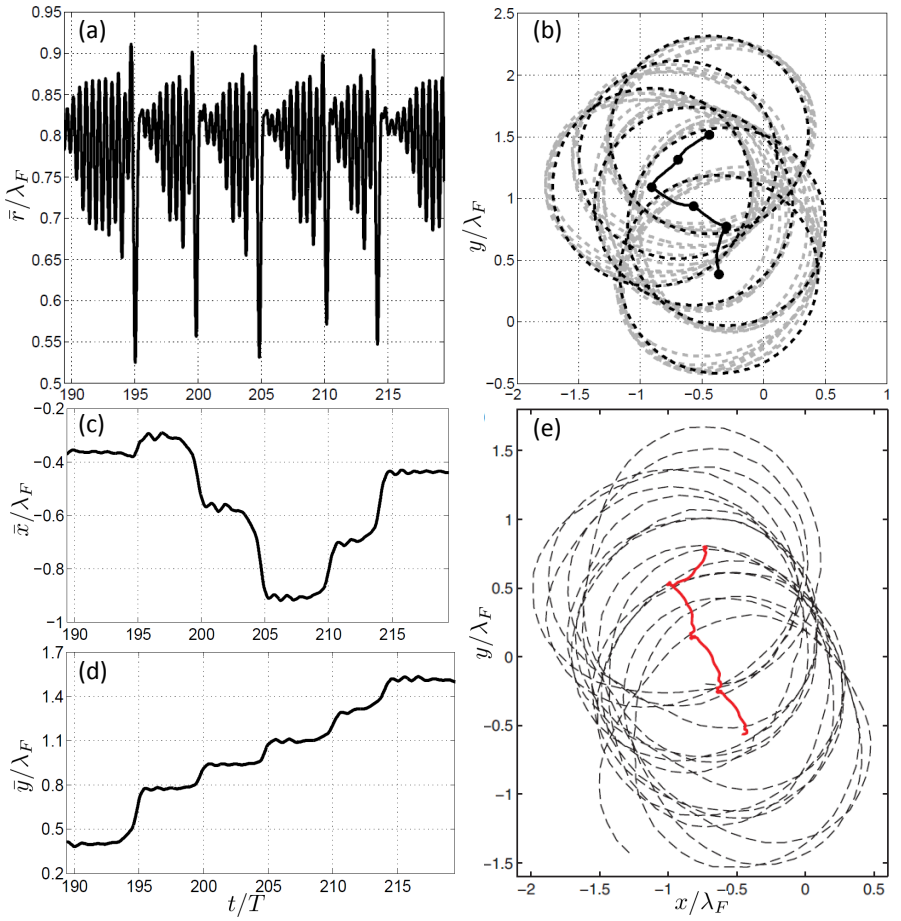

Figure 8.14: Numerical simulation of a wobble-and-leap trajectory at $n = 1$. Panel (a) shows the mean orbital radius $\bar{r}(t)$. Panel (b) shows the trajectory (dotted gray curve), in which the orbital center (solid black curve) jumps between the transiently stable points (black dots). The dotted black curves show circles of radius r_0 centered on the stable points. Panels (c) and (d) show the coordinates $x_c(t)$ and $y_c(t)$ of the orbital center. Panel (e) shows an experimentally observed wobble-and-leap trajectory from [82]. The trajectory is indicated by the black (dashed) line, and the center by the solid red line.

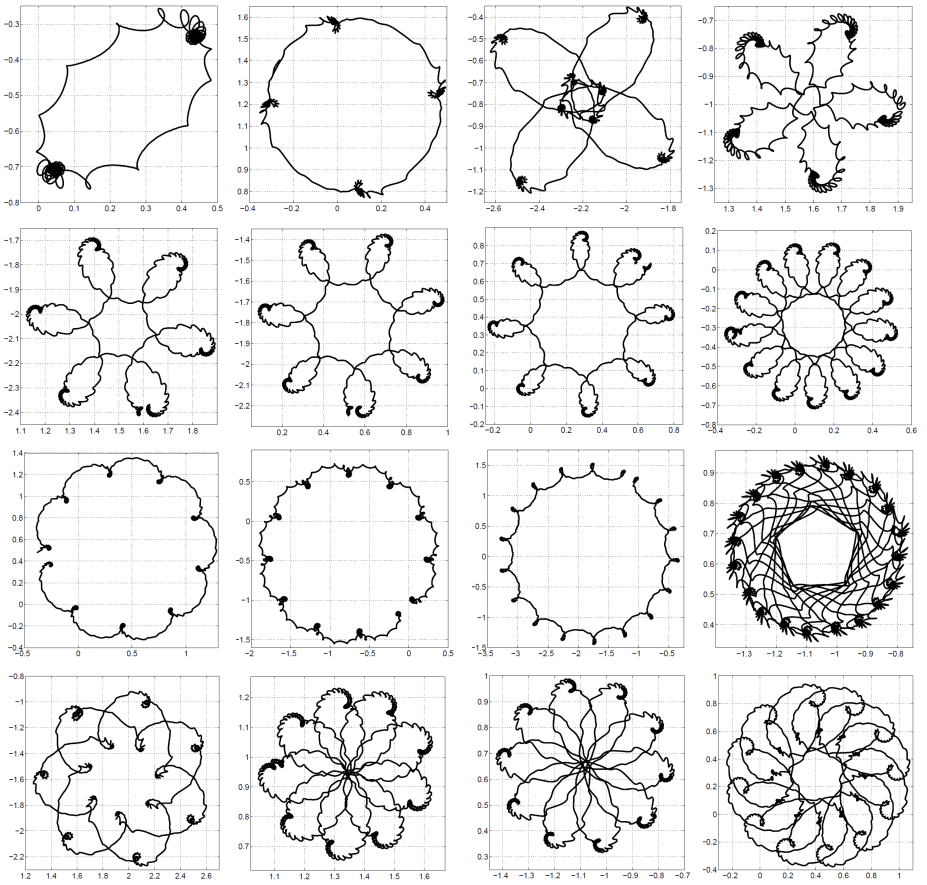

Figure 8.15: Numerical simulations of wobble-and-leap trajectories at $n = 0$, for various values of memory γ/γ_F and rotation rate Ω_R. The plots show the motion of the center (x_c, y_c).

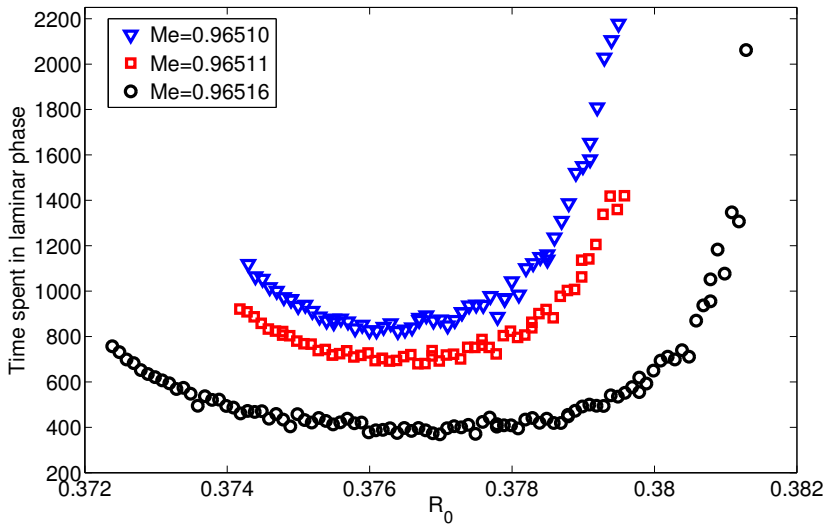

Figure 8.16: The average time spent in the laminar phase as a function of the bifurcation parameter r_0 for three different memory values.

As a final remark, we will relate the wobble-leap behavior to a phenomenon called intermittency, also seen in dynamical systems. Intermittent behavior is observed as (random) alternations between long regular (laminar) phases, and short bursts [83]. In our system, we identify the wobbling as the laminar phase, and the very short time with which the droplet leaps to a new attractor, as the burst phase. The average length of the laminar phase, $< l >$, follows a scaling law,

$$< l > \propto |p - p^*|^{-\alpha}, \tag{8.14}$$

where p is a bifurcation parameter, p^* is the critical onset point for the intermittent behavior, and $\alpha > 0$ is a scaling exponent [84]. This law can be found analytically for some ordinary differential equations, and for other more complicated systems it can be computed numerically.

Different types of intermittency (type I, II, and III) gives different values of α (1/2, 1, 1, respectively). The typical values for α are computed for lower-dimensional systems, where our system is of very high dimension due to the inclusion of the wave force memory. In Figure 8.16 $< l >$ is plotted as a function of r_0, for three different memory values. We have attempted to fit the function

$$< l >= |r_0 - r_0^*|^{-\alpha} + c, \tag{8.15}$$

to the right-most points of the three simulations, this is shown in Figure 8.17.

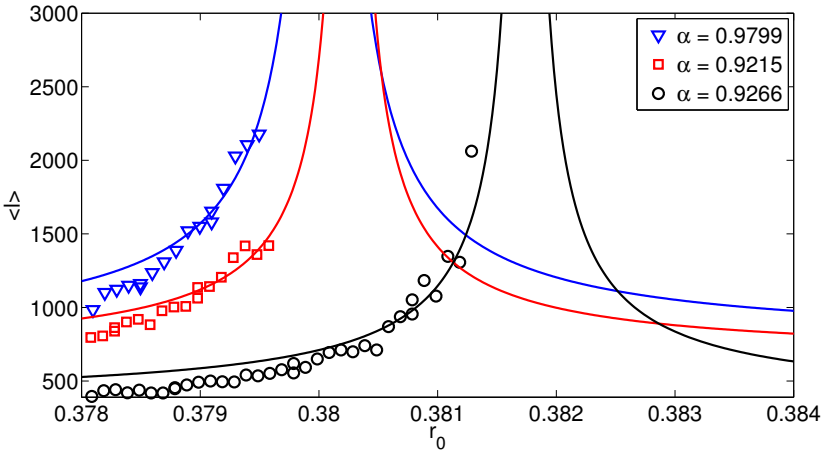

Figure 8.17: The right-most points of Figure 8.16, and the fitted functions of the type $< l >= |r_0 - r_0^*|^{-\alpha} + c$.

The fits are far from perfect, and the shown value of α has interval confidence bounds up to ± 0.5. Nevertheless, this could indicate an exponent close to $\alpha = 1$ for all three memories.

8.5 High-memory dynamics

The final section regarding the bouncing droplets in the rotating set-up deals with the behavior at very high memory. Referring back to the regime diagram, Figure 8.3, we see that the drops orbit with seemingly erratic behavior for almost all values of r_0. An example of an erratic orbit is shown in Figure 8.18(a).

Such an orbit appears to be difficult to characterize due to the rapidly varying curvature and spaghetti-like appearance. However, there is some structure to be identified if the local radius of curvature is computed, which is shown in Figure 8.18(b). The drop prefers to orbit in certain radiis, switching back and forth between these in some way. If a histogram of the radius is collected, we obtain panel (c), where the dotted red lines show the zeros of the Bessel function $J_0\,(k_F r)$. To understand why these values are shown, we state two results obtained by Oza *et al.* [75]. The first result is that except for very small values of r_0, no circular orbits are stable at high memory. This is also shown in our regime diagram. The next result is obtained by considering the orbital

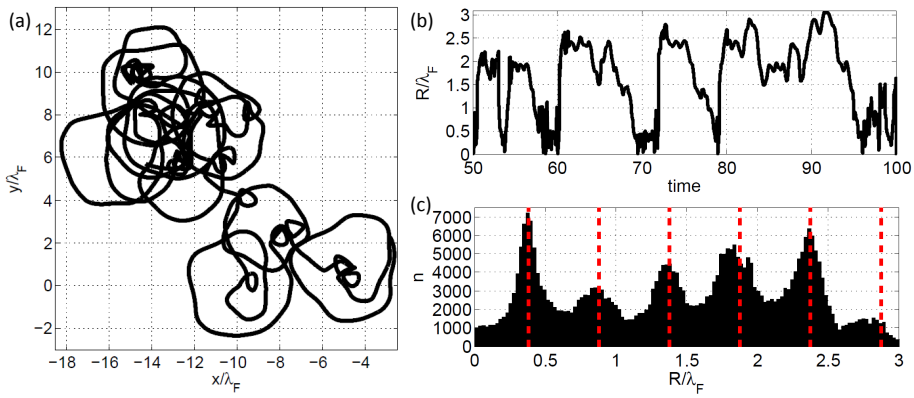

Figure 8.18: (a) Numerical solution of Eq. (8.7) from $t = 25$ to $t = 100$ in the high-memory regime, for nondimensional mass $\kappa = 0.08635$, wave force coefficient $\beta = 505.6$, and rotation rate $\Omega_R = 0.15$. The initial condition is $x_p(t) = (r_0 \cos \omega t, r_0 \sin \omega t)$ for $t < 0$, where $r_0 = 2.525$, $\omega = -8.855$ is a solution to Eqs. (8.9)-(8.10). The time step is $\Delta t = 2^{-9}$. (b) Time trace of loop radius R computed using $\alpha = \pi/2$. (c) Histogram of the local radius of curvature R of the same trajectory. Dashed vertical lines represent the zeros of the Bessel function $J_0(k_F r)$

solutions at high memory, i.e. where are solutions of the kind

$$(x, y) = (r_0 \cos(\omega t), r_0 \sin(\omega t)), \tag{8.16}$$

found for $\gamma \to \gamma_F$. One obtains by insertion in Eq. (8.7) that

$$J_0(k_F r_0) = 0, \quad \text{or} \quad J_1(k_F r_0) = 0. \tag{8.17}$$

Both these solutions are unstable in the sense that the system linearized around Eq. (8.16) has eigenvalues with a positive real part, with the magnitude of the J_1 values being larger than for the J_0 values. Evidently, the histogram is peaked around the zeros of J_0, spending a larger amount of time near these solutions.

To investigate the dependence of the orbital statistics as a function of the rotation rate, numerical sweeps were done for three memories, see Figure 8.19. At each rotation rate, a histogram was obtained showing the distribution of the local radius of curvature. The color-map reflects the most prevalent radius in red and radiis not observed in blue. The dotted line correspond to the sample distribution shown in the bottom row, which all are for $2\Omega_R \lambda_F / u_0 = 0.6$. The memories chosen are quite high, $\gamma/\gamma_F = 0.980$, 0.983, and 0.985, respectively, so only for very low rotation rates stable circular orbits are seen (with correspondingly large r_0).

If instead the rotation rate is fixed, $\Omega_R = 0.2$, and the memory increased from 0.93 to 0.99, we get the result shown in Figure 8.20. In (a), the color-map again represents the most prevalent radius as red, and radiis not observed in blue. The emergence of the statistics is evident as the memory reaches around 0.97, and the radius is significantly smeared out when increasing the memory further. It is worth noting that the droplet seems to prefer to orbit around the lowest possible radius, $r_0 \approx 0.5$, in the very high memory limit. In panel (b), the value of the real part of the eigenvalues of the solution to Eq. (8.7) linearized around a circular orbit $\mathbf{x}(t) = (r_0 \cos \omega t, r_0 \sin \omega t)$ is shown. We mentioned that such solutions, in the high memory limit, are unstable (i.e. eigenvalues with real part bigger than zero) and satisfy $J_0(k_F r_0) = 0$ or $J_1(k_F r_0) = 0$, with the magnitude of the latter eigenvalues being bigger. In the figure, blue points correspond to circular orbits, and red/yellow points correspond to orbits color-coded according to the magnitude of their most unstable eigenvalue. The red branches of the solutions, are $J_1(k_F r_0) = 0$, and these are not observed in the simulations or in experiments due to their more unstable nature.

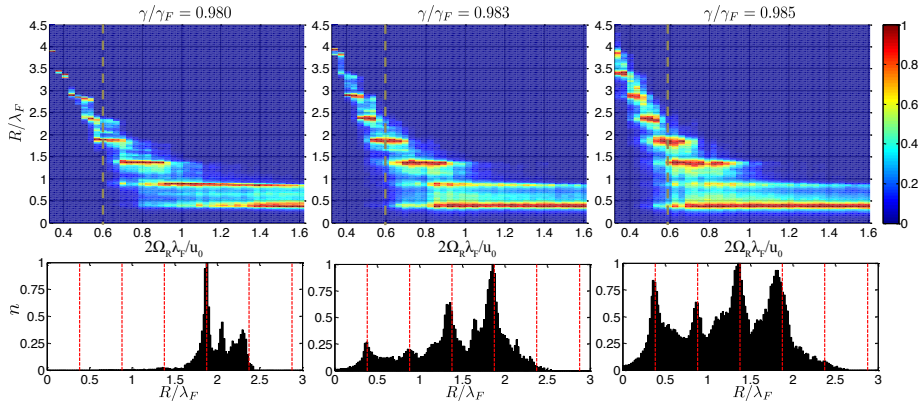

Figure 8.19: Numerical simulations showing the dependence of the orbital statistics on the dimensionless rotation rate $2\Omega_R\lambda_F/u_0$, for three different values of memory γ/γ_F. Each simulation was performed with rest initial conditions, with $\Delta t = 2^{-8}$ and tmax= 1000. In the top panels, each column is colored according to the prevalence of the corresponding loop radius R, with red segments corresponding to the most prevalent radii. The bottom panels show three sample probability distributions at $2\Omega_R\lambda_F/u_0 = 0.6$. The peaks of the probability distributions are centered around the zeros of the Bessel function $J_0(k_F r)$, indicated by the red dashed lines.

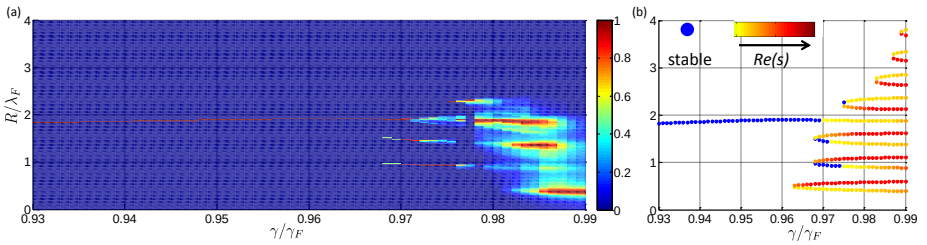

Figure 8.20: Numerical simulations showing the dependence of the orbital statistics on the memory γ/γ_F for fixed rotation rate $\Omega_R = 0.2$. For a given value of γ/γ_F, the simulations were performed with circular orbit initial conditions $\mathbf{x}(t) = (r_0 \cos \omega t, r_0 \sin \omega t)$, where (r_0, ω) define the possible circular orbit solutions of Eqs. (8.9)-(8.10). The simulations were performed with $\Delta t = 2^{-8}$, tmax $= 1000$ and initial perturbation $\delta = (0.02, 0)$. In panel (a), each column is colored according to the prevalence of the corresponding loop radius R, with red segments corresponding to the most prevalent radii. Note that the brightest segments lie near the zeros of $J_0(k_F r)$. Panel (b) shows the radii of the possible orbital solutions at $\Omega_R = 0.2$ as a function of the memory γ/γ_F , color-coded by their stability. Blue segments correspond to stable solutions, and unstable solutions are colored according to the real part $Re(s)$ of the largest unstable eigenvalue s. All of the orbital solutions are unstable at high memory, but those corresponding to the zeros of $J_1(k_F r)$ are more unstable than those at the zeros of $J_0(k_F r)$.

Chapter 9

Conclusion and Discussion

In the second Part of this thesis, we have considered the set-up where a drop bounces on a vertically vibrated surface of the same fluid. The experiment has been described, and governing equations for the vertical and horizontal motion of the drop has been presented. Two in-depth studies, one experimental and one numerical, has furthermore been given.

Experimental mode characterization

In the experimental study, we presented a characterization of the vertical bouncing mode of the droplet as a function of drop size and the system parameters. In this section, particular attention was given to the bouncing modes within the region where drops also propel themselves horizontally along the surface. To our knowledge, this was the first characterization of its kind. Several complex and exotic bouncing modes were shown by virtue of their associated spatio-temporal diagram, including a mixed-state walking drop which alternated in bouncing mode between the high and low energy $(2, 1)$ mode. The experimental characterization was extensive, and coincided remarkably well with the developed theoretical predictions. However, some things still remain to be investigated. Specifically, the role of hysteresis and the possibility of multiple solutions for the same system parameters. We did this to some degree by considering the

evolution in the bouncing mode across phase changes, but only in some regions of parameter space.

An important result is the fact that drops inside the walking region are not necessarily phase locked in a $(2, 1)$ mode, but can be bouncing in a complex, $(4, 2)$ or mixed way. When describing the horizontal dynamics mathematically, it is assumed that the drop is in the $(2, 1)$ mode, facilitating the stroboscopic approach. One has to make sure, experimentally, that the drop is in the appropriate bouncing mode to allow for comparison between numerics and experiments.

The rotating set-up

An extensive numerical study of the observed orbits of a droplet walking on a rotated, and vertically vibrated fluid bath was presented. We started by presenting the model used to describe the system, and described the unique way, in which the parameter r_0 defines the rotation rate of the fluid tray. A regime diagram containing all orbits was then presented, and subsequently, each orbit was studied. Where possible, explanations of the transitions between orbits was given, either through physical or mathematical (dynamical systems theory) arguments.

We managed to classify the observed orbits and understand most of their behavior, including some of the transitions between orbits. However, we can never be entirely sure that we have observed all behavior in the system, since the drop was initially put in a circular orbit. Possibly, other orbits could exist, which would then never be found through the numerical techniques employed in the current study. The response of the system to the small perturbation in x- and y-direction reveals some information about the structures in the near vicinity of the circular orbit, but a global picture is hard to obtain.

To mimic the experimental set-up more closely, we have also developed a method where, instead of using a single value of r_0 in each simulation, a continuous function sweeping through the rotation rate Ω_R was used. The function used was a smooth step-function, with a characteristic transition time between plateaus which was deemed long enough for the system to settle into a new solution. We wanted to investigate if the role of the history in the system could lead to significantly different behaviors. However, we did not observe any difference between this sweeping method and the point-wise one used throughout the simulations, probably because the numerics could be extended far enough for the wave-history of the previous solution to have decayed significantly.

The intermittent behavior in the system is an area to explore further. In our analysis, we considered only three memories and the number of data near the critical bifurcation point was probably inadequate. However, obtaining a fine resolution near these boundaries is nontrivial, since very long computational time is needed due to the high memory and the fast growing value of $< l >$.

Quantum mechanics

One of the reasons we are interested in the bouncing droplet system is that it serves, in some situations, as a quantum mechanical hydrodynamic analogue [58, 85]. It is a system which exhibits particle-wave duality [64], with the drop being guided by its own wave field. A similar system was envisioned by deBroglie [59], without his knowledge of the present set-up. Many analogues between quantum mechanical systems and the bouncing droplets has been presented, including single-particle diffraction [86], tunneling phenomena [87]. The rotating fluid bath presented herein has been discussed as an analogue to a charged particle in a magnetic field [65, 75, 74, 79]. Furthermore, the wave-like statistics at very high memory, shown at the end of the previous chapter, has also been demonstrated for a droplet in confined geometries [82].

Whether the quantum world behaves as fluid mechanics or not, the bouncing droplet system is interesting in its own right. As we have shown, the dynamical system is rich in behavior and has an obvious artistic appeal. Furthermore, the system can be used in teaching as an example of particle-wave duality, which is a concept that is hard to comprehend.

As a final remark regarding quantum mechanics, consider the specific case of a drifting orbit, the trajectory shown in Figure 9.1(a). It consists of loops as depicted in panel (b), and has two frequencies, or radiis, associated; one large and one smaller. This is seen in the bottom panel (c), where the orbital radius is shown. The drop periodically switches between the high and low radius, and thus has two identifiable "energy levels". Since the considered system has previously been thought of as analogous to the Landau levels of a charged particle in a magnetic field, a proposal for an analogy for the current orbit could be a Rabi cycle for a two-state quantum system.

Rabi oscillations are the oscillations back and forth between the two energy levels in the quantum system, when the system is driven at or near the resonance frequency [88]. The result is, that the probability of finding the system in its excited state oscillates in a sinusoidal way, with the probability being bigger the closer to resonance the driving is. The analogy to the observed trajectory in

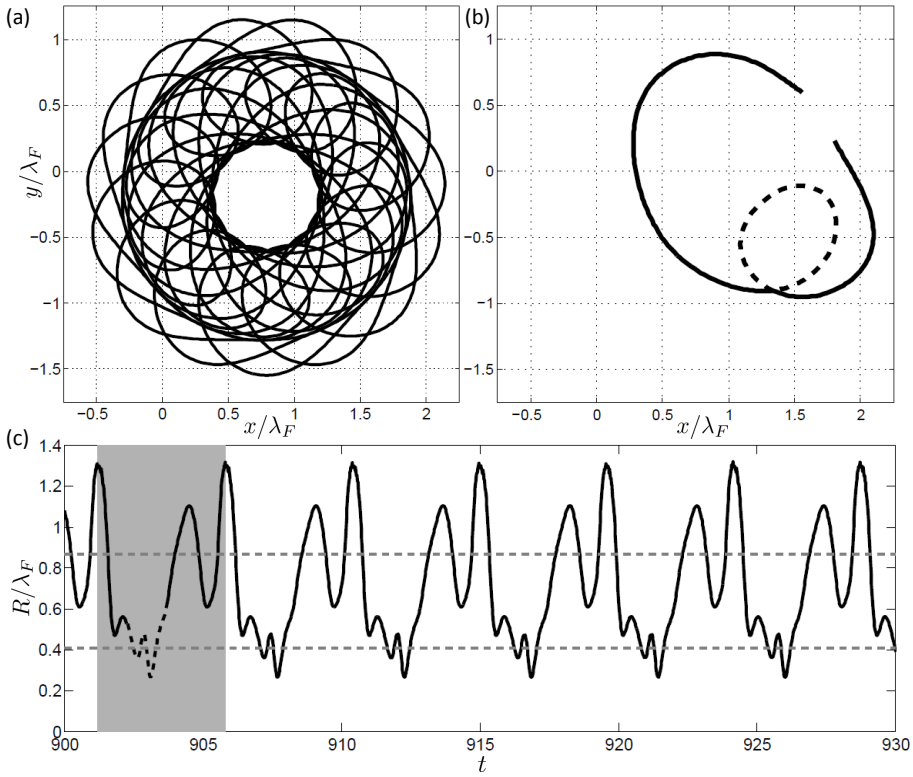

Figure 9.1: Numerical simulation of a hydrodynamical analog of Rabi oscillations. Panel (a) shows the trajectory, which consists of the loop in panel (b) drifting along a circle. Panel (c) shows the loop radius R of the trajectory. The shaded gray portion corresponds to the portion of the trajectory in (b). The drop evidently oscillates periodically between the two unstable orbital solutions indicated by the dashed gray lines

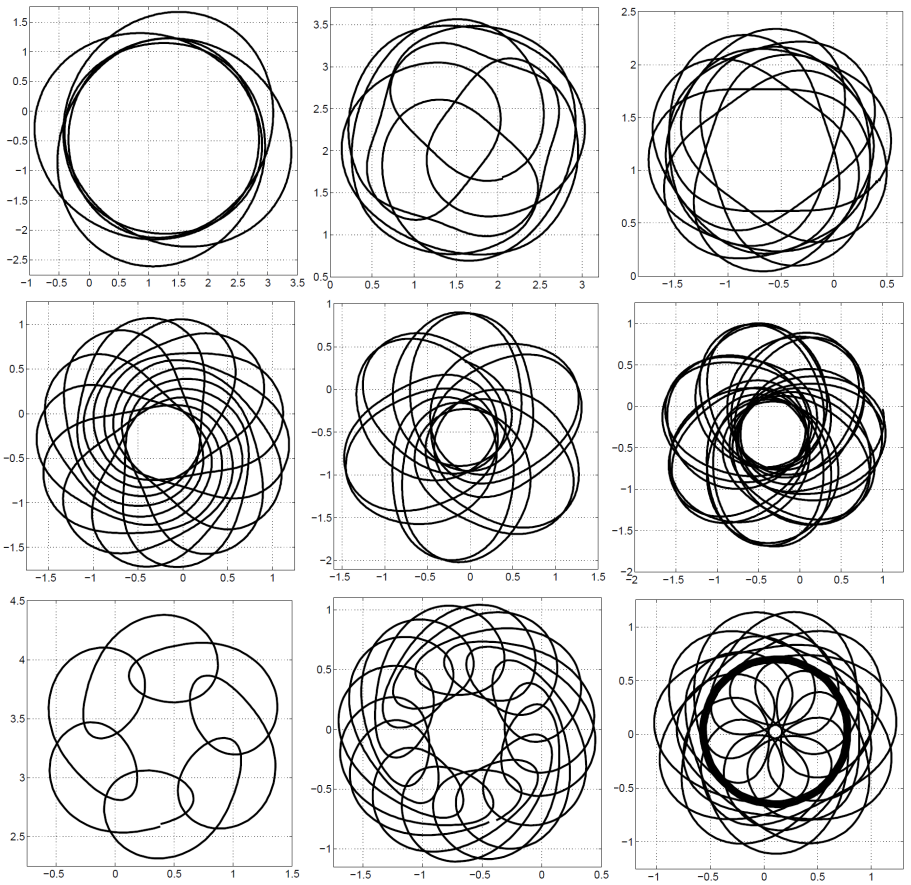

Figure 9.2: Numerical simulations of quasiperiodic trajectories for various values of memory γ/γ_F and rotation rate Ω_R.

the bouncing drops system is thus a periodic switching between energy levels, although this switching in the hydrodynamical system is not entirely sinusoidal.

While the Rabi oscillation analogy may could provide useful in understanding a quantum mechanical system, the final figure of this thesis is Figure 9.2, where several trajectories from the rotating set-up are shown, simply for their artistic appeal.

Combining Part I and II

In both Part I and II, mathematical models are used to describe the dynamics of droplets. Where the model in Part I is based on partial differential equations (PDE), ordinary differential equations (ODE) are used in Part II. One might argue that the PDE model represent a more complex set of equations which are harder to solve. However, the inclusion of the wave force through the memory integral in the ODE model is a challenge. Nevertheless, one could attempt to utilize the successful ODE model for the bouncing droplets in a setting with a hydrophobic surface, since the two situations share a similarity; when a droplet impacts a superhydrophobic surface, effects owing to the presence of an air film trapped in the structures of the surface lead to different behavior than for a flat surface [89]. The film reduces viscous friction between the drop and the solid, leading to a higher maximum spread of the drop and a possible destabilization of the rim. However, this type of phenomena is seen for high Weber numbers, $We \approx 160 \gg 1$, which violates the assumptions of the ODE model. Hence, it would require a new formulation of the drop shape as it impacts the surface. However, the bath dynamics would be simplified since it can be considered inelastic and completely rigid.

Appendix A

Papers

A.1 Exotic states of bouncing and walking droplets

The following paper has been published in Physics of Fluids **25**, 082002 (2013) and was written in collaboration with Jan Molacek, Dan Harris and John Bush. It reflects the experimental results obtained when characterizing the bouncing modes within the bouncing and walking regime, and is paired with theoretical predictions.

PHYSICS OF FLUIDS **25**, 082002 (2013)

Exotic states of bouncing and walking droplets

Øistein Wind-Willassen,[1] Jan Moláček,[2] Daniel M. Harris,[2] and John W. M. Bush[2,a)]
[1]*Department of Applied Mathematics and Computer Science, Technical University of Denmark, 2800 Kongens Lyngby, Denmark*
[2]*Department of Mathematics, Massachusetts Institute of Technology, 77 Massachusetts Avenue, Cambridge, Massachusetts 02139, USA*

(Received 20 March 2013; accepted 14 July 2013; published online 13 August 2013)

We present the results of an integrated experimental and theoretical investigation of droplets bouncing on a vibrating fluid bath. A comprehensive series of experiments provides the most detailed characterisation to date of the system's dependence on fluid properties, droplet size, and vibrational forcing. A number of new bouncing and walking states are reported, including complex periodic and aperiodic motions. Particular attention is given to the first characterisation of the different gaits arising within the walking regime. In addition to complex periodic walkers and limping droplets, we highlight a previously unreported mixed state, in which the droplet switches periodically between two distinct walking modes. Our experiments are complemented by a theoretical study based on our previous developments [J. Molacek and J. W. M. Bush, J. Fluid Mech. **727**, 582–611 (2013); **727**, 612–647 (2013)], which provide a basis for rationalising all observed bouncing and walking states. [http://dx.doi.org/10.1063/1.4817612]

I. INTRODUCTION

Drops bouncing on a vibrating fluid bath[1,2] have recently received considerable attention for two principal reasons. First, they represent a rich dynamical system, exhibiting many features of low-dimensional chaotic oscillators.[3–5] Second, in certain parameter regimes, the bouncers walk horizontally through resonant interaction with their wave field.[6–10] The resulting walkers represent the first known example of a macroscopic pilot-wave system,[11–13] and exhibit many features thought to be exclusive to the microscopic quantum realm,[14] including self-organising lattice structures,[15,16] single particle diffraction,[17] quantized orbits,[18] orbital level splitting,[19] tunneling effects,[20] and wave-like statistics in confined geometries.[21]

Consider a fluid of density ρ, kinematic viscosity ν, and surface tension σ in a horizontal bath of depth H driven by a vertical vibration of amplitude A and frequency $f = \omega/(2\pi)$. The effective gravity in the vibrating bath frame of reference is $g^*(t) = g + \gamma \sin(2\pi f t)$, where g is the gravitational acceleration and $\gamma = A\omega^2$. At low forcing acceleration, the fluid remains quiescent in the vibrating frame; however, above a critical acceleration amplitude γ_F corresponding to the Faraday threshold, the layer becomes unstable to a field of standing Faraday waves.[22,23] The waves are subharmonic, with half the frequency of the vibrational forcing, $\omega_F = \omega/2$, and with wavelength $\lambda_F = 2\pi/k_F$ prescribed by the standard surface wave dispersion relation:

$$\omega_F^2 = \tanh(k_F H)\left(gk_F + \frac{\sigma k_F^3}{\rho}\right). \tag{1}$$

In the experiments of interest, the vibrational forcing is less than the Faraday threshold, $\gamma < \gamma_F$; consequently, the interface would remain flat if not for the presence of a droplet.

a)bush@math.mit.edu

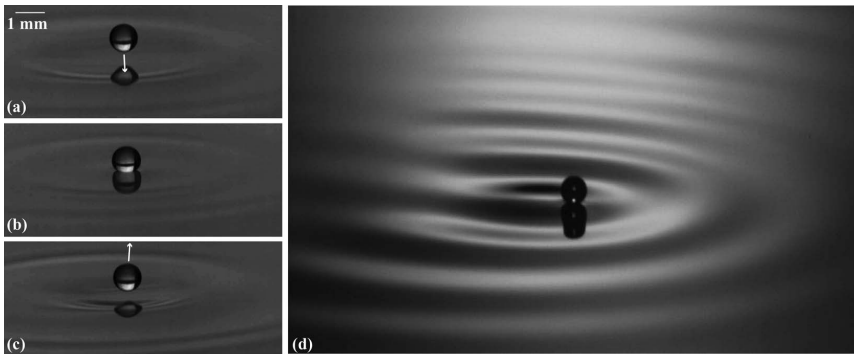

FIG. 1. Walking drop of 20 cS silicone oil of radius 0.48 mm (a) before, (b) during, and (c) after an impact with a bath of the same liquid vibrating at 70 Hz. (d) A walking drop and its associated wave field.

When a fluid drop is placed on a vibrating bath (Fig. 1), there are three basic outcomes: the droplet may either coalesce, bounce in place, or walk across the fluid surface.[1,7,9] For $\gamma < \gamma_B$, where γ_B is the bouncing threshold, the applied forcing is insufficient to levitate the drop, which then settles towards the bath. The intervening air layer thins until reaching a critical thickness at which Van der Waals forces between drop and bath initiate coalescence. For $\gamma > \gamma_B$, this air layer is sustained during impact, precluding coalescence and enabling a stable bouncing state. Beyond a critical forcing threshold, $\gamma > \gamma_w$, where γ_w is the walking threshold, the stationary bouncing state is destabilised by the underlying wave field, giving way to a dynamic state in which the drops walk across the fluid bath. The walking regime arises only for a limited range of drop sizes and forcing conditions.

Couder's group has characterised the behaviour of drops bouncing on a fluid bath in terms of the drop diameter $D = 2r_0$ and dimensionless forcing acceleration $\Gamma = \gamma/g$.[7–9] Protiere *et al.*[7] conducted experiments with a viscosity-frequency combination of 50 cS-50 Hz and summarised their results in a regime diagram illustrating the droplet behaviour in the D-Γ plane. For low forcing accelerations, simple bouncing arises: the drop hits the bath once every driving period. Increasing the acceleration generally leads to a period-doubled bouncing state. For relatively small and large drops, a period doubling cascade may follow, culminating in chaotic bouncing or walking. For the larger drops, an intermittent regime can arise in which the drop changes from one bouncing state to another in an irregular fashion. For drops within a limited size range, there is a critical $\Gamma_w = \gamma_w/g$ above which they walk along the surface of the bath. The walking regime was previously thought to be associated exclusively with a fully period doubled bouncing state; however, more complex walking modes will be highlighted herein. A similar regime diagram was obtained for a 20 cS-80 Hz combination, the system being characterised in terms of the same four characteristic states.[8,9] The theoretical rationale for the form of the regime diagrams was only recently developed,[10,13] and will be built upon herein.

Gilet and Bush[4] considered the motion of a drop on a vibrating soap film, and demonstrated that the film behaves like a linear spring with a spring constant proportional to the surface tension. They observed and rationalised a number of complex bouncing states, multiperiodicity (the existence of different bouncing states at identical system parameters), and period doubling transitions to chaos. Different bouncing states were denoted by (m, n), where m/f represents the period of the bouncing mode, during which the drop contacts the surface n times. The dynamics of interest here, of droplets bouncing on a vibrating fluid bath, are significantly complicated by the influence of the fluid bath's inertia.

Molacek and Bush[10] (henceforth MB1) examined droplets bouncing on a vibrating fluid bath, and detailed both experimentally and theoretically the dependence of the bouncing mode on the system parameters. They introduce the vibration number, $\Omega = 2\pi f\sqrt{\rho r_0^3/\sigma}$, the relative magnitude

of the forcing frequency, and the drop's natural oscillation frequency, and summarised their results in regime diagrams that indicate the droplet behaviour in the Ω-Γ plane. They demonstrate that droplets of a given size can bounce at the lowest forcing amplitude when $\Omega \approx 0.65$, that is, when the drop is forced at its natural frequency. They noted different bouncing states with the same periodicity, which they denote by $(m, n)^i$, where the integer superscript i increases with the state's mean mechanical energy, specifically, the drop's combined kinetic and gravitational potential energy. In addition to identifying a number of previously unreported bouncing states, MB1 developed a theoretical model that rationalises the observed dynamics. The vertical interaction between the bouncing drop and the liquid bath during drop contact was described using a logarithmic spring model, which built upon their model of drop impact on a rigid substrate.[24]

Molacek and Bush[13] (henceforth MB2) extended their theoretical model in order to capture the dynamics of walking droplets. Specifically, their logarithmic spring model was supplemented by consideration of the wave field of the bath, which may destabilise the stationary bouncing states. While they rationalised the limited extent of the walking regime, they did not characterise the dependence of the walking style on the system parameters. Their model successfully rationalised the experimentally reported transitions from bouncing to walking states, as well as the dependence of the walking speed on the system parameters. They also noted the coexistence of different walking states at the same system parameters, and highlighted the predominance of the $(2, 1)^1$ and $(2, 1)^2$ modes. Finally, they reported a number of exotic walking states, including chaotic walkers and "limping" drops that walk with unequal steps, the focus of the present study.

The goal of the current study is to extend our knowledge of the bouncing drop dynamics by presenting the most detailed regime diagrams to date. In addition to reporting a number of new exotic bouncing and walking states, we extend the predictions of our theoretical model[10,13] in order to rationalise our observations. In Sec. II, we describe our experimental set-up and present the experimentally obtained regime diagrams in which we identify the different walking and bouncing modes. We also examine the dependence of the walking speed on the bouncing mode. In Sec. III, we review our theoretical model and compare its predictions with our new experimental observations. Our results are summarised in Sec. IV.

II. EXPERIMENTS

In Figure 2, we present a schematic illustration of our experimental set-up. A circular fluid tray of diameter 76 mm and depth 16 mm is oscillated vertically in a sinusoidal manner with frequency f, amplitude A, and peak acceleration $\gamma = (2\pi f)^2 A$. The tray is vibrated by an industrial shaker mounted on a massive levelling platform, which rests beneath an optical table. The shaker is driven by a power amplifier controlled using a data acquisition system and custom software. We measure the acceleration using two piezoelectric accelerometers, and use a feedback loop to maintain a constant

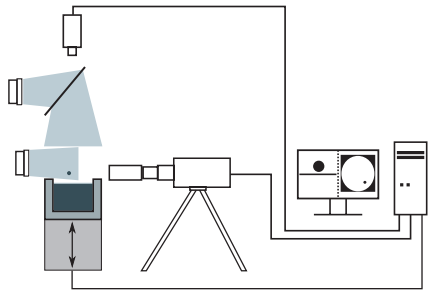

FIG. 2. Schematic illustration of the experimental set-up. The vibrating bath is illuminated by two LED lamps, and the drop motion recorded by two digital video cameras. The top view camera captures images at 17.5–20 frames per second, while the side view camera records at 4000 frames per second. The video processing is done on a computer.

vibration amplitude, corresponding to a tolerance of 0.01 g in vibrational acceleration amplitude. An air bearing carriage with a square cross section is mounted to a levelling platform to ensure that the vibratory motion lies strictly along a single vertical axis. The air bearing minimises lateral vibration introduced by the shaker, a technique developed for careful studies of vibrated granular layers.[25–27] A thin coupling rod connects the shaker to the slider bar of the air bearing.

We use two different silicone oils, the first with kinematic viscosity $\nu = 20$ cS, density $\rho = 949$ kg/m^3, and surface tension $\sigma = 20.6$ mN/m, and the second with $\nu = 50$ cS, $\rho = 965$ kg/m^3, and $\sigma = 20.8$ mN/m. We identify the Faraday threshold γ_F for each combination of experimental parameters by gradually increasing the acceleration amplitude γ until standing waves with frequency $f/2$ form at the free surface. The precise value of γ_F depends on the vibration frequency, the depth, and viscosity of the oil. The dimensionless Faraday threshold is denoted by $\Gamma_F = \gamma_F/g$.

Oil drops are created by rapidly extracting a submerged needle from the fluid bulk.[7] Of the droplets formed, we select those of radius r_0 between 0.20 mm and 0.51 mm. The undeformed drop radius r_0 is measured optically with a high-speed camera, recording at 4000 frames per second. The optical set-up results in a pixel density of 71–88 pixels per mm, leading to an uncertainty in drop radius of $\pm 1.5\%$. The horizontal motion of the drop is captured from above with a Machine Vision CCD camera and is tracked using particle-tracking software. We performed measurements for a single drop size by either increasing or decreasing the driving acceleration in a stepwise manner from some initial value of Γ, with typical step size $d\Gamma = 0.1\Gamma$. The entirety of the bouncing and walking regimes could thus be explored by varying γ between γ_B and γ_F.

Three different combinations of fluid viscosity and forcing frequency were investigated. A 20 cS silicone oil bath was forced at 70 and 80 Hz, and a 50 cS oil bath at 50 Hz. A full exploration of both walking and bouncing regions was conducted for the 20 cS-80 Hz combination, since this exhibited the richest behaviour. For the other two combinations, we focused on characterising the walking regimes. For each combination of oil viscosity and driving frequency, we present a regime diagram indicating the droplet bouncing behaviour in the Γ-Ω plane (Fig. 3). Spatiotemporal diagrams of selected bouncing and walking modes, deduced by transposing pixel-wide slices through the droplet's centerline obtained from successive frames, are presented in Figures 4–6. In Table I, a summary of the observed bouncing and walking modes is provided.

In the three regime diagrams reported in Fig. 3, the horizontal axis is the dimensionless forcing $\Gamma = \gamma/g$, and the vertical axis is the dimensionless vibration number Ω, a proxy for drop size. Individual markers correspond to experimental observations, with square and round markers denoting stationary bouncing and walking states, respectively. The colour of the marker denotes the observed bouncing or walking mode. We first describe the experimental results, and reserve the comparison with theoretical predictions for Sec. III.

A full exploration of both the bouncing and walking regimes for the 20 cS-80 Hz combination is shown in Fig. 3(a). For relatively weak forcing, $1.5 < \Gamma < 2.3$, the (2, 2) bouncing mode is dominant; however, a band of the (4, 4) mode (Fig. 4(a)) is also observed for vibration numbers $\Omega \lesssim 0.5$. As Γ is increased, additional $m = 4$ modes are observed. Specifically, the (4, 3) mode (Fig. 4(b)) arises in a region around $\Gamma \approx 2.6$ and $\Omega \approx 0.5$, and the (4, 2) mode (Fig. 4(c)) appears for almost all vibration numbers investigated, for $\Gamma > 3.3$, spanning both the bouncing and walking regimes. A region of (2, 1) bouncing modes extends from $\Gamma = 2.5$ up to Γ_F for vibration numbers between 0.6 and 1. This region crosses into the walking region, starting out in the low energy

TABLE I. The walking and bouncing modes observed for the three viscosity-frequency combinations examined. Modes in bold typeface are those for which an associated spatiotemporal diagram is included (see Figs. 4–6).

Fluid/frequency	Regime diagram	Bouncing and walking modes
20 cS-80 Hz	Fig. 3(a)	$(2, 1)^1$, $(2, 1)^2$, (2, 2), **(4, 2), (4, 3), (4, 4)**, chaotic; Fig. 4
50 cS-50 Hz	Fig. 3(b)	**(2, 1)^1**, **(2, 1)^2**, **chaotic**; Fig. 5
20 cS-70 Hz	Fig. 3(c)	**(2, 2)**, (4, 3), **(13, 10)**, $(2, 1)^1$, $(2, 1)^2$, **mixed mode**, chaotic; Fig. 6

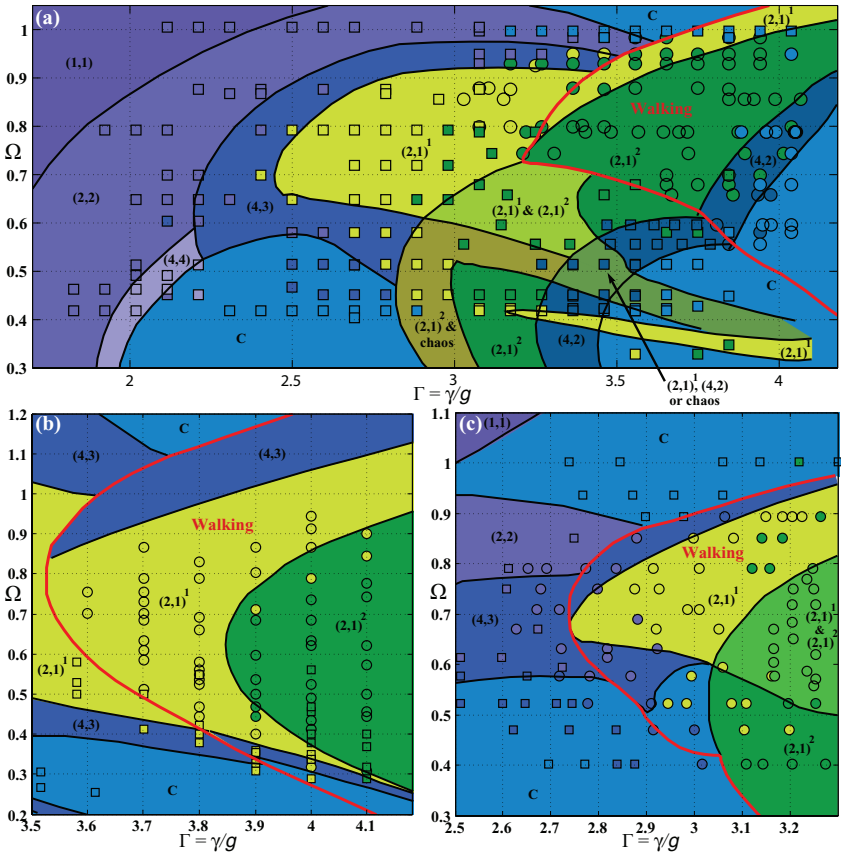

FIG. 3. Regime diagrams indicating the dependence of the droplet behaviour on the dimensionless driving acceleration, $\Gamma = \gamma/g$, and the vibration number, $\Omega = 2\pi f\sqrt{\rho r_0^3/\sigma}$. (a) The 20 cS-80 Hz combination, for which $\Gamma_F = 4.22 \pm 0.05$. (b) The 50 cS-50 Hz combination, for which $\Gamma_F = 4.23 \pm 0.05$. (c) The 20 cS-70 Hz combination, for which $\Gamma_F = 3.33 \pm 0.05$. Coloured areas correspond to theoretical predictions, the solid red line denoting the theoretically predicted walking threshold. Experimental data are presented as square or round markers, with square markers denoting stationary bouncing states, round markers walking states, and their colour indicating the associated mode.

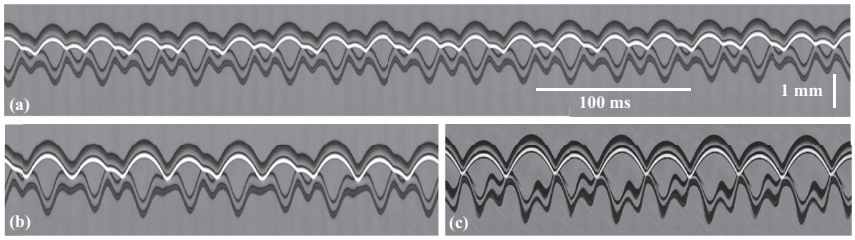

FIG. 4. Spatiotemporal diagrams of the bouncing modes observed for the 20 cS-80 Hz combination. (a) Bouncing mode (4, 4). $\Gamma = 2.3$, $\Omega = 0.45$. (b) Bouncing mode (4, 3). $\Gamma = 2.7$, $\Omega = 0.45$. (c) Bouncing mode (4, 2). $\Gamma = 3.5$, $\Omega = 0.42$.

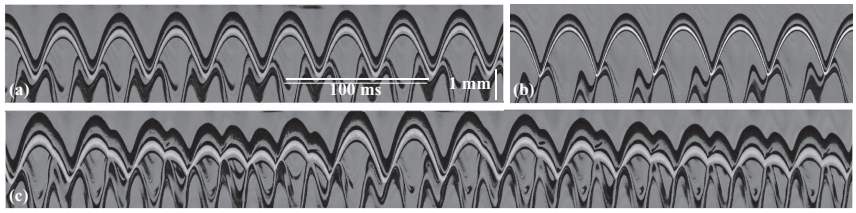

FIG. 5. Spatiotemporal diagrams of the modes observed for the 50 cS-50 Hz combination. (a) Walking mode $(2, 1)^1$. $\Gamma = 3.7$, $\Omega = 0.59$. (b) Walking mode $(2, 1)^2$. $\Gamma = 4.0$, $\Omega = 0.44$. (c) Chaotic bouncing with no apparent periodicity. $\Gamma = 4$, $\Omega = 0.94$.

$(2, 1)^1$ mode then transitioning into the high energy $(2, 1)^2$ mode as Γ is increased. The (2, 1) bouncing states also arise for smaller drops, $\Omega \approx 0.4$–0.5, along a band with Γ ranging from 2.9 to 3.3, at which a period doubling transition creates a (4, 2) mode that eventually gives way to a chaotic region.

Three distinct regions of complex or chaotic motion are observed. One exists for drops bouncing with $2.3 < \Gamma < 3$ and $\Omega \approx 0.4$. Another arises near $3.5 < \Gamma < \Gamma_F$, $0.4 < \Omega < 0.8$ and spans the bouncing and walking regimes. For larger drops ($\Omega \approx 1$) there is a region of complex or chaotic behaviour stretching from the bouncing ($\Gamma \approx 3.1$) into the walking regime, and up to the Faraday threshold. Generally, near the Faraday threshold, the walking is observed to be chaotic, with only a relatively small window of periodic walking, for $0.8 < \Omega < 1$, above which chaotic bouncing is observed. For $\Omega \approx 1$, we observed stationary chaotic bouncing drops that, when perturbed with a submerged needle, could be induced to transition into a stable (2, 1) walking mode.

The regime diagram deduced for the 50 cS-50 Hz combination is shown in Fig. 3(b). The observed modes were $(2, 1)^1$, $(2, 1)^2$, and chaotic bouncing, the form of which are presented in Fig. 5. Walking occurs only in the $(2, 1)^1$ and $(2, 1)^2$ modes, the horizontal drop speed being typically 2-3 times larger in the former than in the latter. The $(2, 1)^1$ mode (Fig. 5(a)) has a longer contact time than the higher energy $(2, 1)^2$ mode (Fig. 5(b)), for which a much more rapid shift in momentum occurs during impact. The impact phase relative to the vibrating bath is also different, as is the walking speed, which is approximately 4 times higher for the $(2, 1)^1$ mode. The drop is generally in the $(2, 1)^1$ mode near the walking threshold, but transitions to the $(2, 1)^2$ mode as Γ is increased, remaining in this state until the Faraday threshold is reached. Chaotic bouncing is observed for lower forcing and drop size (Fig. 5(c)).

The regime diagram for the 20 cS-70 Hz combination is shown in Fig. 3(c) and includes a number of exotic bouncing and walking modes. Outside the walking region, three bouncing modes are observed. For large ($\Omega \approx 1$) and small ($\Omega \approx 0.4$) vibration numbers, chaotic or highly complex bouncing states are evident. Fig. 6(a) shows a spatiotemporal evolution of a highly complex (13, 10) mode. For intermediate Ω, (4, 3) and (2, 2) bouncing modes arise, the former being observed for drops with $\Omega \approx 0.4$–0.6, and the latter for $\Omega \approx 0.6$–0.8. Fig. 6(b) shows the spatiotemporal diagram of a drop in the (2, 2) mode. We refer to these as limping drops, owing to their unequal step sizes. The (4, 3) and (2, 2) modes stretch into the walking region, where the (2, 1) modes are dominant. Once again, the $(2, 1)^2$ mode is generally observed at lower Ω than the $(2, 1)^1$ mode.

Of particular interest is a region of "mixed states" for $\Gamma > 3.1$ and $0.55 < \Omega < 0.8$. Here the drops alternate between the low and high energy (2, 1) modes, as shown in Fig. 6(c), where the evolution is from $(2, 1)^1$ to $(2, 1)^2$ to $(2, 1)^1$ to $(2, 1)^2$. While the heights of the jumps are roughly equal, the phase of impact shifts rapidly. In Fig. 7(a), the horizontal trajectory of a drop in the mixed state is shown. The shading of the trajectory reflects its local horizontal speed which fluctuates by a factor of 4 as it switches between the fast $(2, 1)^1$ mode and the slow $(2, 1)^2$ mode. Fig. 7(b) shows the velocity of the mixed mode as a function of arc-length. The variation of the velocity occurs over a distance of approximately one Faraday wavelength, resulting in a highly peaked power spectrum (Fig. 7(c)). We note that the mixed mode is generally quite robust; however, by perturbing the drop with the meniscus of a submerged pin or through spontaneous interaction with a boundary,

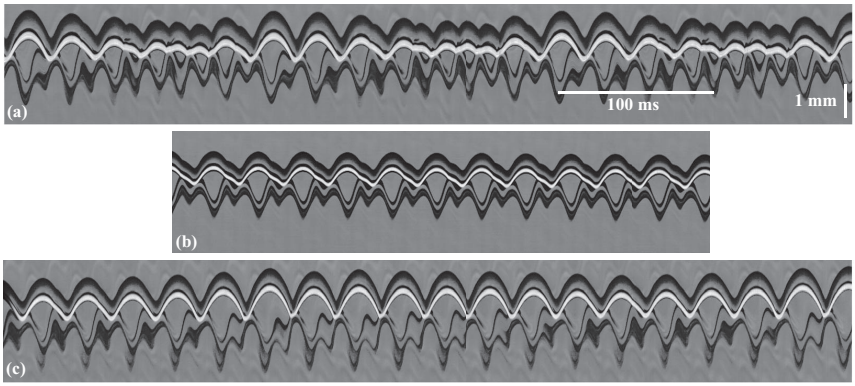

FIG. 6. Spatiotemporal diagrams of the modes observed for the 20 cS-70 Hz combination. (a) The exotic bouncing mode (13, 10), highly complex periodic motion. $\Gamma = 3.3$, $\Omega = 0.97$. (b) The limping drop, a (2, 2) walking mode. $\Gamma = 2$, $\Omega = 0.42$. (c) The mixed walking state, shown here evolving from $(2, 1)^1 \rightarrow (2, 1)^2 \rightarrow (2, 1)^1 \rightarrow (2, 1)^2$. $\Gamma = 3.4$, $\Omega = 0.72$.

it can be destabilised, causing the drop to shift into either the $(2, 1)^1$ or the $(2, 1)^2$ walking modes. Fig. 7(d) shows the trajectory of a mode switcher settling into the high energy $(2, 1)^2$ mode after being perturbed by an approach to the boundary at nearly normal incidence. We note that we might alternatively have denoted the mixed state by a purely periodic mode, (24,12); however, we find it

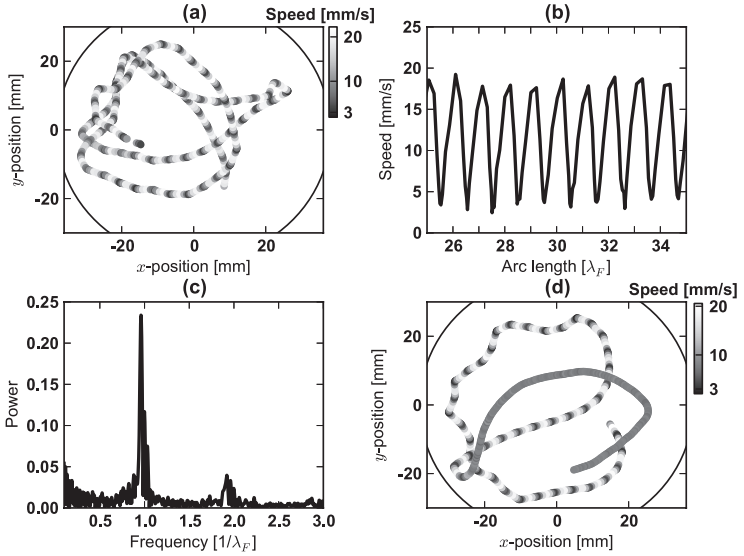

FIG. 7. Mixed state walkers observed with the 20 cS-70 Hz combination. $\Gamma = 3.4$, $\Omega = 0.72$. (a) The trajectory for a drop in the mixed state, shaded according to the speed. The circular bath domain is indicated. (b) The observed variation of walking speed with arc-length, as normalised by the Faraday wavelength. (c) A Fourier power spectrum of the normalised velocity fluctuations, which indicates that the mode-switching arises periodically, after the droplet has walked a distance of approximately $0.95\lambda_F$. (d) Trajectory of a mixed mode, shaded according to speed, that destabilises into a $(2, 1)^2$ walker after collision with the boundary near $(x, y) = (-25, -20)$ mm.

useful to distinguish between the two phases of its motion ($(2, 1)^1$ and $(2, 1)^2$), in which its speed is markedly different.

III. THEORETICAL PREDICTIONS

In order to obtain theoretical predictions for the dependence of the bouncing behaviour on the system parameters, we adopted the model presented in MB1 and MB2. There, it was shown that the vertical drop motion is governed by

$$\begin{aligned} -mg^*(t) &= m\ddot{z} \quad \text{in free flight } (\mathcal{Z} \geq 0 \text{ or } F_N \leq 0)\,, \\ -mg^*(t) &= \left(1 + \frac{c_3}{\ln^2 |\frac{c_1 r_0}{\mathcal{Z}}|}\right) m\ddot{z} + \frac{4}{3}\frac{\pi \mu r_0 c_2(\nu)}{\ln |\frac{c_1 r_0}{\mathcal{Z}}|}\dot{\mathcal{Z}} + \frac{2\pi\sigma\mathcal{Z}}{\ln |\frac{c_1 r_0}{\mathcal{Z}}|} \quad \text{during contact}\,, \end{aligned} \tag{2}$$

where m is the drop mass, z is its center of mass, and $\mathcal{Z} = z - h$ is the height of the drop above the bath surface. During free flight, the drop responds only to gravity. During impact, $F_N(t) = m\ddot{z} + mg^*(t)$ is the normal component of the reaction force acting on the drop. The constants used here, $c_1 = 2$, $c_3 = 1.4$, $c_2 = 12.5$ for 20 cS oil and $c_2 = 7.5$ for 50 cS oil, were deduced in MB1 by matching with experimental measurements of the normal and tangential coefficients of restitution. To consider one-dimensional horizontal drop motion, we write $h = h(x, t)$ as the total height of the standing waves in the bath frame of reference. $h(x, t)$ can be expressed as the sum of contributions from all previous impacts:

$$h(x, t) = \sum_{n=1}^{N} h_0(x, x_n, t, t_n). \tag{3}$$

The contribution $h_0(x, x_n, t, t_n)$, resulting from a single drop impact at $(x, t) = (x_n, t_n)$, can be approximated, in the long-time limit, by a standing wave decaying exponentially in time with a spatial profile prescribed by a zeroth order Bessel function of the first kind, $J_0(x)$:

$$\begin{aligned} h_0(x, x_n, t, t_n) \approx J_0\left(k_F(x - x_n)\right) \sqrt{\frac{2}{\pi}} \frac{k_F r_0}{3k_F^2 r_0^2 + \mathcal{B}o} \frac{r_0 k_F^2 \mu_{eff}^{1/2}}{\sigma} \frac{\cos(\pi f t)}{\sqrt{t - t_n}} \\ \times \exp\left\{(\Gamma/\Gamma_F - 1)\frac{t - t_n}{T_d}\right\} \int F_N(t') \sin\left(\pi f t'\right) \mathrm{d}t'\,. \end{aligned} \tag{4}$$

Here, $\mathcal{B}o = \rho g r_0^2/\sigma$ is the Bond number, and T_d is the characteristic decay time of the unforced waves, which depends on the fluid viscosity and the critical wavenumber. μ_{eff} is a phenomenological viscosity required to ensure that the decay rate of the waves matches that in a fully analytical model (MB2, Appendix A.1). The integral of the reaction force, $F_N(t)$, is carried out over the duration of contact.

In order to increase computational speed, the number of previous impacts stored is kept to a manageable size by discarding those whose standing wave amplitude has decayed sufficiently (below 0.1% of its initial value). Since the contact takes place over a finite length of time, x_n and t_n are taken as the weighted averages of x and t over the contact time t_c, defined as the interval during which the vertical reaction force $F_N(t)$ on the drop is positive:

$$x_n = \frac{\int_{t_c} F_N(t')x(t')\mathrm{d}t'}{\int_{t_c} F_N(t')\mathrm{d}t'}, \quad t_n = \frac{\int_{t_c} F_N(t')t'\mathrm{d}t'}{\int_{t_c} F_N(t')\mathrm{d}t'}. \tag{5}$$

The horizontal dynamics is governed by

$$m\ddot{x} + D(t)\dot{x} = -\frac{\partial h(x, t)}{\partial x} \cdot F_N(t), \tag{6}$$

where

$$D(t) = 0.17\frac{\sqrt{\rho r_0}}{\sigma} F_N(t) + 6\pi r_0 \mu_a \left(1 + \frac{g r_0}{12} v_a f\right) \tag{7}$$

is the total instantaneous drag coefficient. The subscript a denotes air. The first term represents the momentum drag induced during impact and the second term represents the aerodynamic drag induced during flight. The term on the right-hand side of Eq. (6) is the propulsive wave force applied during contact, which is well approximated by the tangential component of the total reaction force.

The system of Eqs. (2)–(6) was solved numerically, with time step $0.05\sqrt{\rho r_0^3/\sigma}$ during contact, the duration of which was typically at least $4\sqrt{\rho r_0^3/\sigma}$. We followed a procedure akin to that adopted to obtain the experimental data reported in Fig. 3; specifically, we scan a wide range of Ω ($0.2 \leq \Omega \leq 1.2$), with increments of $d\Omega = 0.005$. For each Ω value, we start at a value of Γ close to the Faraday threshold, specifically $\Gamma = 0.99\Gamma_F$, then decrease Γ in small increments until reaching some pre-defined lower limit. We shall refer to one such sweep of Γ as a *run*. The bath is taken to be initially quiescent, $h(x, 0) = 0$. We performed several runs, starting each with different initial conditions on the drop position $z(0)$ and speed $\dot{z}(0)$, so as to increase the likelihood of discovering all the possible bouncing modes in case of the coexistence of multiple modes. Usually, this meant setting $z(0) = 0$ and varying $\dot{z}(0)$ between -0.3 and 0.3.

For relatively large drops close to the Faraday threshold, as in our experiments, both walking and bouncing states may arise at identical system parameters. To ensure resolution of the walking solution, the initial horizontal speed was set to a value higher than the equilibrium speed. Then, for each run, we slowly decreased Γ in steps $d\Gamma = 0.001\Gamma_F$, at each step waiting for the walking speed to converge, specifically until the difference between the average walking speed at successive impacts drops below 0.1%:

$$0.999 < \left| \frac{\bar{v}_t}{\bar{v}} \right| < 1.001, \tag{8}$$

where $\bar{v}$ and $\bar{v}_t$ are the average horizontal drop speed up to the time of the penultimate and last impacts, respectively.

At each Γ value, we recorded the period of vertical motion and number of contacts per period, which yielded the (m, n) mode number. We also recorded the average contact time $\bar{T}_C$, the total contact time per period of vertical motion divided by the number of contacts n. This allowed us to differentiate between different energy levels, as the high energy modes had $\bar{T}_C < 5\sqrt{\rho r_0^3/\sigma}$ (typically, $\bar{T}_C \approx 3.5\sqrt{\rho r_0^3/\sigma}$), while the low energy modes had $\bar{T}_C > 5\sqrt{\rho r_0^3/\sigma}$ (typically, $\bar{T}_C \approx 8\sqrt{\rho r_0^3/\sigma}$). When the forcing is decreased below a critical value Γ_W, the walking speed drops to 0. The equations of motion can then be simplified considerably, as (6) is identically 0, and $J_0(k_C(x - x_n)) = 1$ in (4). Assimilation of the data obtained by this procedure yielded our theoretical regime diagrams (Fig. 3). Numerically computed vertical bouncing modes with corresponding surface displacements are provided in MB1 (Figures 16–18) and MB2 (Figure 16).

The solid coloured regions of Figs. 3(a)–3(c) indicate the theoretically predicted bouncing modes. The red line indicates the predicted walking threshold. For the 20 cS-80 Hz combination (Fig. 3(a)) several modes are found to exist where predicted, including the observed (2, 1), (2, 2), (4, 4), (4, 2), and chaotic modes. The experimental walking threshold for large and small vibration numbers ($\Omega < 0.7$ and $\Omega > 0.9$) coincides with the theoretical predictions; however, for drops of intermediate size, the agreement is less convincing. The (4, 3) bouncing mode is experimentally observed for smaller drop sizes than predicted, and the experimental $(2, 1)^1$ bouncing region extends further into the theoretical (4, 3), $(2, 1)^2$, and chaotic regions than predicted. The model does capture the observed $(2, 1)^1$-branch cutting across several other regions near $\Gamma \approx 3$–4 and $\Omega < 0.6$.

For the 50 cS-50 Hz combination (Fig. 3(b)), the observed and predicted $(2, 1)^1$ and $(2, 1)^2$ modes coincide convincingly, and the theoretical and experimental walking thresholds also match. Furthermore, chaotic bouncers were observed inside the theoretically predicted chaotic region. The (4, 3) walking regime was not observed experimentally, but might have been had larger drops been examined.

For the 20 cS-70 Hz regime diagram (Fig. 3(c)), the observed chaotic region for large drops ($\Omega \approx 1$) coincides with that predicted. For smaller drops ($\Omega \approx 0.4$–0.6), the observed (4, 3) mode

is offset relative to that predicted, as was the case in the experiments at 20 cS-80 Hz (Fig. 3(a)). The (2, 2) bouncing mode is also observed at slightly lower vibration numbers than predicted. The observed high and low energy (2, 1) modes do not coincide precisely with the theory within the walking region, but the walking threshold is generally well-predicted. The mixed mode region found experimentally corresponds closely to the theoretically predicted region of coexistence of the $(2, 1)^1$ and $(2, 1)^2$ modes. We note that a true mixed mode, characterised by a stable periodic shift between the low and high energy (2, 1) modes, has not yet been observed theoretically.

Finally, we note that in our experiments the threshold between bouncing states generally depends on whether it was approached from above or below. Specifically, by increasing and decreasing Γ across a regime boundary, the Γ threshold between states has a characteristic uncertainty of $\Delta\Gamma \approx 0.1$. This hysteresis, which may reflect the existence of prolonged transient behaviour, provides some rationale for the relatively small discrepancy between theory and experiment. We note that significantly less hysteresis was apparent in the simulations, which could be simply extended beyond any transient behaviour.

IV. CONCLUSION

We have conducted a combined experimental and theoretical study of drops bouncing on a vibrating fluid bath, and focused on the parameter regime of interest to workers in hydrodynamic quantum analogs. By comparing our experimental results with the theory developed in MB1 and MB2, we have extended the current knowledge of the bouncing droplet system. We have enumerated the myriad styles in which drops can bounce and walk, and presented, in Fig. 3, the most detailed experimental and theoretical regime diagrams to date. Particular attention has been given to elucidating the rich and varied dynamics within the walking regime, an understanding of which will assist in rationalising the quantum-like behaviour of walking drops. Finally, we have highlighted a mixed state, in which the walking drop shifts between two distinct modes, a state that may prove valuable in expanding the range of hydrodynamic quantum analog systems.

ACKNOWLEDGMENTS

The authors gratefully acknowledge the financial support of the National Science Foundation (NSF) through Grant No. CBET-0966452. Ø.W.-W. thanks The Danish National Advanced Technology Foundation for financial support through the NanoPlast project. D.M.H. thanks the NSF Graduate Research Fellowship Program for financial support.

[1] J. Walker, "Drops of liquid can be made to float on the liquid. What enables them to do so?," Amateur Scientist, Sci. Am. **238**, 151–158 (1978).
[2] Y. Couder, E. Fort, C.-H. Gautier, and A. Boudaoud, "From bouncing to floating: Noncoalescence of drops on a fluid bath," Phys. Rev. Lett. **94**, 177801 (2005).
[3] T. Gilet, D. Terwagne, N. Vandewalle, and S. Dorbolo, "Dynamics of a bouncing droplet onto a vertically vibrated interface," Phys. Rev. Lett. **100**, 167802 (2008).
[4] T. Gilet and J. W. M. Bush, "The fluid trampoline: Droplets bouncing on a soap film," J. Fluid Mech. **625**, 167–203 (2009).
[5] T. Gilet and J. W. M. Bush, "Chaotic bouncing of a droplet on a soap film," Phys. Rev. Lett. **102**, 014501-1–014501-4 (2009).
[6] Y. Couder, S. Protiere, E. Fort, and A. Boudaoud, "Dynamical phenomena: Walking and orbiting droplets," Nature **437**, 208 (2005).
[7] S. Protiere, A. Boudaoud, and Y. Couder, "Particle-wave association on a fluid interface," J. Fluid Mech. **554**, 85–108 (2006).
[8] A. Eddi, D. Terwagne, E. Fort, and Y. Couder, "Wave propelled ratchets and drifting rafts," Europhys. Lett. **82**, 44001 (2008).
[9] A. Eddi, E. Sultan, J. Moukhtar, E. Fort, M. Rossi, and Y. Couder, "Information stored in Faraday waves: the origin of a path memory," J. Fluid Mech. **674**, 433 (2011).
[10] J. Molacek and J. W. M. Bush, "Drops bouncing on a vibrating bath," J. Fluid Mech. **727**, 582–611 (2013).
[11] L. de Broglie, "Interpretation of quantum mechanics by the double solution theory," Ann. Fond. Louis Broglie **12**(4), 1–23 (1987).
[12] Y. Couder and E. Fort, "Probabilities and trajectories in a classical wave-particle duality," J. Phys.: Conf. Ser. **361**, 012001 (2012).

[13] J. Molacek and J. W. M. Bush, "Drops walking on a vibrating bath: towards a hydrodynamic pilot-wave theory," J. Fluid Mech. **727**, 612–647 (2013).
[14] J. W. M. Bush, "Quantum mechanics writ large," Proc. Natl. Acad. Sci. U.S.A. **107**(41), 17455–17456 (2010).
[15] A. Eddi, A. Decelle, E. Fort, and Y. Couder, "Archimedean lattices in the bound states of wave interacting particles," Europhys. Lett. **87**, 56002 (2009).
[16] A. Eddi, A. Boudaoud, and Y. Couder, "Oscillating instability in bouncing droplet crystals," Europhys. Lett. **94**, 20004 (2011).
[17] Y. Couder and E. Fort, "Single-particle diffraction and interference at a macroscopic scale," Phys. Rev. Lett. **97**, 154101 (2006).
[18] E. Fort, A. Eddi, A. Boudaoud, J. Moukhtar, and Y. Couder, "Path-memory induced quantization of classical orbits," Proc. Natl. Acad. Sci. U.S.A. **107**(41), 17515–17520 (2010).
[19] A. Eddi, J. Moukhtar, S. Perrard, E. Fort, and Y. Couder, "Level splitting at macroscopic scale," Phys. Rev. Lett. **108**, 264503 (2012).
[20] A. Eddi, E. Fort, F. Moisy, and Y. Couder, "Unpredictable tunneling of a classical wave-particle association," Phys. Rev. Lett. **102**, 240401 (2009).
[21] D. M. Harris, J. Moukhtar, E. Fort, Y. Couder, and J. W. M. Bush, "Wavelike statistics from pilot-wave dynamics in a circular corral," Phys. Rev. E **88**, 011001 (2013).
[22] S. Douady, "Experimental study of the Faraday instability," J. Fluid Mech. **221**, 383–409 (1990).
[23] T. B. Benjamin and F. Ursell, "The stability of the plane free surface of a liquid in vertical periodic motion," Proc. R. Soc. London, Ser. A **225**(1163), 505–515 (1954).
[24] J. Moláček and J. W. M. Bush, "A quasi-static model of drop impact," Phys. Fluids **24**, 127103-1–127103-16 (2012).
[25] P. M. Reis, R. A. Ingale, and M. D. Shattuck, "Forcing independent velocity distributions in an experimental granular fluid," Phys. Rev. E **75**, 051311 (2007).
[26] D. I. Goldman, "Pattern formation and fluidization in vibrated granular layers, and grain dynamics and jamming in a water fluidized bed," Ph.D. thesis, University of Texas at Austin (2002).
[27] J. R. de Bruyn, B. C. Lewis, M. D. Shattuck, and H. L. Swinney, "Spiral patterns in oscillated granular layers," Phys. Rev. E **63**, 041305 (2001).

A.2 A finite-element method model for droplets moving down a hydrophobic surface

The following paper has been submitted (November 2013) to the European Physical Journal E, and is the result of a study where droplets interacting with a hydrophobic surface was modeled through a Finite Element Method.

EPJ manuscript No.
(will be inserted by the editor)

A finite-element method model for droplets moving down a hydrophobic surface

Øistein Wind-Willassen and Mads Peter Sørensen

Department of Applied Mathematics and Computer Science, Technical University of Denmark, 2800 Kongens Lyngby, Denmark

Received: date / Revised version: date

Abstract. We set up a 2D computational Finite-Element Method (FEM) model describing the initial descent of a droplet down an inclined hydrophobic substrate. We solve the full Navier-Stokes equations inside the drop domain, and use the Arbitrary Lagrangian-Eulerian method to keep track of the droplet surface. The contact angle is included by using the Frennet-Serret equations. We investigate the behaviour of the drop velocity as a function of the slip length and compare with experimental results. Furthermore, we quantify the energy associated with centre of mass translation and internal fluid motion. The model predicts trajectories for tracer particles deposited inside the drop, and satisfactorily describes the sliding motion of steadily accelerating droplets. The model can be used for determining a characteristic slip parameter, associated with slip lengths and drag reduction for hydrophobic surfaces.

PACS. 47.11.Fg Finite element methods – 47.55.D- Drops and bubbles – 47.55.np Contact lines

1 Introduction

Structured hydrophobic surfaces are widely seen in nature and lead to phenomena such as colour effects and self-cleaning properties[1]. Such surfaces have now become manufacturable by a range of processes, increasing the necessity for understanding the relating physics and chemistry. One such understanding concerns the dynamic behaviour of droplets on an inclined hydrophobic surface. It is important to understand the flow inside the droplet as it slides down the plane since this has an effect on the self-cleaning properties of the surface. Depending on the dynamic viscosity (η) and liquid-air surface tension (σ) of the liquid, the drop can follow different regimes. Viscous drops, $\eta > \sqrt{\sigma\rho\kappa^{-1}\alpha}$, where ρ is the density and $\kappa^{-1} = \sqrt{\sigma/(\rho g)}$ is the capillary length, follow the Mahadevan - Pomeau model[2], and exhibit a solid-like rotation. This regime lasts until surface tension no longer dominates the inertial forces, i.e. when the capillary number is above unity, $Ca = \eta V/\sigma > 1$. Here, V is the velocity of the drop. For less viscous liquid drops, experiments have shown the initial descent to have a constant acceleration, $v(t) \sim t\sin(\alpha)$, where α is the small incline of the surface[3], indicating a pure sliding motion. This regime persists until air drag and the viscous friction between solid and liquid balances the gravitational pull, resulting in a back-bending drop[4]. Other applications of structured surfaces have been considered, e.g., Patankar[5] considers the use of patterned surfaces as a driving device for lab-on-a-chip systems. By oscillating an increasingly textured surface vertically, drop motion can be induced[6, 7].

The large slip and associated large velocities seen on hydrophobic surfaces occur when the drop resides on top of the created structures. Cassie [8] and Wenzel [9] gave the first descriptions of the apparent contact angle of a drop residing either suspended or submerged on a structured surface. The models describe the static droplet, and give rise to an apparent contact angle. However, there are a range of stable contact angles, owing to the hysteretic nature of the problem[10]. Among others, Patankar [5] has conducted experiments to characterise the hysteresis on different structured surfaces. They determined that the models by Cassie and Wenzel do not fully explain the hysteresis effect. Furthermore, there is a challenge regarding the moving contact line. Pomeau[11] proposes the effect of evaporation/condensation near the moving contact line, which is also in experimental agreement. However, in order to have slip on a surface, the Navier-slip condition can be applied. This boundary condition removes the stress singularity arising at the triple point in the case of a no-slip condition[12–14]. A review on general slip conditions is given by Rothstein[15], in which it is concluded that for situations of larger length-scale than the microscopic level, the Navier slip-condition is well-suited. A recent study by Srinivasan et al.[16] on multi-scale structured spray-coated surfaces resulted in slip lengths on the scale of 100 μm, indicating that, for small-scale flows, the no-slip boundary condition should probably be replaced.

The Finite Element Method (FEM) as a numerical framework has been used to study both the statics and dynamics of drops. This numerical method is also denoted as a sharp interface method, since the boundary separating different phases is well-defined. The static shape

of a pendant drop hanging from a surface, and a static drop residing on a surface with a given static contact angle was examined by Saksono & Peric[17]. Their numerical solution matched well against a parameterization of the Young-Laplace equation. Dynamic effects, such as the evolution of the contact angle of droplets initially displaced[18] and oscillating droplets[19] have also been studied through FEM, and Brackbill et al. [20] and Walkley et al.[21] concludes that the method is in general suitable to describe free surface flows. Other numerical methods have been implemented, e.g. a Lattice-Boltzmann model[22], which builds upon a diffuse interface, which does not explicitly solve the governing equations for the fluid flow[23]. Furthermore, simulations of a droplet climbing an inclined plane were done by Das & Das[24], where the gradients needed to sustain climbing at different inclination angles were examined. Thampi et al.[25] recently applied a Lattice-Boltzmann model in order to study drops moving down an inclined plane. They specifically noted the remarkable dependence of the rotating motion in the drop on the isoperimetric quotient $q = \frac{4\pi \times Area}{Perimeter^2}$, a measure of how close to a circle the drop is. The closer q is to unity, the more rotation is observed inside the drop. They also noted the increasing rolling motion as the viscosity ratio between liquid and surrounding gas increases. Furthermore, they introduced a clever way to determine the amount of rotation inside the drop, based on a triple decomposition of the velocity gradient, enabling them to distinguish between the sliding, shearing and rolling motion of the drop. However, they did not compare to experimental results, but considered the steady state of the model and not the initial descent of the droplets, this being the scope of the present study. A similarity for all the mentioned numerical studies is the use of a 2-dimensional drop to study the dynamics and statics. As is the case in our study, it is believed, that the result is generalizable to the 3-dimensional case.

The goal of the current study is to extend the knowledge of a drop moving down an inclined superhydrophobic plane by presenting a finite-element model that describes this situation. We focus on the initial steady accelerating descent of the droplets. The numerical model and the numerical scheme used to obtain the simulations are presented, and we show how the slip coefficient can be used as a characterising parameter for a superhydrophobic surface by comparing with experimental data found in the literature. We furthermore compare the results from the model with known rolling and sliding examples to highlight the rotating motion inside the drop, and also determine the energies related to translation and internal fluid flow. Finally, interesting results for specific particle trajectories inside the drop are presented.

2 Setting up the model

The chosen geometry is shown schematically in Figure 1, where the computational domain is Ω. The boundary Γ of the drop is divided into two parts; the free surface Γ_{free} and the part in contact with the solid Γ_{solid}. The union

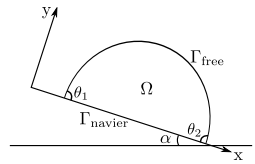

Fig. 1. The drop on an inclined plane. The inclination angle is α. Ω is the computational domain, Γ_{free} and Γ_{solid} are the free and solid-liquid boundaries. The contact angles at the left and right side are θ_1 and θ_2. All these quantities are allowed to vary in time. The size of the drop is D. We model gravity as a body force in the x-direction.

of these two is the entire boundary, $\Gamma = \Gamma_{\text{free}} \bigcup \Gamma_{\text{solid}}$. The boundaries do not overlap, so $\Gamma_{\text{free}} \bigcap \Gamma_{\text{solid}} = \emptyset$. The contact angles at the left and right side of the drop are denoted θ_1 and θ_2 respectively. Note that in general $\theta_1 \neq \theta_2$. The size (diameter) of the drop is D. The domain and the boundaries are allowed to change with time as the system evolves. The chosen coordinate system allows for implementation of a spatially varying prescribed contact angle.

2.1 Governing equations

The Navier-Stokes equation and incompressibility condition is

$$\rho \left(\partial_t \mathbf{u} + (\mathbf{u} \cdot \nabla)\, \mathbf{u}\right) = \nabla \cdot \mathbf{S} + \mathbf{f}. \tag{1}$$

$$\nabla \cdot \mathbf{u} = 0. \tag{2}$$

$\mathbf{S}(\mathbf{u}, p)$ is the Cauchy stress tensor which is a function of the velocity $\mathbf{u} = \mathbf{u}\,(x, y, t)$ and the pressure $p = p\,(x, y, t)$,

$$S(\mathbf{u}, p)_{i,j} = 2\eta D(\mathbf{u})_{i,j} - p\delta_{i,j}, \qquad i, j = 1, 2,$$

where

$$D(\mathbf{u})_{i,j} = \frac{1}{2}\left(\frac{\partial u_i}{\partial x_j} + \frac{\partial u_j}{\partial x_i}\right), \qquad i, j = 1, 2.$$

In Eq. 1, $\mathbf{f}$ is the gravitational pull, modeled as a volume force in the x-direction,

$$\mathbf{f} = \rho g \sin(\alpha)\mathbf{e_x} - \rho g \cos(\alpha)\mathbf{e_y}, \tag{3}$$

where α is the inclination angle, and $\mathbf{e}_x$ and $\mathbf{e}_y$ are unit vectors in the x and y-direction, respectively. The boundary conditions on Γ_{free} are the following

$$\begin{aligned} \mathbf{n}_F \cdot \mathbf{u} &= \mathbf{n}_F \cdot \mathbf{w} \\ \mathbf{n}_F \cdot \mathbf{S} \cdot \mathbf{n}_F &= \sigma \nabla_s \cdot \mathbf{n}_F \\ \mathbf{n}_F \cdot \mathbf{S} \cdot \mathbf{t}_F &= 0. \end{aligned} \tag{4}$$

Here $\mathbf{n}_F$ and $\mathbf{t}_F$ are the normal and tangent vector of the free surface, and ∇_s is the surface divergence operator, sometimes written as $\nabla_s = \nabla - \mathbf{n}\frac{\partial}{\partial n}$, i.e. it is the divergence operator restricted to the surface Γ_{free}. This means

that $\nabla_s \cdot \mathbf{n}_F = \kappa$, where κ is the curvature of the surface. The first boundary condition equates the normal velocity of the fluid to the normal velocity of the interface, $\mathbf{w}$. The second condition is the Young-Laplace equation on the free surface. The assumption is that there are no Marangoni flows, which is stated in the last condition. On the solid-liquid boundary Γ_{solid}, the conditions are

$$\begin{aligned} \mathbf{n}_S \cdot \mathbf{u} &= 0 \\ \mathbf{t}_S \cdot \mathbf{u} - \beta \left(\mathbf{n}_S \cdot \mathbf{S} \cdot \mathbf{t}_S \right) &= 0. \end{aligned} \tag{5}$$

The first condition is a no-penetration condition through the solid. The second is the Navier slip condition which sets the tangential velocity of the fluid proportional to the shear stress in the fluid at the boundary. The factor β is the slip-length which determines the amount the fluid is slipping at this boundary. The above constitutes a complete model for modelling fluid slipping on a plane surface with some defined free surface. It can also describe a freely oscillating droplet by setting $\Gamma_{\text{solid}} = \emptyset$.

2.2 The weak formulation

In the following, in order to implement the model in a computer program and solve it through FEM it is necessary to put it into weak formulation. This is done by choosing suitable test functions $\mathbf{v}$ and q, multiplying these with equations 1 and 2 and integrating over the computational domain[18,26,27],

$$\int_\Omega Re \partial_t \mathbf{u} \cdot \mathbf{v} d\Omega + \int_\Omega Re \left(\mathbf{u} \cdot \nabla \right) \mathbf{u} \cdot \mathbf{v} d\Omega \tag{6}$$

$$= \int_\Omega \left(\nabla \cdot \mathbf{S}(\mathbf{u}, p) \right) \cdot \mathbf{v} d\Omega + \int_\Omega \mathbf{f} \cdot \mathbf{v} d\Omega. \tag{7}$$

$$\int_\Omega \left(\nabla \cdot \mathbf{u} \right) q d\Omega = 0. \tag{8}$$

To avoid dealing with second derivatives of $\mathbf{u}$, the integral with the stress tensor is considered. It is first noted that the following holds

$$\left(\nabla \cdot \mathbf{S} \right) \cdot \mathbf{v} = \nabla \cdot \left(\mathbf{S} \cdot \mathbf{v} \right) - \mathbf{S} : \left(\nabla \mathbf{v} \right),$$

where $\mathbf{A} : \mathbf{B} = tr\left(\mathbf{A}^T \mathbf{B} \right)$ is the Frobenious inner product, or the tensor double dot product. Using this along with the divergence theorem the stress tensor integral is written as

$$\int_\Omega \left(\nabla \cdot \mathbf{S}(\mathbf{u}, p) \right) \cdot \mathbf{v} d\Omega = \int_\Gamma \left(\mathbf{S} \cdot \mathbf{v} \right) \cdot \mathbf{n} d\gamma - \int_\Omega \mathbf{S} : \left(\nabla \mathbf{v} \right) d\Omega, \tag{9}$$

where $\mathbf{n}$ is the outward normal on the boundary Γ. It is now possible to rewrite the second term on the right hand side, by exploiting the symmetry of the stress tensor along with $\mathbf{A} : \mathbf{B} = \mathbf{B} : \mathbf{A}$ and the linearity of the trace of a matrix,

$$\begin{aligned} \int_\Omega \mathbf{S} : \left(\nabla \mathbf{v} \right) d\Omega &= \int_\Omega \frac{1}{2} \mathbf{S} : \left(\nabla \mathbf{v} \right) d\Omega + \int_\Omega \frac{1}{2} \mathbf{S}^{\mathbf{T}} : \left(\nabla \mathbf{v} \right) d\Omega \\ &= \int_\Omega \mathbf{S} : \left(\frac{1}{2} \nabla \mathbf{v} \right) d\Omega + \int_\Omega \mathbf{S} : \left(\frac{1}{2} \nabla \mathbf{v} \right)^T d\Omega \\ &= \int_\Omega \mathbf{S} : \left(\frac{1}{2} \nabla \mathbf{v} + \left(\frac{1}{2} \nabla \mathbf{v}^T \right) \right) d\Omega \\ &= \int_\Omega \mathbf{S} : \mathbf{D} \left(\mathbf{v} \right) d\Omega \\ &= \int_\Omega 2\eta \mathbf{D} \left(\mathbf{u} \right) : \mathbf{D} \left(\mathbf{v} \right) d\Omega - \int_\Omega p \nabla \cdot \mathbf{v} d\Omega. \end{aligned} \tag{10}$$

The boundary part of Eq. 9 is now considered. We require that on the solid boundary $\mathbf{v} \cdot \mathbf{n} = 0$. Since the vectors $\mathbf{n}_S$ and $\mathbf{t}_S$ constitute one orthonormal basis and $\mathbf{n}_F$ and $\mathbf{t}_F$ another, the test function can be decomposed as

$$\mathbf{v} = (\mathbf{v} \cdot \mathbf{n}_S)\mathbf{n}_S + (\mathbf{v} \cdot \mathbf{t}_S)\mathbf{t}_S,$$

on the solid-liquid boundary. On the free surface it is correspondingly written

$$\mathbf{v} = (\mathbf{v} \cdot \mathbf{n}_F)\mathbf{n}_F + (\mathbf{v} \cdot \mathbf{t}_F)\mathbf{t}_F.$$

The boundary part of the integral of the stress tensor is split up into two parts:

$$\begin{aligned} \int_\Gamma \mathbf{v} \cdot S(\mathbf{u}, p) \cdot \mathbf{n} ds = &\int_{\Gamma_{\text{free}}} \mathbf{v} \cdot S(\mathbf{u}, p) \cdot \mathbf{n}_F ds \\ &+ \int_{\Gamma_{\text{solid}}} \mathbf{v} \cdot S(\mathbf{u}, p) \cdot \mathbf{n}_S ds. \end{aligned} \tag{11}$$

Using the decomposition of $\mathbf{v}$, the free boundary integral is

$$\int_{\Gamma_{\text{free}}} \mathbf{v} \cdot S(\mathbf{u}, p) \cdot \mathbf{n}_F ds = \int_{\Gamma_{\text{free}}} \sigma (\mathbf{v} \cdot \mathbf{n}_F) \nabla_s \cdot \mathbf{n}_F ds, \tag{12}$$

where the boundary conditions from equation (4) have been used. The same goes for the boundary integral on the solid-liquid surface, using (5)

$$\int_{\Gamma_{\text{solid}}} \mathbf{v} \cdot S(\mathbf{u}, p) \cdot \mathbf{n}_S ds = -\frac{1}{\beta} \int_{\Gamma_{\text{solid}}} (\mathbf{v} \cdot \mathbf{t}_S)(\mathbf{u} \cdot \mathbf{t}_S) ds. \tag{13}$$

The equations to be solved are stated as

$$a\left(\mathbf{u}, \mathbf{v} \right) = b\left(\mathbf{v} \right), \tag{14}$$

where

$$\begin{aligned} a\left(\mathbf{u}, \mathbf{v} \right) = &\int_\Omega Re \partial_t \mathbf{u} \cdot \mathbf{v} d\Omega + \int_\Omega Re \left(\mathbf{u} \cdot \nabla \right) \mathbf{u} \cdot \mathbf{v} d\Omega \\ &+ \int_\Omega 2\eta \mathbf{D} \left(\mathbf{u} \right) : \mathbf{D} \left(\mathbf{v} \right) d\Omega \\ &+ \frac{1}{\beta} \int_{\Gamma_{\text{solid}}} (\mathbf{v} \cdot \mathbf{t}_S)(\mathbf{u} \cdot \mathbf{t}_S) ds + \int_\Omega q \nabla \cdot \mathbf{u} \\ b\left(\mathbf{v} \right) = &\int_\Omega p \nabla \cdot \mathbf{v} d\Omega + \int_{\Gamma_{\text{free}}} (\mathbf{v} \cdot \mathbf{n}_F) \sigma \nabla_s \cdot \mathbf{n}_F d\gamma \\ &+ \int_\Omega \mathbf{f} \cdot \mathbf{v} d\Omega. \end{aligned} \tag{15}$$

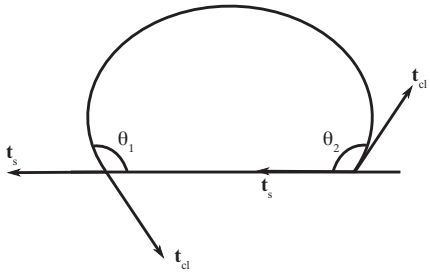

Fig. 2. The left and right side of the drop and corresponding contact angles (θ_1 and θ_2 respectively), along with the solid tangents ($\mathbf{t}_s$) and contact line tangents ($\mathbf{t}_{\mathrm{cl}}$).

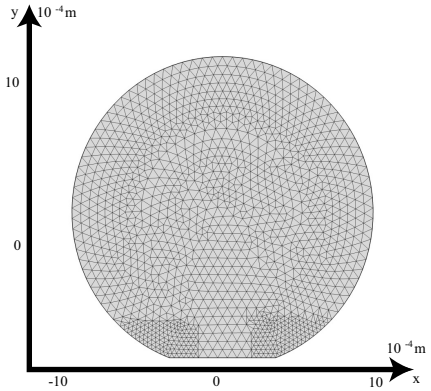

Fig. 3. The initial mesh is shown for a drop with $\theta_1 = \theta_2 = 160°$. Notice the more finely resolved mesh structure near the contact line points.

2.3 Including the contact angle

In order to include the contact angle in the weak formulation we consider the following integral from $b(\mathbf{v})$

$$\int_{\Gamma_{\mathrm{free}}} (\mathbf{v}\cdot\mathbf{n}_F)\sigma\nabla_s\cdot\mathbf{n}_F ds. \tag{16}$$

Recall that $\kappa = \nabla_s\cdot\mathbf{n}$. Through the Frenet-Serret equation we have

$$\partial_s\mathbf{t} = \kappa\mathbf{n}, \tag{17}$$

where ∂_s denotes differentiation with respect to arc length. Using this in 12 and integrating by parts we get

$$\int_{\Gamma_{\mathrm{free}}} \sigma\mathbf{v}\cdot\partial_s\mathbf{t}_F ds = -\int_{\Gamma_{\mathrm{free}}} \sigma\mathbf{t}_F\cdot\partial_s\mathbf{v} ds + [\sigma\mathbf{v}\cdot\mathbf{t}_F]_{\mathrm{cl}}, \tag{18}$$

where $[\cdot]_{\mathrm{cl}}$ means evaluated at the contact line. The first part of the integral can be computed since $\mathbf{t}_F\cdot\partial_s\mathbf{v} = \nabla_s\mathbf{v}$. For the second part we decompose the test function, as before, into

$$\mathbf{v} = (\mathbf{v}\cdot\mathbf{n}_S)\mathbf{n}_S + (\mathbf{v}\cdot\mathbf{t}_S)\mathbf{t}_S, \tag{19}$$

where we note that the no-penetration boundary condition $\mathbf{v}\cdot\mathbf{n}_S = 0$ removes the first term. Inserting Eq. 19 into Eq. 18 we obtain

$$\int_{\Gamma_{\mathrm{free}}} \sigma\mathbf{v}\cdot\partial_s\mathbf{t}_F ds = -\int_{\Gamma_{\mathrm{free}}} \sigma\mathbf{t}_F\cdot\partial_s\mathbf{v} ds + [\sigma(\mathbf{v}\cdot\mathbf{t}_S)(\mathbf{t}_S\cdot\mathbf{t}_F)]_{\mathrm{cl}}. \tag{20}$$

For suitable choice of $[\mathbf{t}_F]_{\mathrm{cl}}$ we get $\mathbf{t}_S\cdot[\mathbf{t}_F]_{\mathrm{cl}} = \cos\theta$. The situation can be seen in Fig. 2. Eq. 20 now becomes

$$\int_{\Gamma_{\mathrm{free}}} \sigma\mathbf{v}\cdot\partial_s\mathbf{t}_F ds = -\int_{\Gamma_{\mathrm{free}}} \sigma\mathbf{t}_F\cdot\partial_s\mathbf{v} ds + \sigma\cos\theta\,[(\mathbf{v}\cdot\mathbf{t}_S)]_{\mathrm{cl}}. \tag{21}$$

Contact angle hysteresis, the measure of the difference between the receding and the advancing contact angle, can now be included by specifying a relation between the angle and the velocity at the triple point. There are several models that can be employed, depending on which specific situation is modeled[28]. We choose to model the hysteresis as a step-function having basically only two values depending on the sign of the speed of the contact line.

3 Simulations and meshing

The model was implemented in the numerical framework of COMSOL v. 4.3a[29]. The geometry was created as described above, and then meshed using the programs meshing tools. Care was taken to set up an initial mesh that would resolve the boundaries adequately. Since the boundary and domain of the droplet is moving in time, the Arbitrary Lagragian-Eulerian method was used[30]. The mesh on the boundaries is displaced with the fluid, whereas inside the drop, it is smoothly advected by solving a Winslow partial differential equation[31]. Remeshing of the domain was done when the quality of any mesh element fell below a given threshold. The largest gradients in velocities were expected to be observed near the triple line, necessitating a finer mesh in these areas, see Fig. 3.

To find the static shape of the drop on a hydrophobic surface we initially set $\alpha = 0$, and then let the drop evolve from a starting shape with $\theta_1 = \theta_2 = 90°$ to the new equilibrium shape. This configuration was then saved, remeshed and used as a starting point for the rest of the simulations. There were approximately 2300 mesh nodes, corresponding to roughly 6000 degrees of freedom.

4 Results

In the following section we present results relating to the motion of a droplet down an inclined plane. We first show different drop shapes and proceed to describing the dynamics of a moving droplet.

4.1 Drop shapes

In the case of $\alpha = 0$, the drop shape deforms solely due to gravity. The Bond number, $Bo = \frac{\rho g r}{\sigma}$, where r is the drop radius, is a measure of the relative influence of gravity compared to surface tension effects. Fig. 4 shows the evolution of the drop shape with changing Bond number, and a fixed contact angle of 140°. For lower Bond numbers the drop shape becomes increasingly circular, either due to decreased gravitational effects or an increase in surface tension.

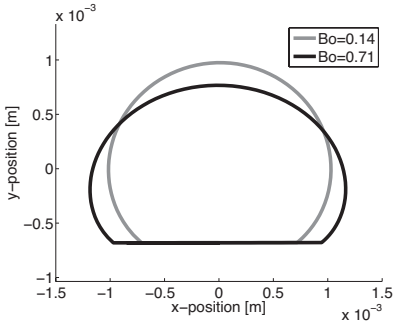

Fig. 4. Static drop shapes for increasing Bond number and contact angle 140°.

When the inclination angle is different from 0, the drop moves down the surface, provided the gravitational pull surpasses the contact angle hysteresis force. Three drop shapes are shown in Fig. 5 for moving droplets with a 10° hysteresis, and three different contact angles. The Figure depicts how the contact area with the surface decreases as the contact angle increases.

4.2 Sliding velocity as a function of slip parameter

We now focus on the dynamical effects of drops moving down an inclined plane. The influence of the slip parameter β (see eq. 5) on a droplet of radius $r_0 = 0.85$ mm residing on a surface inclined $\alpha = 1°$, with $\theta = 160°$ and hysteresis $\Delta\theta = 10°$ is shown in Fig. 6. In the plot, five solutions are shown for β increasing in value from 10^{-6} m to 10^{-2} m. Also, data found in the literature with the same

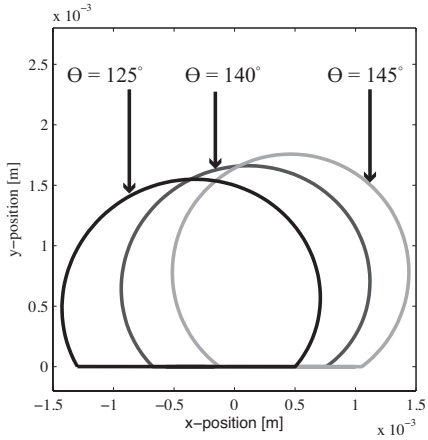

Fig. 5. Drop shapes for moving droplets with contact angles of $\theta = 125°$, $\theta = 140°$ and $\theta = 145°$ with a 10° hysteresis. The coordinates have been translated to allow for comparison.

system parameters are shown. The effect of increasing the slip length saturates at some threshold, in practice resulting in an upper bound on the acceleration of the droplet. Furthermore, for $\beta = 10^{-6}$ m and $\beta = 10^{-5}$ m, a steady state is reached, owing to a balancing of the gravitational pull with the hysteresis force and the viscous dissipation in the drop. For larger slip lengths, the steady state is not reached, but would have been, had longer simulation times been used. The experimental data is well described by the model with $\beta = 10^{-3}$ m and $\beta = 10^{-2}$ m, with little difference between these two solutions.

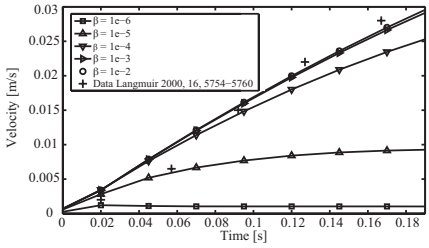

Fig. 6. Velocity of a drop as a function of time for different values of β. $\alpha = 1°$, with $\theta = 160°$ and hysteresis $\Delta\theta = 10°$. Also plotted is data found in the literature for similar system parameters[32].

The Navier-slip condition employed at the solid-liquid effectively means that the drop is sliding down the sur-

face. However, this sliding motion gives rise to some rotation inside the drop, and we therefore expect a somewhat smaller velocity than for a purely sliding object. A comparison of the solution for $\beta = 10^{-3}$ m with four known purely rolling objects, and a purely sliding object, is seen in Fig. 7. As expected, the solution for the droplet lies

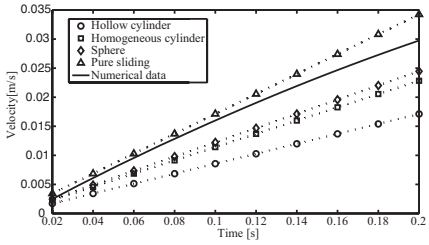

Fig. 7. Velocity as a function of time for a purely sliding object, our numerical solution, and four purely rotating objects. In all cases, $\alpha = 1°$, and for the droplet, additionally $\theta = 160°$ and $\Delta\theta = 10°$.

between the purely sliding object and the purely rolling objects. This clearly indicates that some rotation is going on inside the drop, dissipating energy and slowing down the descent of the drop. However, it should be noted that the descent is still remarkably close to a frictionless sliding motion on the surface, i.e. there is very little drag from the solid on the liquid drop.

4.3 Energy considerations

The total kinetic energy of the drop is given by

$$E_{\text{total}} = E_{CM} + E_R = \frac{1}{2} m v_{CM}^2 + E_R, \qquad (22)$$

where v_{CM} is the velocity of the centre of mass, and E_R is the residual energy of the drop, relating to the rotational energy, seen from the accelerated centre of mass coordinate system. We compute E_R as the difference between E_{total} and E_{CM}. Fig. 8 shows the fraction $\frac{E_{CM}}{E_R}$ for three droplets with $\alpha = 1°$, $\theta = 140°, 145°, 150°$ and hysteresis $\Delta\theta = 10°$. For $t < 0.1$ s, the translational energy grows and becomes 40-50 times larger than the energy E_R of the internal flow. The unsteady motion observed for $t < 0.1$ s is due to surface waves; once these waves are damped sufficiently, the motion becomes steady. At later times, $t > 0.1$ s, a saturation is seen, and the amount of translation to internal flow energy becomes almost constant at a value of around 35.

To consider the effect of gravity on the droplet dynamics we show, in Fig. 9, the fraction $\frac{E_{CM}}{E_R}$ for five different Bond number values. For increasing Bond number, the droplet rotational energy increases, which could possibly be due to a larger contact area with the surface.

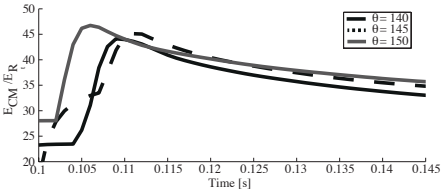

Fig. 8. The fraction $\frac{E_{CM}}{E_R}$ as a function of time for $\alpha = 12°$, $\theta = 140°, 145°, 150°$ and hysteresis $\Delta\theta = 10°$. The graph shows the relative magnitude of the energy associated with translation and internal flow. The surface is tilted at $t = 0.1$ s.

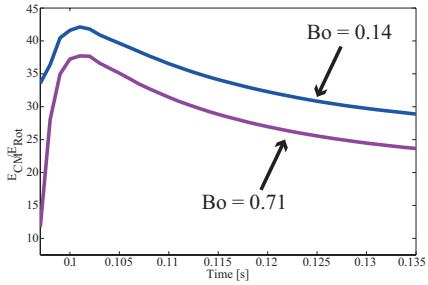

Fig. 9. The fraction $\frac{E_{CM}}{E_R}$ as a function of time for increasing Bond number. The inclination is $\alpha = 1°$, the contact angle is $140°$ and the surface is tilted at $t = 0.1$ s.

4.4 Velocity field inside the drop

The internal flow in the drop is visualized in Figs. 10-12. In Fig. 10 the drop is shown in the laboratory frame, whereas in Figs. 11 and 12, the drop is shown in the frame of reference moving with the centre of mass of the drop, which is in the x-direction (to the right). Fig. 10 shows the drop at $t = 0.08$ s; the colour surface depicts the z-component of the vorticity (the only non-zero component). The Figure indicates that essentially all fluid rotating motion is located below the centre of mass in the drop. Furthermore, the vorticity resembles the one obtained in previous studies[25]. Figs. 11 and 12 depict the evolution of the velocity field in the centre of mass frame as the average velocity increases from time $t = 0.045$ s to $t = 0.19$ s, respectively. Clearly, there is a rotating circulation inside the drop, however, the velocities associated with rotation substantially vary as a function of the position inside the drop. The normalized arrows indicate the direction of the flow, and the contour surface shows the magnitude of the velocity. We note that the point around which the flow rotates, shifts upwards and towards the trailing edge of the droplet as the average velocity increases. Through Particle image velocimetry measurements it is possible to experimentally track particles located inside drops. Fig. 13 shows the trace of three particles located inside the numerically computed

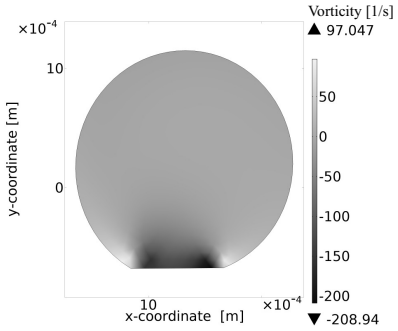

Fig. 10. A drop with $\theta = 160°$, and $\Delta\theta = 10°$ on an incline of $\alpha = 1°$. The drop is depicted in the laboratory frame, and the colour code shows the z-component of the vorticity.

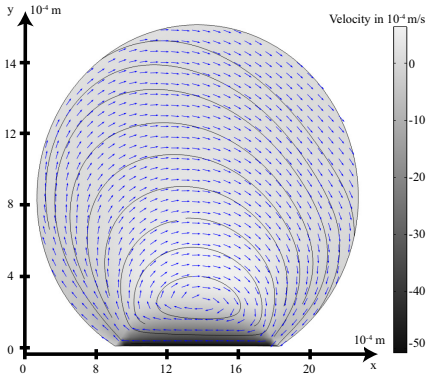

Fig. 11. A drop with $\theta = 160°$, and $\Delta\theta = 10°$ on an incline of $\alpha = 1°$. The drop is depicted in the centre of mass frame of reference, moving to the right. The velocity field directionis indicated by normalised arrows and the streamlines and contour plot shows the size of the velocity. The simulation time is $t = 0.045$ s.

droplet. The small particles were advected with the fluid flow and assumed to have a very small density compared to the fluid density. When placed near the centre of the drop, the trajectory clearly reveals the circulatory motion in the droplet; however, when placed near the boundary, very small displacements are observed, owing to the weak internal flow observed here.

5 Conclusion

We have set up a FEM model that is able to handle a free surface governed by surface tension, along with a slipping

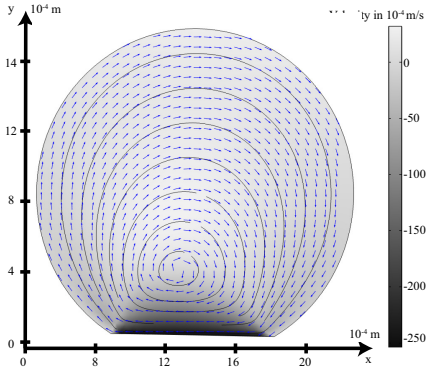

Fig. 12. A drop with $\theta = 160°$, and $\Delta\theta = 10°$ on an incline of $\alpha = 1°$. The drop is depicted in the centre of mass frame of reference, moving to the right. The velocity field directionis indicated by normalised arrows and the streamlines and contour plot shows the size of the velocity. The simulation time is $t = 0.19$ s.

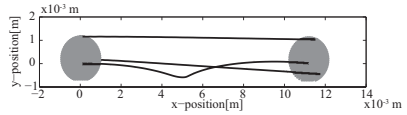

Fig. 13. The evolution of three particles placed inside the drop and advected with the fluid velocity field. The drop evolves from left ($t = 0$ s) to right ($t = 0.6$ s).

surface governed by the Navier slip condition. The model solves the Navier-Stokes equation inside a time-dependent domain along with the partial differential Young-Laplace equation on the free boundary, with a ALE mesh that deforms with the fluid on the boundary.

The slip parameter β was shown to have a significant impact on the initial descent of droplets moving down an inclined plane. We have shown, by comparing with classical mechanical results, that there has to be some rotation inside the drop. This is confirmed by looking at the velocity field in the centre of mass frame of reference of the drop, and the vorticity field corresponds to results seen previously through different numerical methods. Furthermore we highlighted the influence of gravity on the fraction $\frac{E_{CM}}{E_R}$, showing that with increasing Bond number (and thus increasing contact area with the surface), the rotational energy increased. Finally, the model was shown to predict the trajectories of tracer particles located inside the droplet, something which could be useful when comparing to experimental results.

It is our goal in a future study to use the model to make extensive characterisation of structured hydrophobic surfaces by systematically determining the slip coefficient

β, and hence determining the drag reduction as a function of different structure parameters.

6 Acknowledgments

The authors would like to thank The Danish National Advanced Technology Foundation for financial support through the NanoPlast project (File No. 007- 2010-2), and also Rafael Taboryski and Emil Søgaard for ideas and fruitful discussions.

References

1. R. Blossey. Self-cleaning surfaces virtual realities. *Nature Materials*, 2, 2003.
2. L. Mahadevan and Y. Pomeau. Rolling droplets. *Phys. Fluids*, 11(9), 1999.
3. D. Quere. Non-sticking drops. *Rep. Prog. Phys.*, 68:2495–2532, 2005.
4. M. Reyssat, D. Richard, C. Clanet, and D. Quere. Dynamical superhydrophobicity. *Faraday Discussions*, 146:19–33, 2010.
5. N. A. Patankar. On the modeling of hydrophobic contact angles on rough surfaces. *Langmuir*, 19:1249–1253, 2003.
6. O. Bliznyuk, H. P. Jansen, E. S. K. Harold, J. W. Zandvliet, and B. Poelsema. Smart design of stripe-patterned gradient surfaces to controldroplet motion. *Langmuir*, 27:11238–11245, 2011.
7. P. C. Zielke, R. S. Subramanian, J. A. Szymczyk, and J. B. McLaughlin. Movement of drops on a solid surface due to a contact angle gradient. *Proc. Appl. Math. Mech.*, pages 390–391, 2003.
8. A. B. D. Cassie. Contact angles. *Discussions of the Faraday Society*, 3:11–16, 1948.
9. R. N. Wenzel. Resistance of solid surfaces to wetting by water. *Industrial and Engineering Chemistry*, 28(8):988–994, 1936.
10. P. de Gennes, F. Brochard-Wyart, and D. Quere. *Capillarity and Wetting phenomena - Drops, Bubbles, Pearls, Waves*. Springer, 2002.
11. Y. Pomeau. Contact line moving on a solid. *Eur. Phys. J. Special Topics*, 197:15–31, 2011.
12. C. Huh and L. E. Scriven. Hydrodynamic model of steady movement of a solid / liquid / fluid contact line. *Journal of Colloid and Interface Science 1*, 35(1), January 1971.
13. E. B. Dussan. The moving contact line: the slip boundary condition. *J. Fluid Mech.*, 77:665–684, 1976.
14. L. M. Hocking. A moving fluid interface. part 2. the removal of the force singularity by a slip flow. *J. Fluid Mech.*, 79:209–229, 1977.
15. J. P. Rothstein. Slip on superhydrophobic surfaces. *Annu. Rev. Fluid Mech.*, 42:89–109, 2010.
16. Siddarth Srinivasan, Wonjae Choi, Kyoo-Chul Park, Shreerang S. Chhatre, Robert E. Cohen, and Gareth H. McKinley. Drag reduction for viscous laminar flow on spray-coated non-wetting surfaces. *Soft Matter*, 2013.
17. P. H. Saksono and D. Peric. On finite element modelling of surface tension. variational formulation and applications part i: Quasistatic problems. *Comput. Mech.*, 38:265–281, 2006.
18. S. Ganesan and L. Tobiska. Modelling and simulation of moving contact line problems with wetting effects. *Comput. Visual. Sci.*, 12:329–336, 2009.
19. P. H. Saksono and D. Peric. On finite element modelling of surface tension. variational formulation and applications part ii: Dynamic problems. *Comput. Mech.*, 38:251–263, 2006.
20. J. U. Brackbill, D. B. Kothe, and C. Zemach. A continuum method for modeling surface tension. *Journal Of Computational Physics*, 100:335–354, 1992.
21. M. A. Walkley, P. H. Gaskell, P. K. Jimack, M. A. Kelmanson, and J. L. Summers. Finite element simulation of three-dimensional free-surface flow problems. *Journal of Scientific Computing*, 24(2):147–162, 2005.
22. S. P. Thampi, R. Adhikari, and R. Govindarajan. Do liquid drops roll or slide on inclined surfaces? *ArXiv e-prints*, November 2011.
23. B. M. Mognetti, H. Kusumaatmajab, and J. M. Yeomansa. Drop dynamics on hydrophobic and superhydrophobic surfaces. *Faraday Discussions*, 146:153–165, 2010.
24. A. K. Das and P. K. Das. Multimode dynamics of a liquid drop over an inclined surface with a wettability gradient. *Langmuir*, 26(12):9547–9555, 2010.
25. S. P. Thampi, R. Adhikari, and R. Govindarajan. Do liquid drops roll or slide on inclined surfaces? *Langmuir*, 29:3339–3346, 2013.
26. M. Heller. *Numerical study of free surfaces and particle sorting in microfluidic systems*. PhD thesis, Technical University of Denmark, Department of Micro- and Nanotechnology, 2008.
27. H. Bruus. *Theoretical Microfluidics*. Oxford University Press Inc., New York, 2008.
28. Sashikumaar Ganesan. On the dynamic contact angle in simulation of impinging droplets with sharp interface methods. *Microfluidics and Nanofluidics*, 14:615–625, 2013.
29. www.comsol.com.
30. Jean Donea, Antonio Huerta, J.-Ph. Ponthot, and A. Rodrguez-Ferran. *Arbitrary Lagrangian-Eulerian Methods, Encyclopedia of Computational Mechanics*. John Wiley & Sons, Ltd, 2004.
31. P.M. Knupp. Winslow smoothing on two-dimensional unstructured meshes. *Engineering with Computers*, 15(3):263–268, 1999.
32. Masashi Miwa, Akira Nakajima, Akira Fujishima, Kazuhito Hashimoto, and Toshiya Watanabe. Effects of the surface roughness on sliding angles of water droplets on superhydrophobic surfaces. *Langmuir*, 16:5754–5760, 2000.

Bibliography

[1] L.D. Landau and E.M. Lifshitz. *Fluid Mechanics*. Elsevier, Oxford, 2010.

[2] Sir Horace Lamb. *Hydrodynamics*. Cambridge University Press, 1895.

[3] H. Bruus. *Theoretical Microfluidics*. Oxford University Press Inc., New York, 2008.

[4] A. Pressley. *Elementary differential geometry*. Springer-Verlag London Limited, 2007.

[5] P. H. Saksono and D. Peric. On finite element modelling of surface tension. variational formulation and applications – part i: Quasistatic problems. *Comput. Mech.*, 38:265–281, 2006.

[6] Lord Rayleigh. On the cappillary phenomena of jets. *Proceedings of the Royal Society of London*, 29:71–97, 1879.

[7] C. A. Miller and L. E. Scriven. The oscillations of a fluid droplet immersed in another fluid. *Journal of Fluid Mechanics*, 32(3):417–435, 1968.

[8] http://mathworld.wolfram.com/solidharmonic.html.

[9] T. Funada J.C. Padrino and D.D. Joseph. Purely irrotational theories for the viscous effects on the oscillations of drops and bubbles. *International Journal of Multiphase Flow*, 34(61), 2008.

[10] http://engineeringtoolbox.com/surface-tension-d_962.html.

[11] A. P. Engsig-Karup. *The Spectral/hp-Finite Element Method for Partial Differential Equations*. Technical University of Denmark, 2011.

[12] Comsol. User's guide, 2013.

[13] Mads Jakob Jensen. *Numerical simulations of interface dynamics in microfluidics*. PhD thesis, Technical University of Denmark, 2005.

[14] Howard H. Hu, N. A. Patankar, and M. Y. Zhu. Direct numerical simulations of fluid–solid systems using the arbitrary lagrangian–eulerian technique. *Journal of Computational Physics*, 169:427–462, 2001.

[15] Sashikumaar Ganesan. *Finite element methods on moving meshes for free surface and interface flows*. PhD thesis, Fakultaet fur Mathematik der Otto-von-Guericke-Universitaet Magdeburg, 2006.

[16] J. Donea1, Antonio Huerta, J.-Ph. Ponthot1, and A. Rodrıguez-Ferran. *Encyclopedia of Computational Mechanics - Arbitrary Lagrangian–Eulerian Methods*, volume 1. John Wiley & Sons, 2004.

[17] R. Blossey. Self-cleaning surfaces — virtual realities. *Nature Materials*, 2, 2003.

[18] Andrew R. Parker and Chris R. Lawrence. Water capture by a desert beetle. *Nature*, 414:33–34, 2001.

[19] Yongmei Zheng, Xuefeng Gao, and Lei Jiang. Directional adhesion of superhydrophobic butterfly wings. *Soft Matter*, 3:178–182, 2007.

[20] D. Robert and J. Rulon. *Contact Angle Hysteresis*. 1964.

[21] R. N. Wenzel. Resistance of solid surfaces to wetting by water. *Industrial and Engineering Chemistry*, 28(8):988–994, 1936.

[22] J. Bico, C. Marzolin, and D. Quere. Pearl drops. *Europhysics letters*, 47(2):220–226, 1999.

[23] A. B. D. Cassie. Contact angles. *Discussions of the Faraday Society*, 3:11–16, 1948.

[24] A. B. D. Cassie and S. Baxter. Wettability of porous surfaces. *Trans. Faraday Soc.*, 40:546–551, 1944.

[25] Mathilde Callies and David Quere. On water repellency. *Soft Matter*, 1:55–61, 2005.

[26] P. de Gennes, F. Brochard-Wyart, and D. Quere. *Capillarity and Wetting phenomena - Drops, Bubbles, Pearls, Waves*. Springer, 2002.

[27] Mathilde Callies, Yong Chen, Frederic Marty, Anne Pepin, and David Quere. Microfabricated textured surfaces for super-hydrophobicity investigations. *Microelectronic Engineering*, 78–79:100–105, 2005.

[28] Mathilde Reyssat and David Quere. Contact angle hysteresis generated by strong dilute defects. *J. Phys. Chem. B*, 113:3906–3909, 2009.

[29] David Quéré and Mathilde Reyssat. Non-adhesive lotus and other hydrophobic materials. *Philosophical Transactions: Mathematical, Physical and Engineering Sciences*, 366(1870):pp. 1539–1556, 2008.

[30] Siddarth Srinivasan, Wonjae Choi, Kyoo-Chul Park, Shreerang S. Chhatre, Robert E. Cohen, and Gareth H. McKinley. Drag reduction for viscous laminar flow on spray-coated non-wetting surfaces. *Soft Matter*, 9:5691–5702, 2013.

[31] Masashi Miwa, Akira Nakajima, Akira Fujishima, Kazuhito Hashimoto, and Toshiya Watanabe. Effects of the surface roughness on sliding angles of water droplets on superhydrophobic surfaces. *Langmuir*, 16:5754–5760, 2000.

[32] L. Mahadevan and Y. Pomeau. Rolling droplets. *Phys. Fluids*, 11(9), 1999.

[33] D. Quere. Non-sticking drops. *Rep. Prog. Phys.*, 68:2495–2532, 2005.

[34] M. Reyssat, D. Richard, C. Clanet, and D. Quere. Dynamical superhydrophobicity. *Faraday Discussions*, 146:19–33, 2010.

[35] N. A. Patankar. On the modeling of hydrophobic contact angles on rough surfaces. *Langmuir*, 19:1249–1253, 2003.

[36] O. Bliznyuk, H. P. Jansen, E. S. K. Harold, J. W. Zandvliet, and B. Poelsema. Smart design of stripe-patterned gradient surfaces to control droplet motion. *Langmuir*, 27:11238–11245, 2011.

[37] P. C. Zielke, R. S. Subramanian, J. A. Szymczyk, and J. B. McLaughlin. Movement of drops on a solid surface due to a contact angle gradient. *Proc. Appl. Math. Mech.*, 2:390–391, 2003.

[38] M. Reyssat, F. Pardo, and D. Quere. Drops onto gradients of texture. *Europhys. Lett.*, 87:36003, 2009.

[39] Y. Pomeau. Contact line moving on a solid. *Eur. Phys. J. Special Topics*, 197:15–31, 2011.

[40] C. Huh and L. E. Scriven. Hydrodynamic model of steady movement of a solid / liquid / fluid contact line. *Journal of Colloid and Interface Science 1*, 35(1), January 1971.

[41] E. B. Dussan. The moving contact line: the slip boundary condition. *J. Fluid Mech.*, 77:665–684, 1976.

[42] L. M. Hocking. A moving fluid interface. part 2. the removal of the force singularity by a slip flow. *J. Fluid Mech.*, 79:209–229, 1977.

[43] J. P. Rothstein. Slip on superhydrophobic surfaces. *Annu. Rev. Fluid Mech.*, 42:89–109, 2010.

[44] S. Ganesan and L. Tobiska. Modelling and simulation of moving contact line problems with wetting effects. *Comput. Visual. Sci.*, 12:329–336, 2009.

[45] P. H. Saksono and D. Peric. On finite element modelling of surface tension. variational formulation and applications – part ii: Dynamic problems. *Comput. Mech.*, 38:251–263, 2006.

[46] J. U. Brackbill, D. B. Kothe, and C. Zemach. A continuum method for modeling surface tension. *Journal Of Computational Physics*, 100:335–354, 1992.

[47] M. A. Walkley, P. H. Gaskell, P. K. Jimack, M. A. Kelmanson, and J. L. Summers. Finite element simulation of three-dimensional free-surface flow problems. *Journal of Scientific Computing*, 24(2):147–162, 2005.

[48] B. M. Mognetti, H. Kusumaatmajab, and J. M. Yeomansa. Drop dynamics on hydrophobic and superhydrophobic surfaces. *Faraday Discussions*, 146:153–165, 2010.

[49] A. K. Das and P. K. Das. Multimode dynamics of a liquid drop over an inclined surface with a wettability gradient. *Langmuir*, 26(12):9547–9555, 2010.

[50] S. P. Thampi, R. Adhikari, and R. Govindarajan. Do liquid drops roll or slide on inclined surfaces? *Langmuir*, 29:3339–3346, 2013.

[51] www.comsol.com.

[52] P.M. Knupp. Winslow smoothing on two-dimensional unstructured meshes. *Engineering with Computers*, 15(3):263–268, 1999.

[53] Sashikumaar Ganesan. On the dynamic contact angle in simulation of impinging droplets with sharp interface methods. *Microfluidics and Nanofluidics*, 14:615–625, 2013.

[54] RLC Flemmer and CL Banks. On the drag coefficient of a sphere. *Powder Technology*, 48(3):217–221, 1986.

[55] J. Molacek and J. W. M. Bush. Drops bouncing on a vibrating bath. *J. Fluid Mech*, 727:582–611, 2013.

[56] J. Walker. Drops of liquid can be made to float on the liquid. what enables them to do so? *The Amateur Scientist, Sci. Am.*, 238:151—158, 1978.

[57] Y. Couder, S. Protiere, E. Fort, and A. Boudaoud. Dynamical phenomena: Walking and orbiting droplets. *Nature*, 437, 2005.

[58] J. W. M. Bush. Quantum mechanics writ large. *Proc. Nat. Acad. Sci.*, 107(41):17455—17456, October 2010.

[59] L. de Broglie. Interpretation of quantum mechanics by the double solution theory. *Annales de la Fondation Louis de Broglie*, 12(4), 1987.

[60] Øistein Wind-Willassen, Jan Moláček, Daniel M. Harris, and John W. M. Bush. Exotic states of bouncing and walking droplets. *Physics of Fluids*, 25:082002, 2013.

[61] Bo Christiansen. *Faraday waves and Collective phenomena in coupled oscillators*. PhD thesis, Niels Bohr Institute, Copenhagen University, 02 1993.

[62] T. B. Benjamin and F. Ursell. The stability of the plane free surface of a liquid in vertical periodic motion. *Proc. Royal Soc. London. Series A, Math. Phys. Sci.*, 225(1163):505–515, 1954.

[63] S. Douady. Experimental study of the faraday instability. *J. Fluid Mech.*, 221:383–409, 1990.

[64] S. Protiere, A. Boudaoud, and Y. Couder. Particle-wave association on a fluid interface. *J. Fluid Mech.*, 554:85—108, 2006.

[65] A. Eddi, E. Sultan, J. Moukhtar, E. Fort, M. Rossi, and Y. Couder. Information stored in faraday waves: the origin of a path memory. *J. Fluid Mech.*, 674:433, 2011.

[66] Y. Couder, E. Fort, C.-H. Gautier, and A. Boudaoud. From bouncing to floating: Noncoalescence of drops on a fluid bath. *Phys. Rev. Lett.*, 94:154101, 2006.

[67] A. Eddi, A. Decelle, E. Fort, and Y. Couder. Archimedean lattices in the bound states of wave interacting particles. *Europhys. Letters*, 87:56002, 2009.

[68] A. Eddi, A. Boudaoud, and Y. Couder. Oscillating instability in bouncing droplet crystals. *Europhys. Letters*, 94:20004, 2011.

[69] T. Gilet, D. Terwagne, N. Vandewalle, and S. Dorbolo. Dynamics of a bouncing droplet onto a vertically vibrated interface. *Phys. Rev. Lett.*, 100:167802, 2008.

[70] T. Gilet and J. W. M. Bush. The fluid trampoline: Droplets bouncing on a soap film. *J. Fluid Mech.*, 625:167—203, 2009.

[71] T. Gilet and J.W.M. Bush. Chaotic bouncing of a droplet on a soap film. *Phys. Rev. Lett.*, 625:0145011—0145014, 2009.

[72] J. Moláček and J. W. M. Bush. A quasi-static model of drop impact. *Phys. Fluids*, 22124(127103):1–16, 2012.

[73] J. Molacek and J. W. M. Bush. Drops walking on a vibrating bath: towards a hydrodynamic pilot-wave theory. *Submitted to J. Fluid Mech*, 727:612–647, 2013.

[74] A. U. Oza, R. R. Rosales, and J. W. M. Bush. A trajectory equation for walking droplets: hydrodynamic pilot-wave theory. *J. Fluid Mech.*, 737:552–570, 2013.

[75] Anand U. Oza, Daniel M. Harris, Rodolfo R. Rosales, and John W. M. Bush. Pilot-wave dynamics in a rotating frame: on the emergence of orbital quantization. Submitted to J. Fluid Mech., 2013.

[76] A. Eddi, D. Terwagne, E. Fort, and Y. Couder. Wave propelled ratchets and drifting rafts. *Europhys. Letters*, 82:44001, 2008.

[77] J. D. Meiss. *Differential Dynamical Systems*. SIAM, 2007.

[78] E. Fort, A. Eddi, A. Boudaoud, J. Moukhtar, and Y. Couder. Path-memory induced quantization of classical orbits. *Proc. Nat. Acad. Sci.*, 107(41):17515–17520, October 2010.

[79] A. Eddi, J. Moukhtar, S. Perrard, E. Fort, and Y. Couder. Level splitting at macroscopic scale. *Phys. Rev. Lett.*, 108:264503, 2012.

[80] William H. Press, Brian P. Flannery, Saul A. Teukolsky, and William T. Vetterling. *Numerical recipes - the art of scientific computing*. Cambridge University Press, 1986.

[81] Steven H. Strogatz. *Nonlinear dynamics and chaos*. Westview press, 1994.

[82] Daniel M. Harris and John W. M. Bush. Droplets walking in a rotating frame: from quantized orbits to wavelike statistics. Submitted to J. Fluid Mech., 2013.

[83] Heinz Georg Schuster. *Deterministic chaos*. Physik-Verlag GmbH, 1984.

[84] Yuzhu Xiao, Yan Wang, and Ying-Cheng Lai. Dependence of intermittency scaling on threshold in chaotic systems. *Physical Review E*, 80:057202, 2009.

[85] Y. Couder and E. Fort. Probabilities and trajectories in a classical wave-particle duality. *Journal of Physics: Conference Series*, 361:012001, 2012.

[86] Y. Couder and E. Fort. Single-particle diffraction and interference at a macroscopic scale. *Phys. Rev. Lett.*, 97:177801, 2005.

[87] A. Eddi, E. Fort, F. Moisy, , and Y. Couder. Unpredictable tunneling of a classical wave-particle association. *Phys. Rev. Lett.*, 102:240401, 2009.

[88] David J. Griffiths. *Introduction to Quantum Mechanics*. Pearson Prentice Hall, 2 edition, 2005.

[89] M. Reyssat, A. Pepin, F. Marty, Y. Chen, and D. Quere. Bouncing transitions on microtextured materials. *Europhys. Lett.*,, 74 (2):pp. 306–312, 2006.